Alma Mater Studiorum – Università di Bologna

DOTTORATO DI RICERCA IN

CHIMICA

Ciclo XXXII°

Settore Concorsuale: 03/B1

Settore Scientifico Disciplinare: CHIM/03

Photosynthetic Solar Fuels and Chemicals Production with Hybrid Inorganic Semiconductor Nanostructures

Presentata da: AGOSTI AMEDEO

Coordinatore Dottorato — **Supervisore**

Prof. Tonelli Domenica — **Prof.Bergamini Giacomo**

Esame finale anno 2020

Aknowledgements

I would first like to thank Prof. Giacomo Bergamini for his endless efforts in supervising me over the last three years. He has always demonstrated trust and confidence in my skills, patiently enriched my scientific knowledge and provided me with freedom and responsibility. His office door has always been open for me to grow not only as a scientist, but also as a person. I feel indebted for this and I hope he will find this thesis a reward for his dedication and kindness.

Secondly, I am extremely grateful to my collaborators from the PHOTOTRAIN project. In particular, I would like to thank Prof. Amirav for the unique opportunity to work in his lab at Technion and live a fascinating life experience in Israel. However, my time as a PhD student wouldn't have so interesting without all of the other members of the network, Dr. Lucy Scioscia, Dr. Tommaso Battisti, Dr. Kaituo Dong, Dr. Alex McMillan, Dr. Nurtalya Alandini, Dr. Cristofer Pezzella, Dr. Daniele Mazzarella, Dr. Gustavo Ribeiro, Dr. Oliwia Matusewska, Dr. Argyri Giakoumakis, Dr. Thien Le Phu, Dr. Lexie Cheng and Dr. Hoawei Huang. Above all, I had the pleasure to work closely with Dr. Ewelina Kuna, whose perseverance and gentleness have been an example for me.

I would also like to thank all the people that made my life so much more than just what I was building at work. I am especially glad to be part of unique group of friends, la MONO, that have always been home for me, no matter how far work was bringing me from Piacenza. Moreover, Bologna has been a special place where to live, and this is thanks to the amazing people that I met at Ciamician, at Active and to Denis, the best flatmate I've ever had.

Finally, I would like to dedicate my wholehearted recognition to my family. Never did I have a moment where I lacked your help, attention, support and love also in this delicate moment of my education. My happiness is the fruit of your daily dedication to me and my brother and all of my actions are driven by the desire to become as great person as you are.

Lastly, I would like to thank Virginia. This thesis would not have existed without having you close to me. Once more, we are tougher than the rest.

Abstract

In the present thesis hybrid inorganic semiconductor nanostructures are investigated for solar-to-chemical energy conversion purposes. Among the family of fuel-forming reactions, hydrogen (H_2) production is targeted by means of mild and sustainable synthetic routes. Traditional water splitting poses, to this extent, stringent kinetics and technological limitations, hampering overall photochemical performance.

Leveraging on the superior H_2 forming quantum efficiency expressed by core-shell CdSe@CdS seeded-rod (SR) nanostructures, we develop alternative anodic organic transformations to realise closed redox cycle solar chemicals syntheses Notably, this approach circumvents the use of sacrificial reagents, promoting instead value-added oxidative chemistries. We find that fluorescence quenching screening allows for rigorous selection of such reactions, defining precise optoelectronic rules bridging between materials properties and photosynthetic performance. This is in contrast to conventional serendipitous development of catalytic processes, whose trial-and-error approach is surpassed by means of cheap and readily available spectrophotometric tools. Spectroscopic evidence also provides insights into reaction optimisation, chemical selectivity, and materials photostability. We observe that, for aldehyde forming transformations, extensive chemical potential is stored by the concomitant generation of hydrogen fuel, up to remarkable 4.2% solar-to-chemical conversion efficiencies, doubling state-of-the art solar-to-hydrogen benchmark values. These findings are particularly relevant in the development of photo-corrosion resilient metal chalcogenide photochemical devices.

The ability of this class of nanostructured materials to promote concerted electron transfer is then tested for additional photo-redox reactions. The strong oxidative potential of SR allows access to photo-polymerisation and photo-reforming processes whilst the proton reducing capability in organic media allows for in situ photo-hydrogenations. Furthermore, initial address of chemo-selective radical coupling reactions has leveraged on the nanometric distance between

reduction- and oxidation-active sites, providing a promising outlook for future optimisation.

Finally, attempts to integrate these hybrid semiconductor photocatalysts into microfluidic chips targeted a prompt application of the photosynthetic system to a scalable device. The flow conditions offered by such photoreactors promise to soften current limits and further upgrade solar-to-chemical energy conversion. Not only could turnover number be nourished by continuous reagent replenishment, but photocatalyst recyclability will also be attained at successful chemical anchoring of nanorods to reactor walls. The work presented in this thesis endows therefore Ciamician's dream of the photochemistry of the future with bright forthcoming perspectives.

List of Figures

List of Tables

Contents

Chapter 1 Introduction

1.1. Context: Sustainability and Lack Thereof

The irresponsible use of natural resources witnessed over the past two centuries induced historians to refer to modern times with the term Anthropocene. The central role of mankind in geology and ecology has been particularly evident in the inconsiderate emission of huge amount of carbon dioxide (CO_2) in the atmosphere. The most significant rise in CO_2 concentration has been registered since the beginning of the Industrial revolution, where a steep emission trend brought the initial $275\ ppm$ of carbon dioxide in the atmosphere to skyrocket above $400\ ppm$ in present days. In absolute numbers, this scenario corresponds to an increase in the total amount of CO_2 produced from the 1.957 *billion* tonnes of 1900 to the actual 36.831 *billion* tonnes. China is the principal contributors to nowadays share (27%), however the United States (25%) and the European Union (22%) dispensed the largest portion of cumulative historical emission. The alarming record of carbon dioxide concentration, tracked by the Keeling curve, have, however, been extended to a much wider period of human-related footprint on the environment. Recent analyses of CH_4 and CO_2 isotopes found in ice cores from Greenland revealed indeed distinctive contributions of humankind to worldwide emission in the past two millenia[1,2]. Overall, such dramatic changes are pushing planet Earth to the brink of irreversible climate changes. The scientific consensus almost unanimously attributes the responsibility for such devastating scenario to human activities[3], yet exhaustive endowment to the Sustainable Development Goals can still steer future generations out of risk.

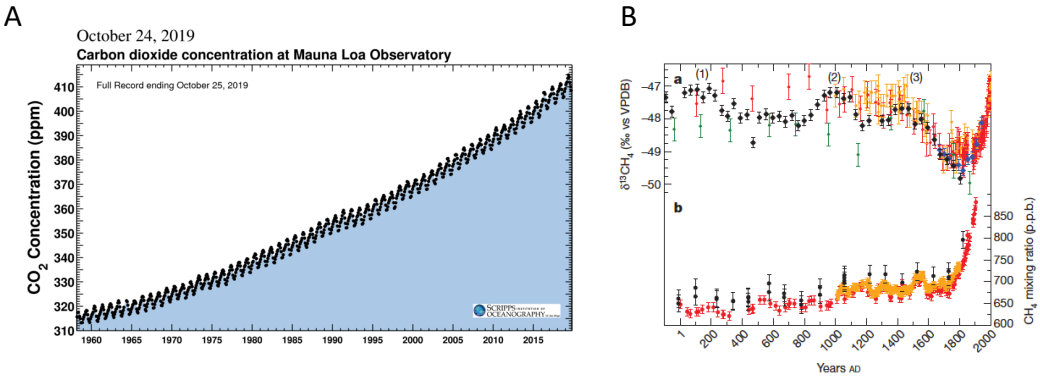

Figure 1.1. ***Historic record of carbon dioxide and methane emissions.***
A) The Keeling Curve, i.e. the daily record of global atmospheric CO_2 concentration, by Scripps Institution of Oceanography at UC San Diego. B) Records of carbon isotope and CH_4 mixing ratio data over the past two millennia, as estimated from air trapped in Greenland ice cores[2]. Evidence was provided for CO_2 concentration correlation with natural climate variability, changes in human population and land use, as well as major events like the decline of Roman Empire and the Han dynasty, the Medieval Climate Anomaly and the Little Ice Age.

Among the 17 challenges that the United Nations have elected as critically important, several of them appear to be intimately connected with energy production and consumption. As can be seen from Figure 1.2, power generation is accountable for the largest part of CO_2 emissions, together with industrial and transportation activities[4]. This is principally due to the fact that, still in 2017, 81% of world primary energy demand was covered by fossil fuels, namely coal, gas and oil, whose combustion products include both CO_2 and pollutants like nitrogen and sulphur oxides. Notably, the overall share of fossil fuels in primary energy demand has not changed over the past 25 years, causing profound environmental, as well as socio-economic changes. In particular, it was estimated that 50% of total primary energy supply was consumed by the wealthiest 10% of the world population, while 3% of the such amount satisfies the energy hunger of the poorest 25% of mankind. Furthermore, universal access to modern energy has fundamental implications in other social issues like economic growth and gender-inequality. Figure 1.2 shows, to this extent, that access to electricity and clean cooking is yet to be conquered for *billions* of people. In 2017, the former problem extended to just below one billion of people, while, in the second case, one third of human population still suffers this issue. Furthermore, lack of modern energy and cooking fuel affects the number of women entering workforce, the latter being a phenomenon that was correlated to

growth in economic productivity in advanced economies over the course of the 20th century. As a result of this, accomplishing Sustainable Development Goals entails complete reversal of the historic relationship interweaving economic growth, energy demand and emissions.

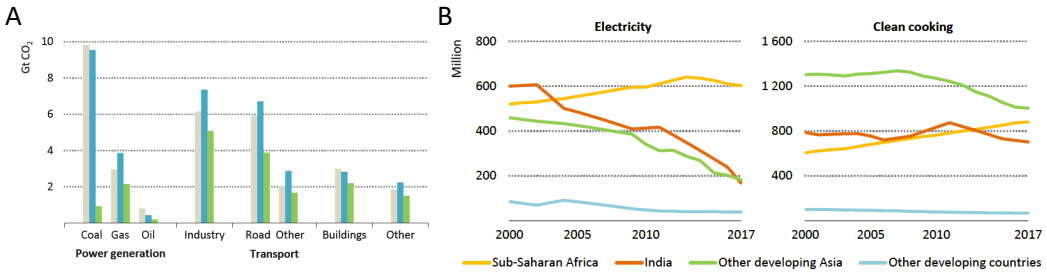

Figure 1.2. ***A few present global issues: CO_2 emissions and population without modern energy access.***

A) World energy-related CO_2 emissions by sector. Grey bars represent 2017 estimated values, while blue and green bars refer to projections according to World Energy Outlook's New Policy and Sustainable Development Scenario, respectively[4]. B) Development of the share of world population without access to electricity and clean cooking.

One of the most prospective change in the energy mix scenario can be determined by the deployment of the hydrogen economy. This high gravimetric energy dense fuel can in fact respond to a variety of issue: H_2 can be deployed in all end-user sectors and exploited for electricity production, it can be stored, distributed into the existing gas network and used on-demand without green-house gases or pollutants emission. Nowadays, hydrogen is already a chemical commodity in the fields of oil refinery, chemicals manufacturing and in the production of iron and steel. Nevertheless, the current 60 million tonnes of H_2 produced worldwide on an annual basis, amounting to only 2% of world primary energy, are obtained through emission-intensive industrial processes. In particular, 50% of the global supply is synthesised through steam methane reforming (SMR), which releases 10 Kg of CO_2 per kg of H_2 produced. This process alone, representing ~0.001% of global emissions, contributes with $\sim 3.7 \cdot 10^{16}$ kg of CO_2 per year to global emissions. "Greener" alternatives are currently pursued to a limited extent, one being the electrolysis of water, which represents only 2% of the H_2 production market because of its high cost, i.e. $\sim\$4 - 6\ /kg_{H_2}$ vs. the $\sim\$1 - 2\ /kg_{H_2}$ needed for SMR.

Despite the enormous technological challenge to be surmounted, H_2 still represents a practical prospective resource to meet several upcoming decarbonisation targets. In the marine shipping sector, for example, it has been singled out as one of the few fuel options allowing to achieve the International Maritime Organisation Agreement to reduce CO_2 levels to 2009 levels. Finally, looking at a larger framework, hydrogen economy will possibly be achieved provided the development of grid-independent generation technologies. Grid-based electricity is indeed expected to remain high, significantly impacting future development of electrolyser technologies. Overall, the quest to decarbonise H_2 production for the energy, chemicals and refining sector stands however as a compelling target to profoundly advance the technology beyond current status in the imminent future.

1.2. State-of-the-art Prototypes and Aim of this Thesis

"I believe that water will one day be employed as fuel, that hydrogen and oxygen which constitute it, used singly or together, will furnish an inexhaustible source of heat and light, of an intensity of which coal is not capable…. Water will be the coal of the future".

The hydrogen economy has been a long-soughed target, in fact, already in 1874 Jules Verne was providing with these words a pioneering manifesto of such concept. As previously described, history witnessed a different technological progress, however, promising methods of H_2 production prototypes are currently being investigated by a vast body of research. In particular, the most obvious strategy to decarbonise hydrogen production is by means of solar-energy harvesting[5–7]. When compared to the solar energy supplied to the Earth by the sun, the overall sum of recoverable energy from all other natural reserves add up to ~1% of the former, making it the ultimate inexhaustible resource in our Galaxy. Noteworthy, the amount of solar power striking our planet in one hour is equivalent to our yearly energy demand ($17.91\ TW$ in 2017). Leveraging on the abundance of such readily available and free resource, various technoeconomic analyses have estimated the threshold efficiency performance to synthesise H_2 via solar input to

be cost competitive with the SMR process benchmark. Specifically, both the United States Department of Energy (in 2011)[8] and Japan Ministry of economy (in 2017)[9], set the solar-to-hydrogen (STH) efficiency target to a minimum of 5-10%, which would allow for a corresponding cost of approximately $\sim\$4 - 6\ /kg_{H_2}$ produced. Currently, three major STH strategies are pursued to achieve this scheme, as schematically depicted in Figure 1.3A-C:

- Photovoltaic + Electrolysis (PV+EC)
- Photoelectrochemical (PEC)
- Suspended photocatalyst (PC).

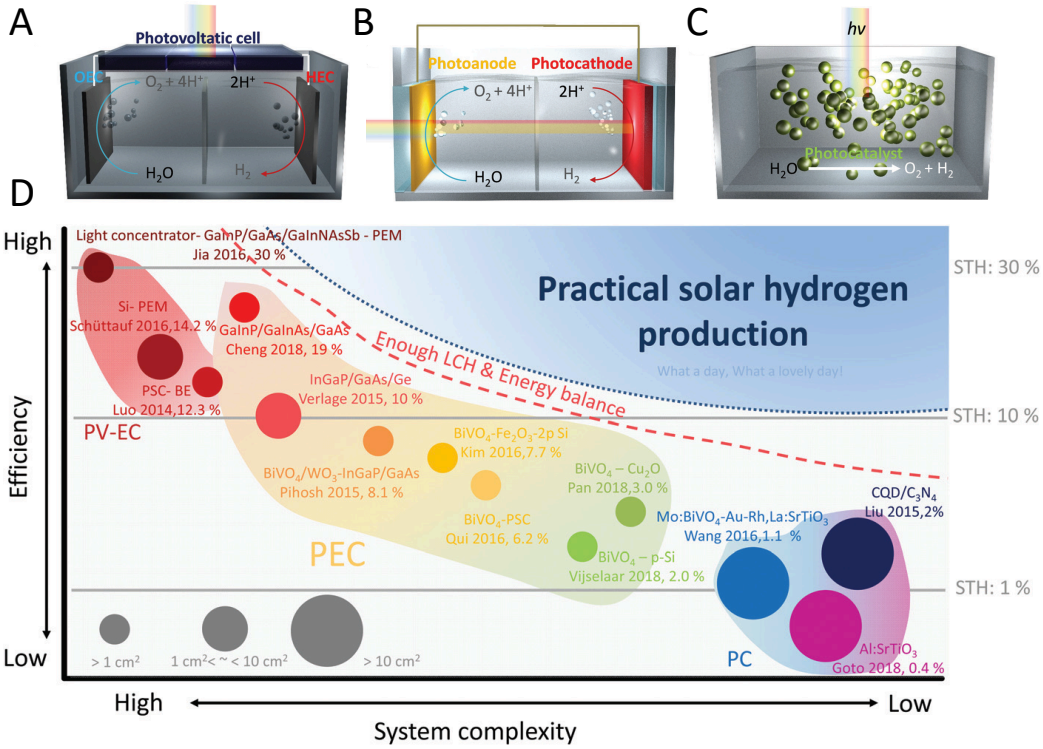

Figure 1.3. ***Technologies and state-of-the-art efficiency for Solar-to-Hydrogen Conversion.***

Solar-driven H_2 producing devices are classified into A) Photovoltaic + Electrolyser (PV-EC), B) Photoelectrochemical (PEC) and C) Photocatalytic (PC) pathways. D) State-of-the-art efficiencies for the different technologies, whose spot size on the graph is proportional to the device scale.

These technologies have fundamentally different operational modes, however, all their experimental maximum efficiencies were estimated to be well above the requested target, namely being >30% for both PV+EC, PEC and PC[10]. Major differences in the device performance optimisation arise therefore when considering device complexity and photo-active materials' morphology. Firstly,

PV+EC systems (Figure 1.3A) comprise the electrical connection between a photovoltaic cell and a pair of electrolysers. In this configuration, the light-harvesting material is not in contact with the reaction solution, thus photo-corrosion is of little concern and separate components optimisation offers the greatest technological appeal. PV+EC also presents the most readily scalable system, however, costs associated with electrical connections significantly affect the economics of this solution. A similar strategy is exploited in photoelectrochemical cells, where light-absorption and chemical reactions processes are condensed in a single component, namely the photo-anode/photo-cathode, that is consequently immersed in the aqueous solution. PEC devices (Figure 1.3B) have the great advantage of potentially eliminating the electrical bias required for PV+EC solutions, thanks to the additional photovoltage input provided to surpass typical overpotential losses. For the overall water splitting reaction it is indeed estimated that a minimum voltage of 1.8V should be provided to kinetically favour reaction turnover. In the case of PEC, even though H_2 and O_2 are generated at different electrodes and separated by an impermeable membrane, photochemical instability poses stringent trade-offs to be considered during materials choice and optimisation. Efficient optoelectronic strategies have therefore to be considered in order to harvest photo-generated charge carriers, preventing their detrimental effect on material's chemical and structural properties. Lastly, the STH device configurations with the simplest system design developed so far is represented by PC devices (Figure 1.3C). In this case the photoactive species is typically in the form of nanostructured moiety immersed in the aqueous phases, where the photocatalyst and the liquid reagent effectively form a homogeneous solution. In spite of the lack of control of charge carriers because of the absence of any external electrical connection, PC has been estimated as the most promising strategy to reach practical STH conversion efficiencies, with real-world flat-plane reactors at the square meter scale already performing at 0.4%[11]. Having the US Department of energy assessed PC approach to potentially provide hydrogen at a cost of $\sim\$2\ /kg_{H_2}$ at 5% STH efficiency, it is exceptional to consider how systems currently being developed in the Domen group are projected to perform at 10% STH at scale[12].

In spite of such remarkable advances expected in process efficiency improvements, a few engineering aspects of the overall STH process are yet to be tackled. Among these, problems related oxygen production are the most pressing. In the first place, the minimum theoretical energy penalty required to separate the explosive H_2/O_2 gas mixture was estimated to lie close to 8.7% of the energy content of the mixture itself[13]. Secondly, even when the former obstacles would be surpassed, the oxygen produced has in general a very poor value, of merely $\sim\$0.1\ /kg_{O_2}$. It should be therefore of obvious interest to explore more appealing oxidative chemistries to boost the techno-economic attractiveness of the PC technology.

The research efforts reported in the following work fit in this specific framework, endowing to the development of alternative strategies to upgrade H_2 production via PC pathways.

Firstly, Chapter 2 provides the theoretical background to understand solar-to-chemical conversion, with greater emphasis given to semiconductor photo-active systems. Specifically, the true workforce of our investigation is represented by hybrid inorganic semiconductor nanostructures, to which is dedicated a detailed overview of the synthetic development and optoelectronic properties.

The bulk of the experimental research findings are the detailed in Chapter 3. In this section, closed-cycle redox transformations, promoted by metal-chalcogenide based PC, demonstrate efficient H_2 generation occurring along the simultaneous production of value-added oxidative products. The so obtained solar-to-chemical energy conversion process provides an insightful opportunity to prospectively merge the affine research fields of photoredox catalysis and solar-to-hydrogen conversion.

Later, Chapter 4 extends such strategy with explorative studies on more full-cycle red-ox transformations. The development of alternative photo-reductive and photo-oxidative processes is especially conceived with the final target of integrating PC systems in micro-fluidic flow reactors. Overall, a proof-of-concept demonstration of efficient photochemical devices is provided, following the pledge to realise a solar-economy as envisioned by Ciamician in 1912[14].

References

1. Pearson, P. N. & Palmer, M. R. Atmospheric carbon dioxide concentrations over the past 60 million years. *Nature* **406**, 695–699 (2000).
2. Sapart, C. J. *et al.* Natural and anthropogenic variations in methane sources during the past two millennia. *Nature* **490**, 85–88 (2012).
3. Cook, J. *et al.* Consensus on consensus: a synthesis of consensus estimates on human-caused global warming. *Environ. Res. Lett.* **11**, 1–7 (2016).
4. *World Energy Outlook 2018*. *International Energy Agency Publications* (2018).
5. Lewis, N. S. & Nocera, D. G. Powering the planet: Chemical challenges in solar energy utilization. *Proc. Natl. Acad. Sci.* **103**, 15729–15735 (2006).
6. Tachibana, Y., Vayssieres, L. & Durrant, J. R. Artificial photosynthesis for solar water-splitting. *Nat. Photonics* **6**, 511–518 (2012).
7. Kornienko, N., Zhang, J. Z., Sakimoto, K. K., Yang, P. & Reisner, E. Interfacing nature's catalytic machinery with synthetic materials for semi-artificial photosynthesis. *Nat. Nanotechnol.* **13**, 890–899 (2018).
8. United States Department of Energy. *DOE Technical Targets for Hydrogen Production from Photoelectrochemical Water Splitting*. (2011).
9. Japanese Ministerial Council on Renewable Energy - Hydrogen and Related Issues. *Basic Hydrogen Strategy*. (2017).
10. Jang, J.-W. *et al.* Toward practical solar hydrogen production-an artificial photosynthetic leaf-to-farm challenge. *Chem. Soc. Rev.* **48**, 1908–1971 (2019).
11. Goto, Y. *et al.* A Particulate Photocatalyst Water-Splitting Panel for Large-Scale Solar Hydrogen Generation. *Joule* **2**, 509–520 (2018).
12. Hisatomi, T. & Domen, K. Reaction systems for solar hydrogen production via water splitting with particulate semiconductor photocatalysts. *Nat. Catal.* **2**, 387–399 (2019).
13. Fabian, D. M. *et al.* Particle suspension reactors and materials for solar-driven water splitting. *Energy Environ. Sci.* **8**, 2825–2850 (2015).
14. Ciamician, G. The photochemistry of the future. *Science.* **36**, 385–394 (1912).

Chapter 2 Theoretical Background

2.1 Light as a Chemical Reagent

2.1.1 Photochemistry and Photophysics

Light-matter interaction is a ubiquitous topic investigated across a wide spectrum of scientific disciplines. From the definition of the corpuscular theory from Newton to the quantum-mechanical model developed in the last century, optical phenomena understanding has progressed thanks to pioneering contributions in the fields of mathematics, physics, chemistry and engineering. Its relevance is highlighted by the birth of distinct research branches such as photochemistry and photophysics, that fundamentally differ from the parent disciplines. Focusing on the former case, while traditional chemical investigation has been dedicating to ground-state phenomena, photochemistry deals with *excited-state* behaviour of chemical entities. This distinction predominantly entails the transition from thermal to light-promoted chemical reactions.

Photochemistry, according to IUPAC definition, deals with the "*chemical effects of light (far UV to IR)*"[15], where a specific portion of the electromagnetic spectrum, enclosed between 200 and 1000 nm, is of primary importance. According to the quantum model, radiation propagates in the form of electromagnetic waves carrying discrete radiant energies, defined by the formula:

$$E = h\nu = \frac{hc}{\lambda} \qquad \textbf{2.1}$$

where h is the Planck constant ($6.626 \cdot 10^{-34}$ [Js]), c the light speed (299792458 [ms^{-1}]), while ν and λ the characteristic radiation frequency and wavelength. Photons in the optical region of photochemical interest carry an energy content ranging from 240 kcal mol^{-1} (200 nm) to 28 kcal mol^{-1} (1000 nm), that are in large excess compared to bond dissociation energy for C-N (70 kcal mol^{-1}), C-C (83 kcal mol^{-1}), C-H (100 kcal mol^{-1}) and O-H (105 kcal mol^{-1}) chemical bonds. As

summarised in Figure 2.1, optical radiation can therefore provide a powerful driving force to promote chemical reactions with respect to thermal pathways[16].

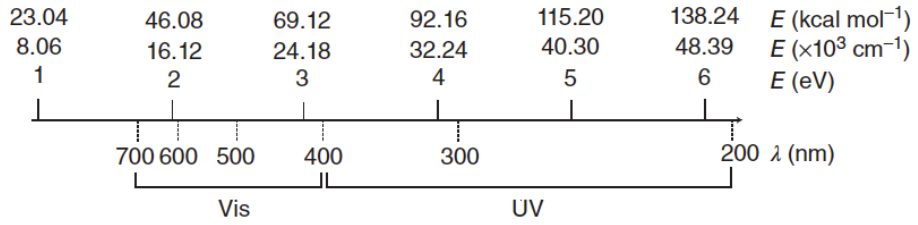

Figure 2.1. **Energy scale bar showing relevant values for UV-visible driven photochemical reactions**[2].

Remarkably, the quantised nature of light has fundamental implications not only in the field of energy conversion, but also in information sciences such as quantum computing, cryptography, communication and, lastly, for human vision.

In general, regardless of its exploitation as an energy or information carrier, light absorption is the inceptive event of radiation conversion. Focusing on the description of molecules dissolved in homogeneous fluid media, Lambert-Beer law defines light attenuation from such particles according to the formula:

$$I(l) = I_0 e^{-A(l)} \quad with \quad A(l) = \varepsilon c l \qquad \textbf{2.2}$$

This equation describes the exponential decay of the incoming light intensity, I_0, throughout the medium as a function of particle absorbance, A. The latter adimensional quantity depends in turn by the particle molar absorption coefficient (ε [$M^{-1}cm^{-1}$]), concentration (c [M]) and optical path length (l [cm]). Light absorption is an extremely fast event - occurring on the $10^{-15}\ s$ timescale – and is typically followed by vibrational relaxations ($10^{-12}\ s$) and internal conversion ($10^{-15}\ s$) whenever excited states higher than the first one are populated. The fate of excited states is then described by photophysical and photochemical decay processes, which depend by both intrinsic phenomena and presence of foreign species in solution. To this extent, unimolecular processes describes the deactivation pathways of non-interacting particles, on the other hand, bimolecular ones introduce additional transitions to the ground state according to the type of interaction between excited species and foreign moieties.

Firstly, unimolecular processes describe first-order transitions that can be schematically summarised as follows:

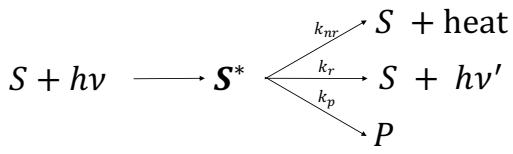

According to this scenario, the excited species $\boldsymbol{S}^*$ decay via non-radiative, radiative (photophysical processes) or photochemical pathways, with an overall first-order rate constant accounting for all competing processes:

$$k_{unim} = k_{nr} + k_r + k_p \qquad \textbf{2.3}$$

The population of excited states extends for a limited lifetime; conventionally, such quantity is defined as the time window delimited by the reduction of the concentration of $\boldsymbol{S}^*$ to $1/e$ of the initial amount:

$$\tau_0(\boldsymbol{S}^*) = \frac{1}{k_{nr} + k_r + k_p} = \frac{1}{\sum_i k_{nr} + k_r + k_p} \qquad \textbf{2.4}$$

Notably, the excited-state lifetime is both dependent on temperature and fluid media where particles are dissolved. For example, higher temperatures accelerate non-radiative deactivation mechanisms, whereas radiative phenomena are negligibly influenced by this parameter.

In order to quantify the different deactivation mechanism affecting the lifetime, it is convenient to define the quantum yield of a primary process, i.e. a process initiated by light absorption and resulting in the disappearance of the photo-activated species:

$$\Phi_i = \frac{\text{number of species undergoing process } i}{\text{number of photons absorbed}} \qquad \textbf{2.5}$$

Similarly, process efficiency defines the ratio of successful events i over the sum of competing processes:

$$\eta_j = \frac{k_j}{\sum_i k_i} = k_i \tau(\boldsymbol{S}^*) \qquad \textbf{2.6}$$

allowing to establish the non-radiative ($\eta_{nr} = k_{nr}\tau$), radiative ($\eta_r = k_r\tau$) and photochemical ($\eta_p = k_p\tau$) efficiencies. Within this framework, the first process, that entails the "degradation to heat" of the excited state, is often regarded as a loss mechanism, yet photo-thermal therapies make use of such heat for medical treatments of carcinogenic conditions. On the contrary, high quantum yields for photophysical deactivation by light emission are highly desirable for a several of applications; in fact, it is a fundamental prerequisite also for highly efficient light-to-chemical energy conversion, as explained in the next paragraph. Light-emission, also known as luminescence, follows quantum-mechanical selection rules, that discriminate between spin allowed (singlet to singlet: $S_1 \rightarrow S_0$) and forbidden transitions (triplet to singlet: $T_1 \rightarrow S_0$). In the former case, luminescence is termed fluorescence, that occurs on timescale of $10^{-6} - 10^{-9}\ s$, while phosphorescence, or long-lived luminescence, occurs on time scales of $10^{-6} - 10^{-2}\ s$ because of the lower probability of optical transition. It is important to note that, according to Kasha's rule, a species cannot display more than two emission bands, thus more than a fluorescence and a phosphoresce band. Finally, a species $\boldsymbol{S}^*$ can deactivate through photochemical pathways, generating a final entity P, thus decaying to a ground-state configuration that is chemically different from that of the original specie S.

The deactivation pathways just described occur for any photo-excited specie, however, if a second population of moieties is present in solution, bimolecular processes should be included in the photophysical and photochemical description of excited states. Analogously to the unimolecular case, bimolecular processes are divided according to their deactivation mechanism:

$$S + h\nu \longrightarrow \boldsymbol{S}^* + Q \begin{cases} \xrightarrow{k_{en}} S + \boldsymbol{Q}^* \\ \xrightarrow{k_{ET}} S^+/S^- + A^{\cdot -}/D^{\cdot +} \\ \xrightarrow{k_{cat}} S + \mathrm{Q} + \mathrm{heat} \end{cases}$$

In this schematic representation it is possible to notice how quencher moieties are responsible for $\boldsymbol{S}^*$ decay via energy transfer, electron transfer or catalytic deactivation.

Energy transfer is at the basis of natural photosynthetic mechanism (antenna effect) and it is generally classified as a radiative or non-radiative process. The former case implies optical interaction, where radiative energy emitted by a first species is harvested by a second species, whereas the latter scenario occurs via coulombic or exchange interaction. Förster-type energy transfer describes coulombic interaction, that is characterised by a long-range concerted mechanism of dipole-dipole interaction. This process is favoured by extensive spectral overlap between the absorption and emission bands of the donor and acceptor moieties. On the other hand, Dexter mechanism requires orbital overlap between the donor and acceptor system, thus occurs at short distance in collisional type events.

Secondly, electron transfer is the inceptive bimolecular event at the foundation of photocatalytic and photosynthetic phenomena. Such processes entail different thermodynamic and kinetic requirements, thus electron transfer plays a fundamentally different role in each scenario. On one hand, while photocatalytic processes are thermodynamically favoured at the ground state, photosynthetic one are not. Within this framework, formation of an excited-state $\boldsymbol{S}^*$ upon light absorption endows electron-transfer with a twofold final outcome: in photo-catalytic mechanisms it simply accelerates reaction kinetics (see Figure 2.2A), while in photosynthetic schemes it effectively allows the reaction to occur (see Figure 2.2B). In short, photo-induced electron transfer exploits light as an accelerating or empowering agent. Notably, chemical-potential storage in realised only by photosynthetic mechanisms.

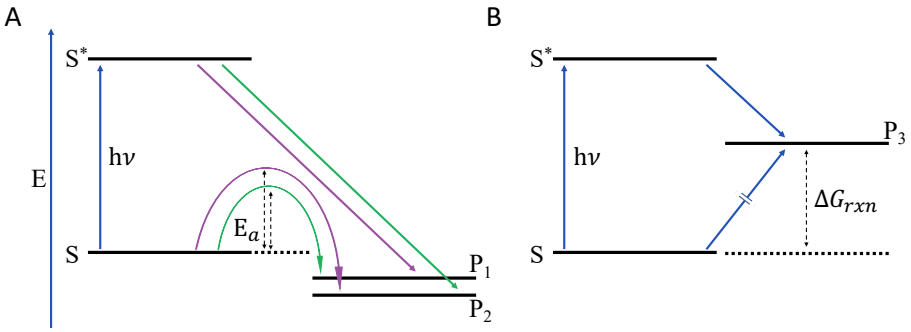

Figure 2.2. ***Schematic illustration of photocatalytic and photosynthetic processes.*** A) Photocatalytic-type process, which is thermodynamically favoured, but kinetically hampered by an activation energy E_a. Faster kinetics can be nevertheless obtained through light-promoted photochemical mechanism, entailing formation of the excited state $\boldsymbol{S}^*$ to obtain the final product P_1 or P_2. The reaction performed is *exothermic* and consequently does *not* store chemical potential. B) Photosynthetic-type process. In this case, product P3 can be obtained only through the formation of the excited state $\boldsymbol{S}^*$. The ground state reaction is thermodynamically unfavoured ($\Delta G_{rxn} > 0$), thus the process effectively store chemical potential through and endergonic reaction.

Other quenching processes include catalytic deactivation, where the collisional interaction enhances non-radiative decay, and formation of excimers and exciplexes, which are supramolecular species forming in specific conditions.

Overall, intermolecular interaction between a species $\boldsymbol{S}^*$ and a quencher Q encompasses additional deactivation mechanisms, that result in the complete time evolution of $\boldsymbol{S}^*$ as the sum of intra- and intermolecular contributions:

$$-\frac{d[\boldsymbol{S}^*]}{dt} = \left(k_{nr} + k_r + k_p + k_q[Q]\right)[\boldsymbol{S}^*] \qquad \textbf{2.7}$$

where quenching-promoted decay to the ground-state stems from rate constant $k_q = k_{en} + k_{ET} + k_{cat}$. The presence of quencher moieties necessarily affects the lifetime of $\boldsymbol{S}^*$, that is accordingly expressed by:

$$\tau(\boldsymbol{S}^*) = \frac{1}{k_{nr} + k_r + k_p + k_q[Q]} \qquad \textbf{2.8}$$

By substitution in equation 2.7 of the lifetime previously defined for solely unimolecular decay (τ^0), it is possible to define, after mathematical rearrangement, the Stern-Volmer relation as follows:

$$\frac{\tau^0}{\tau} = 1 + k_{SV}[Q] \qquad \textbf{2.9}$$

in which $k_{SV} = \tau^0 k_q$ is the Stern-Volmer constant. This equation covers a fundamental importance in photochemical phenomena, expressing the efficiency for chemical potential exchange between species in liquid solution. Specifically, when considering the diffusion-controlled bimolecular rate constant k_d, that has typical values in the interval $0.1 < k_d < 2\ 10^{10} M^{-1} s^{-1}$, the quenching efficiency is expressed by $\Phi_q = \mathrm{k}_q/\mathrm{k}_d$. Exact calculation of the maximum value of k_d can be performed using the Smoluchowski equation:

$$\mathrm{k}_d = 4\pi N_A (R_{\boldsymbol{S}^*} + R_Q)(D_{\boldsymbol{S}^*} + D_Q) \qquad \textbf{2.10}$$

where $R_{\boldsymbol{i}}$ and $D_{\boldsymbol{i}}$ are the collisional radii and diffusion coefficients, respectively, of species $\boldsymbol{S}^*$and Q.

On a practical point of view, the Stern-Volmer equation allows the estimation of the minimal concentration of quencher necessary to deactivate the excited state. For example, in the limiting scenario of maximal quenching ($k_q = k_d$), the population of a species $\boldsymbol{S}^*$, having a lifetime of $1ns$, requires $0.1\ M$ of quencher to reduce half of its size. Alternatively, assuming the same collisional efficiency, the minimum lifetime required to quench half of $\boldsymbol{S}^*$ excited states with a quencher concentration of $0.001\ M$ would be $100\ ns$.

It is worth noting that a Stern-Volmer plot can be experimentally obtained not only by measurements of the excited-state lifetime throughout a titration experiment, but also following the decrease in emission intensity or in luminescence quantum yield following consecutive addition of quencher. To this extent, simultaneous measurement of emission and lifetime decays reveals crucial aspects of the quenching mechanism. In particular, dynamic quenching is validated by superimposed Stern-Volmer relationship for the emission and lifetime behaviours, whereas static quenching displays a decreasing emission intensity, but unaltered lifetime trend, as a function of quencher concentration. Physically, the latter evidence is explained by the formation of a non-luminescent association complex between $\boldsymbol{S}^*$ and Q: a growing population of association complexes reduces

the overall emission intensity registered, however, the lifetime of the un-associated and luminescent species remains unaffected.

2.1.2 Solar-to-chemical energy conversion

The rising energy thirst to power our civilisation is depleting the resources of the Spaceship Earth at an unsustainable pace. The present worldwide energy consumption rate amounts to ~15 TW, with ~81% of this share being provided by fossil feedstocks like oil, coal and gas[4]. Nevertheless, the magnitude of our energy need is incomparably small with respect to 120'000 TW that the sun provides us yearly. This inexhaustible amount of energy exceeds in turn the one offered by all other renewable resources summed up[17]. As a result, solar energy harvesting represents the ultimate process that is prospected to sustain the Anthropocene.

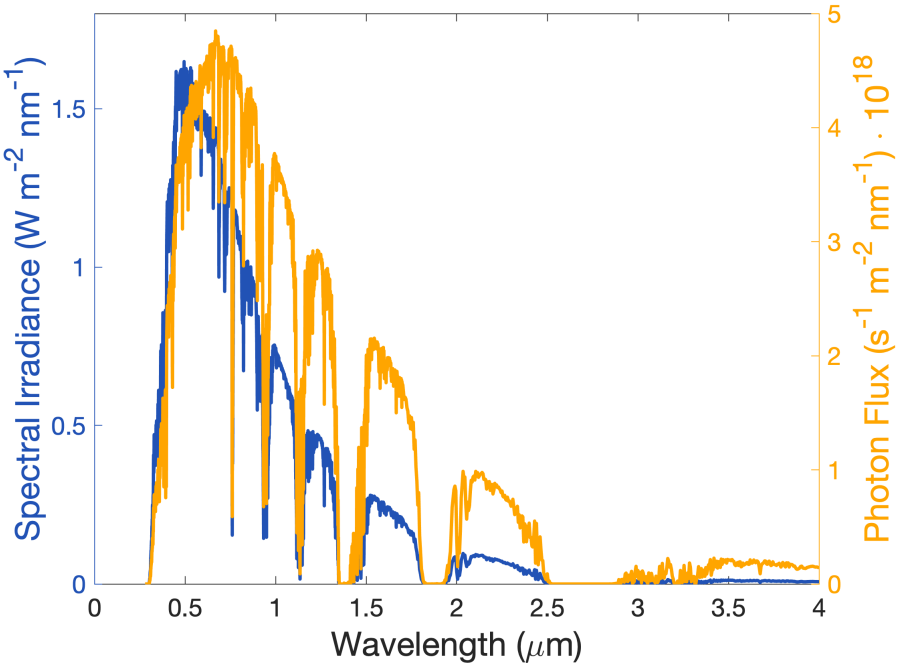

Figure 2.3. **Reference AM1.5G Spectral Irradiance and photon flux.**

Solar radiation spreads in the electromagnetic spectrum from 280 nm to 4000 nm and its photon distribution is commonly separated into ultraviolet (5%), visible (43%) and infrared (52%) regions. Travelling through the Earth's atmosphere, part of the radiation is filtered by O_3, H_2O, CO_2 and other atmospheric gases, whose

absorption bands attenuates power density to an average 1 kWm^{-2} at sea level. The spectral profile at Earth's surfaces, known as AM1.5G, is displayed in Figure 2.3 and represents the reference solar irradiance for efficiency comparison. Under optimal conditions, AM1.5G spectrum represents only 75% of the extra-terrestrial irradiance, referred as AM0G[18]. Taking into account scattering by particulate matter in the air and shading from clouds, solar radiation is further reduced to an yearly average of 170 Wm^{-2} [19].

Therefore, the diluted and intermittent nature of sunlight compelled the quest for optical devices capable of capturing and storing solar radiation. The development of direct solar energy conversion systems (not involving thermal steps) was accomplished through threshold devices that, above a minimum energy E_g (corresponding to a maximum threshold wavelength λ_g), trigger photochemical or photophysical processes[20]. Therefore, for a general photochemical endergonic process promoted by an absorber S, net energy storage is achieved through excitation of S to its excited state $\boldsymbol{S}^*$ (with $\boldsymbol{S}^* - S = E_g$) and successive generation of a product P, as depicted in Figure 2.4A. Three fundamental losses plague photochemical phenomena:

- Photons with $E < E_g$ cannot promote S to $\boldsymbol{S}^*$, hampering the photochemical event,
- Photons generating optical transitions with energies $E > E_g$, thermally equilibrate on a picosecond's timescale at $E = E_g$, dissipating the excess energy as heat and
- Conversion of solar into chemical potential succeed only if the transition from $\boldsymbol{S}^*$ to P proceed through an exergonic barrier. As depicted in Figure 2.4A, this condition entails the presence of an activation energy E_r^*, which avoids the back reaction and grants chemical stability to the species P.

A quantitative assessment of the first two parasitic processes follows from fundamental thermodynamic considerations first described by Ross and Hsiao[21]. To this extent, a thorough coverage of the solar-to-chemical energy conversion framework was described by Bolton, to which the interested reader is referred for a comprehensive overview of the concepts explained in the present paragraph[20,22–25].

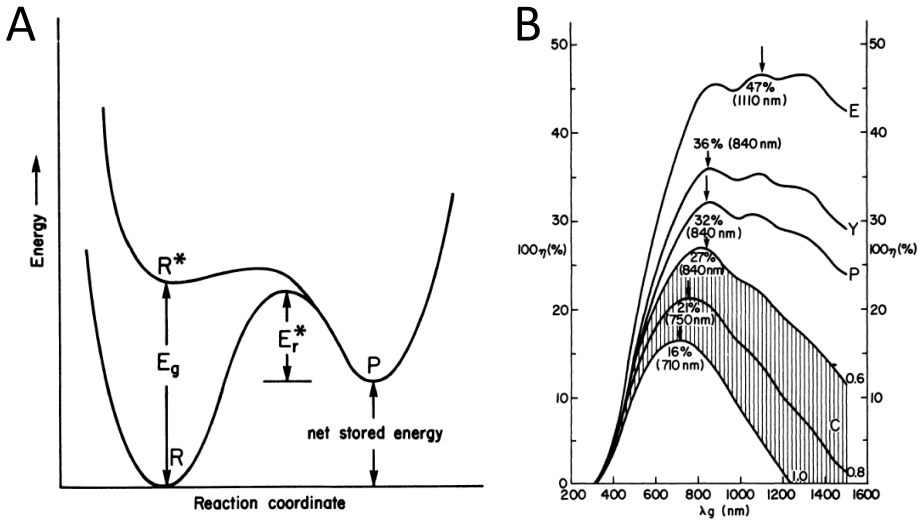

Figure 2.4. **Photochemical energy conversion: basic principle and maximum thermodynamic efficiency[8].**

A) Schematic representation of photochemical energy conversion, where product P is obtained after promotion of S to its excited state $\boldsymbol{S^*}$**,** separated by an energy barrier E_g. E_r^* is the activation energy preventing back reaction. B) Efficiency of solar-to-chemical energy conversion as a function of band-gap wavelength λ_g: curves E, Y, P and C are obtained by considering different thermodynamic and kinetic limitation.

Firstly, it was anticipated that a photo-active species is a threshold system display a total absorbed photon flux, J_e, partitioned by a characteristic band-gap wavelength, λ_g:

$$J_e = \int_0^{\lambda_g} I_S(\lambda)\alpha(\lambda)\, d\lambda \quad [\, s^{-1}m^{-2}nm^{-1}] \qquad \textbf{2.11}$$

where I_S ($[\, m^{-2}\, s^{-1}\, nm^{-1}\,]$) is the incident solar photon flux and $\alpha(\lambda)$ ($[\, m^{-1}\,]$) the photo-active species absorption coefficient.

In the second place, thermalisation effects impose harvesting of the solar power at the band-gap energy. Thus, it possible to define the *energy yield* E as the rate of excitation multiplied for E_g:

$$E = J_e \frac{hc}{\lambda_g} \quad [\, Wm^{-2}\,] \qquad \textbf{2.12}$$

with hc representing the product of Planck constant ($[\, J\, s\,]$) and light speed ($[\, m\, s^{-2}\,]$).

In line with the definition of *ultimate efficiency* of a solar cell provided by Shockley and Queisser[26], the fraction η_E of incident solar radiation available to promote photochemical reactions can be expressed as:

$$\eta_E = \frac{E}{\int_0^\infty E(\lambda)d\lambda} \qquad \textbf{2.13}$$

where the of Equation 2.13 refers to total incident power, i.e. $1\ kWm^{-2}$ for AM1.5G spectrum. Curve E in Figure 2.4B displays the spectral trend of η_E, which peaks at a value of 47% for a band-gap $\lambda_g = 1110\ nm$.

Efficient solar energy converter should however achieve maximum power, not maximum energy yield. In physics, power is defined as the product of the flux of quantity times the corresponding potential gradient, which is the thermodynamic driving force leading to dissipative fluxes. Maxwell elegantly described this concept for all the basic thermodynamics variables[27]:

"*The pressure is the intensity of the tendency of the body to expand, the temperature is the intensity of its tendency to part with heat, and the potential of any component is the intensity with which it tends to expel that substance from its mass.*"

In chemical thermodynamics terms, power can be therefore expressed as the rate of photo-product times the free-energy difference between starting reagent and photoproduct, i.e. the reaction chemical potential.

In real systems, the rate of photoproduct formation can reach the absorption rate, however the thermodynamic potential carried by photoproducts is less than E_g. Accounting for entropic losses, Ross and Hsiao computed the maximum chemical potential, μ_{max}, as:

$$\mu_{max} = RT\frac{ln\int_0^{\lambda_g} I_S(\lambda)\,d\lambda}{ln\int_0^{\lambda_g} I_{BB}(\lambda)\,d\lambda} \quad [J\ mol^{-1}] \qquad \textbf{2.14}$$

where R refers to the universal gas constant ($[\,K\ mol^{-1}\,]$), while and I_{BB} ($[\,m^{-2}\ s^{-1}\ nm^{-1}\,]$) is the blackbody photon flux. In analogy to solar cells working operations, the product of μ_{max} times the maximum photo-reaction flux was defined as *open-circuit yield*:

$$Y = J_e \mu_{max} \quad [\, W m^{-2} \,] \qquad \textbf{2.15}$$

This formula expresses the maximum thermodynamic photochemical power yield and applies generally to any conversion of solar power to electricity or stored chemical energy. Consistently, maximum thermodynamic efficiency is defined as followed:

$$\eta_Y = \frac{Y}{\int_0^\infty E(\lambda) d\lambda} \qquad \textbf{2.16}$$

Shockley and Queisser termed *nominal efficiency* the analogous ratio of open-circuit yield and incident radiation for solar to electrical energy conversion.

It should be noted that Y, assuming a maximum value of 36% at 840nm (Figure 2.4B), is the yield obtainable only under reversible conversion of the chemically stored energy, i.e. when energy is drawn into storage infinitesimally slowly. Consequently, in order to simultaneously maximise both photoproduct rate and chemical storage generation, it is necessary to lower μ_{max}. This is physically achieved by considering competing optical processes such as luminescence yet excluding non-radiative decay pathways. Thus, maximum yield under condition of maximum rate is expressed by:

$$Y = J_e (1 - \varphi_{loss}) \mu_{max} \quad [\, W m^{-2} \,] \qquad \textbf{2.17}$$

With $\varphi_{loss} \approx RT/\mu_{max}$ representing the fraction of absorbed quanta lost from the excited state.

Using previous definitions, optimal energy storage rate can be expressed as follows:

$$P = J_e \left[\mu_{max} - RT \, ln \left(\frac{\mu_{max}}{RT} \right) \right] \cdot \left[1 - \frac{RT}{\mu_{max}} \right] \quad [\, W m^{-2} \,] \qquad \textbf{2.18}$$

Then, the limiting fraction of solar power which can be converted into chemical energy is:

$$\eta_P = \frac{P}{\int_0^\infty E(\lambda) d\lambda} \qquad \textbf{2.19}$$

Figure 2.3B shows how curve P peaks at 32% at 840nm.

Finally, the third fundamental parasitic mechanism imposes kinetic limitation to the ideal thermodynamic limits just computed. For first-order photochemical processes, E_r^* scales logarithmically with respect to product lifetime, creating an energy barrier at the expense of available storage energy. A comprehensive *chemical yield* can be defined as:

$$C = E \cdot \eta_{chem} \quad [\, Wm^{-2} \,] \qquad \textbf{2.20}$$

$$\eta_{chem} = \frac{\Delta G_{rxn}}{E_g} \quad [\, Wm^{-2} \,] \qquad \textbf{2.21}$$

where ΔG_{rxn} is the net free energy storage of the photochemical process. Then:

$$\eta_C = \frac{C}{\int_0^\infty E(\lambda) d\lambda} = \eta_E \cdot \eta_{chem} \qquad \textbf{2.22}$$

Figure 2.4B shows how, by increasing product lifetime from 1 ms ($E_r^* = 0.6\ eV$) to 1s ($E_r^* = 1\ eV$), C decreases from a maximum of 27% to 16% efficiency.

2.1.3 Natural and Artificial Photosynthesis

Life on Earth has blossomed thanks to the process of natural photosynthesis (NPs). This was first realised by photoauto- and photoheterotrophic organisms but nowadays it is also mimicked by modern artificial devices. In natural systems like plants, algae and cyanobacteria, photosynthesis provides energy to the organism in the form of chemical bonds, i.e. carbohydrates. Such products are obtained through concerting reactions that are summarised by the following formula:

$$6CO_2 + 6H_2O + photons \rightarrow C_6H_{12}O_6 + O_2$$

where glucose is synthesised, along O_2 as by-products, through an endothermic reaction requiring $2870\ kJ\ mol^{-1}$. Water is used as an electron donor in the first part of the process, however, a class of microbes makes use of arsenite instead of it. Overall, it was estimated that, on a global scale, energy is captured at a rate of $120\ TW$ by natural systems[5], that approximately convert $100 - 115\ Gtons$ of carbon into biomass every year.

Natural photosynthetic processes have developed differently according to the ecosystem and evolution history of the various systems, yet three fundamental mechanisms are common to all of them:

- Light-absorption by antenna complexes;
- Charge separation across a membrane via reaction centre (RC) proteins;
- "Fuel-forming" redox reactions.

Firstly, trans-membrane pigment protein complexes - chlorophylls, carotenes, xanthophylls - harvest solar radiation over a broad spectral range, as depicted in Figure 2.5[28].

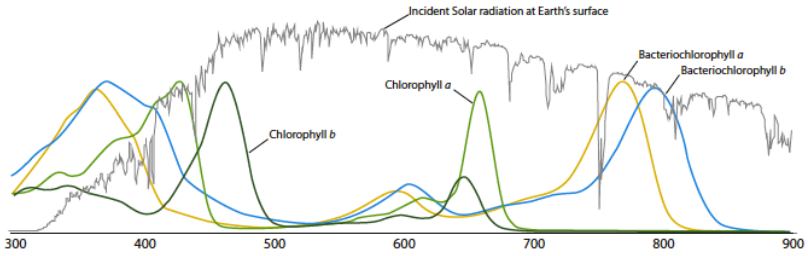

Figure 2.5. **Absorption spectra of different natural light-harvesting chromophores[17].**

Optimal light absorption is then achieved by a precise spatial and energetic photosystems architecture, that provided conceptual inspiration for the realisation of artificial devices. Antenna systems are indeed arranged in a multimeric ring structure that concentrically funnels exciton energy towards the RC. This spatial organisation maximises exciton energy transfer by broadening electronic resonance, thus promoting Förster and Dexter processes at high rates. The delicate architecture is held together by polypeptides, whereas carotenoids, apart from harvesting light, provide protection to the unit against photooxidation by quenching singlet oxygen formed in the redox reactions. As depicted in the scheme in Figure 2.6A, photo-induced charge carriers generated in the chlorophyll pigment in photosystem II (PS-II) are then pumped towards the RC through photosystems I (PS-I), where a second excitation endow excited electrons with the necessary chemical potential to perform water splitting. The so called "Z-scheme" electronic landscape terminates, on the PS-II ends, with a manganese calcium oxide cluster performing water oxidation and, on the PS-I end, with the nicotinamide adenine dinucleotide phosphate (NADP) reductase. This enzyme catalyses the reduction of

NADP to NADPH, which is used as a reducing equivalent in the successive carbon dioxide conversion cycle. Remarkably, high reaction quantum yields are achieved thanks to long-lived charge separation, ensuing from coordination of energetics, electronic couplings and reorganisation energies.

Overall, energy storage is performed by natural organisms through the creation of a reduced species of strongly negative redox potential, that is successively employed in the synthesis of a renewable fuel. To this extent, artificial photochemical devices aim to store the chemical potential provided by solar radiation in a chemical reductant, or solar fuel, that can ideally be transported, stored and used on demand. Taking inspiration from nature, several photochemical architectures for solar-to-chemical energy conversion have been developed over the last 50 years, as schematically depicted in Figure 2.6B[6].

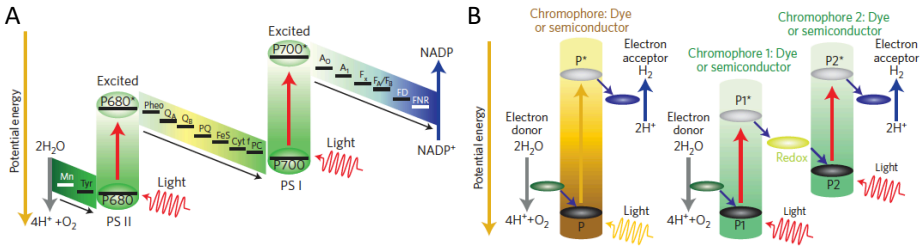

Figure 2.6. **Schematic illustration of natural and artificial photosynthetic architectures[18].**

A) Schematic Z-scheme reaction energy arrangement showing the sequential energy-transfer pathway connecting PSII to PSI. B) Artificial counterparts of the natural photosynthetic architecture, schematically showing one and two photosynthetic units' systems.

Firstly, a seminal contribution in the field was advanced by Fujishima and Honda in 1972[29]. The authors briefly reported electrochemical photolysis of water promoted by a semiconducting TiO_2 electrode. In such device, ultraviolet photogenerated charge carriers are separated through an external circuit between the anatase photoanode and Pt cathode. Through the application of electrical ($0.5\ V$) and chemical bias ($pH = 4.7$), the cell reported a quantum efficiency of 0.1. In spite of the remarkable scientific achievement, excluding the visible region from light harvesting greatly limits solar-to-chemical energy conversion. As a result, Lehn and Sauvage brilliantly circumvented this limitation by alleviating the double burden of light absorption and catalytic functions to different molecular units[30]. Their

photochemical system consisted indeed of a $Ru(bipy)_3^{2+}$ photosensitiser coupled to a $Rh(bipy)_3^{3+}$ redox relay species. Both components featured indeed optimised properties for the respective operation: Ru-complexes display intense visible light absorption ($\lambda_{max} = 452nm,\ \varepsilon_{max} = 14600M^{-1}cm^{-1}$), long-lived excited-state phosphorescence ($\Phi = 0.04,\quad \tau = 0.6\mu s$) and excellent redox potentials($+0.84V\ /-0.86V$ vs NHE), whereas Rh-complexes are simultaneously able to be reduced by the photosensitiser and reduce H_2O following accumulation of two electrons at the same reduction potential. According to the scheme of Figure 2.7A, Ru cycles between light absorption, oxidative quenching by a donor moiety and final regeneration promoted by a sacrificial reagent. The disproportionation reaction prevents back electron transfer and activates the Rh cycle, which in turns reduces a Pt-salt that acts as water reduction catalyst. This elegant homogenous photosynthetic scheme, which employs the $Ru(bipy)_3^{2+}$ / $Rh(bipy)_3^{3+}$ / triethanolamine / K_2PtCl_4 4-component systems, represents a first imitation of the efficient and concerted NPs counterpart. In 1979, Bard developed such artificial process further by proposing a Z-Scheme where a pair of n-type semiconductor nanoparticle systems (SCS-I + SCS-II) separately perform water oxidation and reduction half-reactions[31]. Remarkably, this paper highlights the advantage of using particulate systems, that allow a wider gallery of materials to be exploited for photosynthetic applications, as opposed to the complicated preparation of single crystals/polycrystalline electrodes for similar purposes.

Although tandem configurations offer a wider redox potential window for the photochemical reaction, inherent efficiency losses arise because of the use of two photons per molecules of water that is splitted. Grätzel cleverly surpassed this limitations by designing a bifunctional colloidal semiconductor nanostructure, as depicted in Figure 2.7B[32]. Revamping the use of TiO_2, the author reported a modular system where the semiconductor was decorated by separate Pt and RuO_2 junctions, allowing for distinct development of each catalytic site within a single photosynthetic unit. Vectorial displacement of electron and hole towards Pt and RuO_2 compartments, respectively, accelerated the transfer of photo-generated charge carriers to the aqueous solution, inhibiting e^-/h^+ recombination and yielding an improved 5% quantum yield.

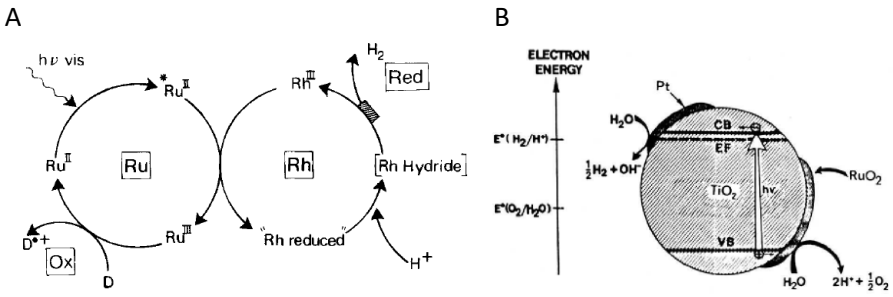

Figure 2.7. **Artificial photosynthetic schemes developed by Lehn-Sauvage[20] and Grätzel[22].**
A) Four component system comprising $Ru(bipy)_3^{2+}$(Ru), $Rh(bipy)_3^{3+}$(Rh), triethanolamine and K_2PtCl_4. B) Single photosynthetic used based on semiconducting titania nanoparticles including distinct reaction sites for reduction and oxidation half-cycles, namely Pt and RuO_2 islands.

These early reports of artificial photosynthetic devices constitute in fact the fundamental system architectures closely mimicking NPs design, upon which successive improvements in materials design and reaction conditions originated to realise efficient overall water splitting. Research efforts especially concentrated on extending spectral response for light absorption, improving exciton management and enhancing surface reactions yields[33]. To date, practical solar-to-chemical energy conversion is far from being accomplished[10,34], yet particulate semiconductor systems are designated as the most promising photochemical architecture in achieving such target[12].

2.2 Semiconductor-Based Photochemical Devices

2.2.1 Semiconductor Nanostructures

Semiconductor materials stroke at the root of the digital revolution but also in many other fields, such as in optoelectronics, bioimaging and sensing. This class of materials represent the building blocks of most photochemical device, whose working principles are strictly interwoven with semiconductor instrinsic properties.

Direct solar-to-chemical energy conversion is in fact efficiently operated when a material with specific optoelectronic properties is used as the active component. In particular, photochemical systems should present excellent light absorption and charge carriers transport under illumination. To this extent, semiconductors provide excellent electrical transport characteristics, yet under specific conditions. This property is perfectly reflected in the band-structure picture that differentiates them from metals and insulators. In solid-state physics, the band structure describes the energy-momentum (E_k) relationship of a compound, yielding macroscopic-scale properties through a microscopic-scale description of the architecture of the material. This results from Bloch theorem, which allows to simplify the Schrödinger equation problem if a periodic potential is assumed to extend over the three dimensions of the crystal lattice. Under these assumptions, E_k can be safely considered as periodic in the reciprocal lattice, i.e. the basis lattice in momentum-/k-space or the Fourier transform of the physical lattice. Provided the periodicity of E_k, it is thus sufficient to define the energy-momentum space within the primitive cell of the reciprocal lattice, called Brillouin zone, to fully characterise the solid-state properties of the materials.

In Figure 2.8 is pictured as an example the Brillouin zone of CdS[35], one of the prototypical semiconductors extensively used in the optoelectronics community. At first, it is possible to distinguish the valence band (VB) and the conduction band (CB), that are formed by the available energy states of a material. In thermal equilibrium, the former is made up of occupied energy levels ("low-energy" region), while the latter comprise unoccupied one ("high-energy" region). Valence and conduction band are separated by an energy gap, that is defined as:

$$E_g = E_c - E_v \qquad \textbf{2.23}$$

with E_c and E_V ($[J]$) being respectively the minimum and maximum of the energy of the CB and VB. It can be noted that in CdS E_C and E_V occur at the same k-value, or at the centre of the Brillouin zone (Γ point), and materials characterised by this property are called direct-band semiconductors. This property is of fundamental importance when considering optical transitions: while in direct-band semiconductors such phenomena occur without any change in the initial and final

momentum value, absorption or emission processes in indirect-band semiconductors, like Si and Ge, require a momentum-transfer event in order to occur. This means that a transfer of phonon (crystal lattice vibration) must mediate such optical transitions, resulting in net weaker absorption properties.

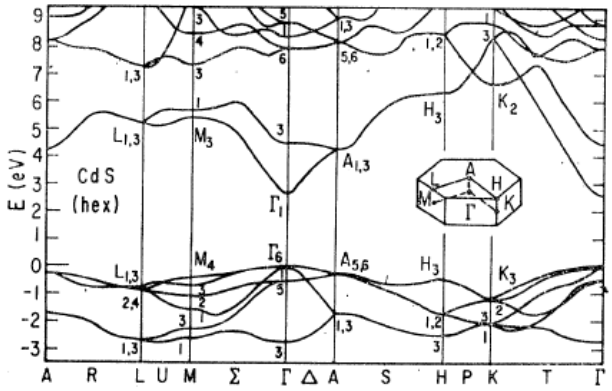

Figure 2.8. **Electronic band-structure of hexagonal CdS[27].**

In this physical framework, semiconductors optoelectronic properties are assumed to be constant in the bulk phase, however, the development of cluster science has evidenced fundamental evolution of intrinsic properties in the transition from extended crystal structures to isolated atoms[36]. Specifically, semiconductor nano-crystallites properties are dominated by spatial confinement of excitation. As a consequence, remarkable variations of optical, electronic and magnetic properties arise when systems with reduced dimensionality display a higher ratio of surface-to-bulk atoms, leading to the onset of quantum-size effects. Such confined systems reveal the dual-nature of charge carriers, which can no longer be described by means of periodically bounded potential, but rather require the quantum-mechanical description of "particles in a box". For a quantised system - in the regime below $\sim 10\ nm$ – continuous electronic bands collapse into discrete energy levels E_n described by the solution of Schrödinger equation imposing vanishing wavefunction, i.e. infinite potential, at the border of the box:

$$E_n = \frac{\hbar^2 \pi}{2ma^2} n \qquad \textbf{2.24}$$

where confined energy results inversely proportional to the square of the size of the box (a), while $\hbar$ ([$J\ s$]) and m ([kg]) represent the reduced Planck constant and

carrier's effective mass. Energy eigenfunction can be therefore interpreted as superposition of bulk E_k states, where $a \to \infty$ and energy bands are continuous. Development of such discrete features is experimentally evinced by absorption and luminescence spectroscopy, as can be seen in Figure 2.9.

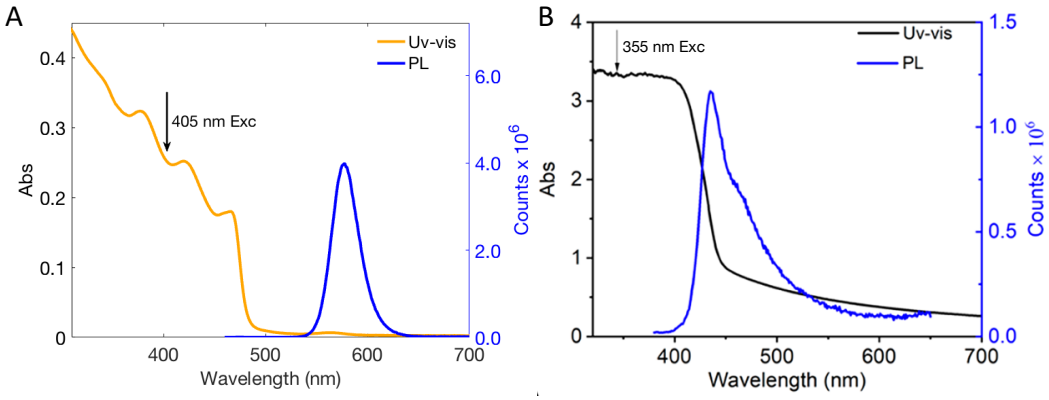

Figure 2.9. **Absorption and Emission spectra of CdSe@CdS nanorods and graphitic carbon-nitride.**

A) Absorption (left-hand side axis, orange curve) and emission spectra (right-hand side axis, blue curve) of core-shell CdSe@CdS nanostructures synthesised in this thesis. B) Absorption (left-hand side axis, black curve) and emission spectra (right-hand side axis, blue curve) of graphitic carbon nitride as reported by Reisner, Durrant et al.[29]. Excitation Wavelength for fluorescence spectra is reported on the graphs.

When optically excited, nanostructured CdS semiconductor concentrates oscillator strength in just a few sharp transitions above E_g, designated by wavy lines above absorption onset, indicating highly monodispersed samples. Moreover, band-edge radiative recombination gives rise to intense emission lines, having narrow full-width half-maxima, where high quantum yields differentiates them from other stochastic nanostructured semiconductors such as carbon nitride[37](Figure 2.9B).

Semiconductors are peculiar because quantum features occur at relatively larger size with respect to metals and insulator. A simplified picture of quantum size-effects for nanostructures systems of different dimensionality is presented in Figure 2.10[38].

Here it is possible to notice that the energy level spacing and associated density of states (DOS) assume different landscapes for materials that are confined in 1, 2 or 3 dimensions. In the transition from bulk configurations, where DOS is proportional to $\sqrt{E}$, to confined systems, the Heavyside step-function accounts for

the “Coulomb blockade” effects, where individual charging event are inhibited by a staircase energy ladder.

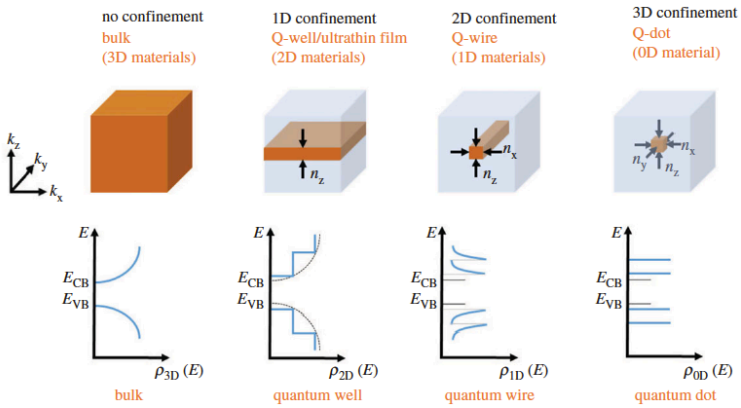

Figure 2.10. **Schematic illustration of change in density of states occurring upon going from bulk to 1D, 2D and 3D quantum systems.**

A further immediate consequence of quantum size effects is exhibited in band-gap energy variation, that is defined as follows:

$$E_g = E_{g,bulk} + E_q + E_c \qquad \textbf{2.25}$$

where the additional terms E_q and E_c ($[J]$) ensue form quantisation effect and Coulombic attraction between electrons and holes in a screened environment. The latter phenomena predominantly influence the behaviour of excitons, i.e. quasi-particle systems that bound charge-carriers according to materials intrinsic properties. In particular, exciton binding energy is defined as follows:

$$E_b = \frac{\hbar^2}{2\mu r_B^2} \qquad \textbf{2.26}$$

where $1/\mu = 1/m_{e^-} + 1/m_{h^+}$ is the exciton reduced mass and r_B ($[kg]$) the exciton Bohr radius. This quantity describes the exciton spatial extension until annihilation and is expressed by:

$$r_B = \frac{\hbar^2 \varepsilon^2}{\mu e^2} \qquad \textbf{2.27}$$

where ε is the semiconductor dielectric constant ($[\mathcal{F}\, m^{-1}]$). Band-gap energy, exciton binding energy and Bohr radius describe semiconductor nanostructures on

a fundamental level, as it is generally recognised that confined systems display different quantisation degrees in accordance to such quantities. In particular, considering:

$$E_q = \frac{\hbar^2 \pi^2}{2\mu a^2} \qquad \textbf{2.28}$$

$$E_c = -1.8 \frac{e^2}{\varepsilon^2 a} \qquad \textbf{2.29}$$

weak quantisation occurs when $a \gg r_B$, where E_c dominates, while in the strong quantisation regime $a < r_B$ and E_q term is predominant.

The fundamental outcomes of quantum size effect lead to unprecedented development in both bottom-up and top down materials engineering and, not surprisingly, the field of catalysis has enormously benefited from improved manipulation opportunities in terms of hierarchical nano-structuring and surface design[39].

2.2.2 Hybrid Inorganic Colloidal Architectures

The surge of colloidal nanoscience has been nourished by the broad application opportunities that this class of mesoscopic materials has reached in the last decades[40]. Along with the flexibility to tune intrinsic properties by size, shape and composition manipulation at the atomic scale, wet chemical methods enabled further advances in structure complexity with the realisation of heterostructures architectures. As opposed to homo-structures, which are constituted by a single material, hybrid nanostructures present sections of dissimilar material, exhibiting synergistic features and delivering more than one function simultaneously. This opportunity perfectly fits the multiple requirements of catalysis, those efficiency strongly depends on both surface and interface quality of the different active components. On one hand, catalytic activity is intimately related to size, hence confined systems are desirable because of increase surface to volume ration, while, on the other hand, light-triggered phenomena are greatly favoured in spatially

distinct, yet neighbouring reactions site. To this extent, the family of elongated hybrid nanostructures composed of metal-chalcogenide materials greatly contributed to the field of photo-catalysis and artificial photosynthesis[41]. Additionally, it is worth noting that semiconductor-metal hybrids can also be used as asymmetric anchoring sites for self-assembled systems or to improve macro-electrodes/nanoparticles electrical connection.

Considering CdSe as a prototypical system, size-controlled quantum confinement effects allowed property tuning such as E_g ranging from 2.5 to 4 eV and depression of melting temperature form 1600℃ to 400℃, while heterojunctions with CdS determined different type of charge-carriers' confinements[42]. In particular, it is possible to generally reconduct heterostructures to three different classes (parentheses explicit the case of CdSe-CdS systems):

- type I heterostructures, where photo-excited carriers are confined in the lower E_g materials (CdSe)
- type II heterostructures, separating e^- in one material (CdS) and h^+ in the other (CdSe)
- quasi-type II configurations, where h^+ are localised (in CdSe) and e^- wavefunction is spread over the entire structure (CdS and CdSe).

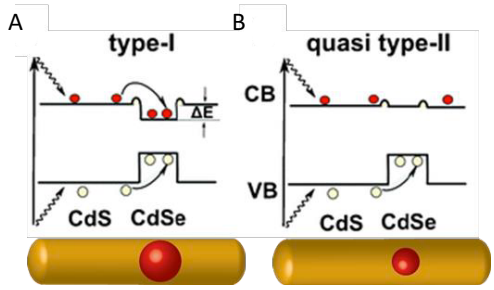

Figure 2.11. **Schematic illustration showing type-I and quasi type-II semiconductor core-shell heterostructures and the effect of core size and the electronic band structure.**

Under an experimental point of view, the possibility to achieve such system complexity was exceptionally endowed by colloidal chemistry routes. Following the landmark breakthrough from Murray, Norris and Bawendi[43], high-quality inorganic nanocrystals are synthesised at high temperature through pyrolysis of precursors in appropriate surfactants and coordinating solvents. The so called "hot-

injection" method allows to obtain crystallites with consistent crystal structure, surface derivatisation and a high degree of mono-dispersity. Notably, nanostructure stabilisation occurs by embedding nanocrystals in a passivating medium, i.e. a monolayer of organic molecules. These surfactants constitute integral part of the colloidal system yet having a marked difference with respect to ligand's function in organo-metallic complexes. In the latter case, ligand identity is highly coupled to the electronic structure of coordination compounds, whereas surface ligands in nanostructures act as passivating agents eliminating energy levels inside the E_g, negligibly influencing the electronic structure of the cores. This unfolds important advantages provided by colloidal systems, namely the possibility to exchange ligands to access a wide variety of solvents or tune the affinity to different adsorbents, without appreciably changing the redox potential and absorption spectra of the particles[44]. Moreover, scaling colloids from millimetre size down to the nanoparticle's regime, active surface sites to volume ratio increases by a factor of 10^6, potentially offering a number of binding sites that largely outcompetes the one of homogeneous catalysts (typically having one/two binding site per unit).

Recent development in ligand chemistry has remarkably contributed the construction of Pt-tipped CdSe@CdS core-shell nanostructures, that are the chief materials used throughout the present doctoral project. Such material architecture closely targets the multitude requirements imposed by efficient solar-to-chemical energy conversion strategies and consequently reflects one the most accurate inorganic artificial mimic of natural photosynthetic systems[45]. More specifically, CdSe@CdS-Pt is a multi-component heterostructure designed to surpass stochastic arrangement while achieving both controlled reaction site distance and degree of charge separation. Following the aforementioned fundamental photosynthetic mechanisms, structure-function relationship can be summarized as follows:

- light-absorption is realized by CdS elongated shell;
- charge separation is promoted through a three component quasi-type II heterostructure, where CdSe and Pt quantum dots, physically and energetically separated by CdS nanorods, selectively collect photogenerated h^+ and e^-, respectively;

- fuel-forming reactions are finally developed using Pt as co-catalyst (reduction half-reaction) and through interfacial electron-transfer in proximity of CdSe QDs (oxidation half-reaction).

The unique properties of CdSe@CdS-Pt leverage on the advantage of cost-effective and versatile productions of solution-processed organic materials and superior optoelectronic properties of inorganic semiconductors, those synthetic development span over the last two decades.

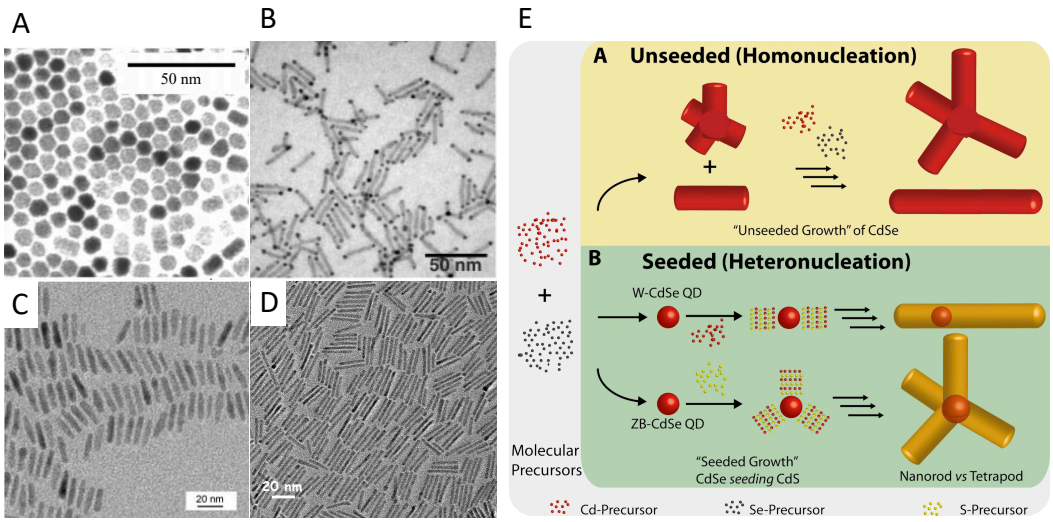

Figure 2.12. **Development of seeded-rod hybrid metal-semiconductor nanostructure.** TEM pictures of A) CdSe nanorods[37], B) Au-tipped nanorods[38], C) CdSe@CdS seeded nanorods[40] and D) same structure used throughout the present work. E) Schematic representation of seeded synthesis of CdSe@CdS nanorods and nanotetrapods.

Firstly, control over size and shape of metal-chalcogenides was demonstrated through careful manipulation of nucleation and growth kinetics by Alivisatos group[46]. In their pioneering work, Peng et al. obtained monodispersed anisotropic structure ranging from 10 to 100 nm by alkyl phosphonic acid-mediated growth of the $< 001 >$ axis of wurtzite CdSe (Figure 2.12A). The surfactants showed stronger coordination to Cd atoms with respect to TOPO (trioctylphosphine oxide) and allowed slower growth of facets but the one oriented along the c-axis. Difference in surface energetics was also cleverly exploited to covalently bind metal nanoparticles to nanorod tips[47,48]. As shown in Figure 2.12B, Mokari et al. contacted nanorods with single and bi-metal nanoparticles, controlling quantum size through initial precursor concentration. The addition of metal tips quenches

nanorods emission via non-radiative pathways, as brilliantly demonstrated by the authors through Stern-Volmer analysis, i.e. by monitoring nanorods fluorescence emission decrease as a function of anchored metal size. Fluorescent properties are known to be improved through core-shell hetero-structuring, which motivated Talapin et al. to develop a seeded-growth approach for metal-chalcogenide materials[49]. The novel synthetic procedure allowed separation of growth and nucleation processes, yielding nanorod and nano-tetrapod structures when wurtzite or zinc-blend CdSe were used as seed reagents (Figure 2.12C). CdSe@CdS structures presents therefore a mixed dimensionality, where CdS arms act as antenna units funnelling excited carriers in CdSe cores, where recombination occurs. Remarkably, fluorescence quantum yields as high as 80% can be obtained, while giant extinction coefficients ranging from $\sim 10^7$ to $10^8\ M^{-1}cm^{-1}$ at 350 nm are commonly reported for such structures.

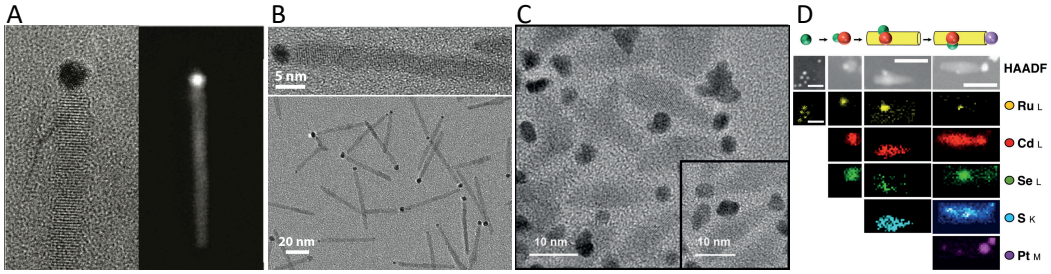

Figure 2.13. **Pt-tipped CdSe@CdS.**
TEM pictures of A) a single particle reported by Amirav et al.[41] and B) a batch used in the present work. C) Ru@Ru_xO_y-CdSe@CdS-Pt dual-metal dual-semiconductor hybrid heterostructure[43].

A further synthetic effort by Amirav and Alivisatos combined the precise spatial arrangement provided by seeded-nanorods with the catalytic properties of Pt-nanoparticles[50]. The so designed hybrid heterostructure can be regarded as a closed-circuit photoelectrochemical cell, having two electrodes separated by a tuneable distance in the nanometric range, as seen in Figure 2.13A and 2.13B. Additional synthetic control of the CdSe seed size allows improved charge separation, yielding up to 100% photon to hydrogen quantum efficiency when using isopropanol as reducing reagent in strong basic conditions[51]. Such harsh reaction conditions were necessary for efficient hydrogen production turnover because of the sluggish

kinetics characterising the oxygen-evolution half-reaction. In order to overcome this limitation, Amirav et al. finally realised a dual-metal dual semiconductor systems (Figure 2.13C), where both redox reaction sites were endowed with co-catalyst to align reaction kinetics[52]. Realisation of overall water splitting depends indeed on the multi-electronic water reduction (2 e^- required) and oxidation (4 h^+ needed), that were expected to be favoured by Pt and Ru@Ru_xO_y nanoparticles, respectively. Although no report of overall water splitting was provided, the modular, sequential and multistep assembly of colloidal building blocks exceptionally paralleled molecular chemistry protocols.

2.2.3 Semiconductor Photochemistry and Efficiency Metrics

The superior optoelectronic properties, together with facile and cheap synthetic methods, make semiconductor nanostructures ideal candidates for photochemical devices. As discussed in previous chapters, high luminescence quantum yields favour efficient solar-to-chemical energy conversion, whereas abundant surface sites endow these materials with equally high reaction turnover and kinetics potential. Nonetheless, combining both light-harvesting and catalytic units, homogeneous semiconductor systems display a rich photophysics and photochemical behaviour[53], as illustrated in Figure 2.14.

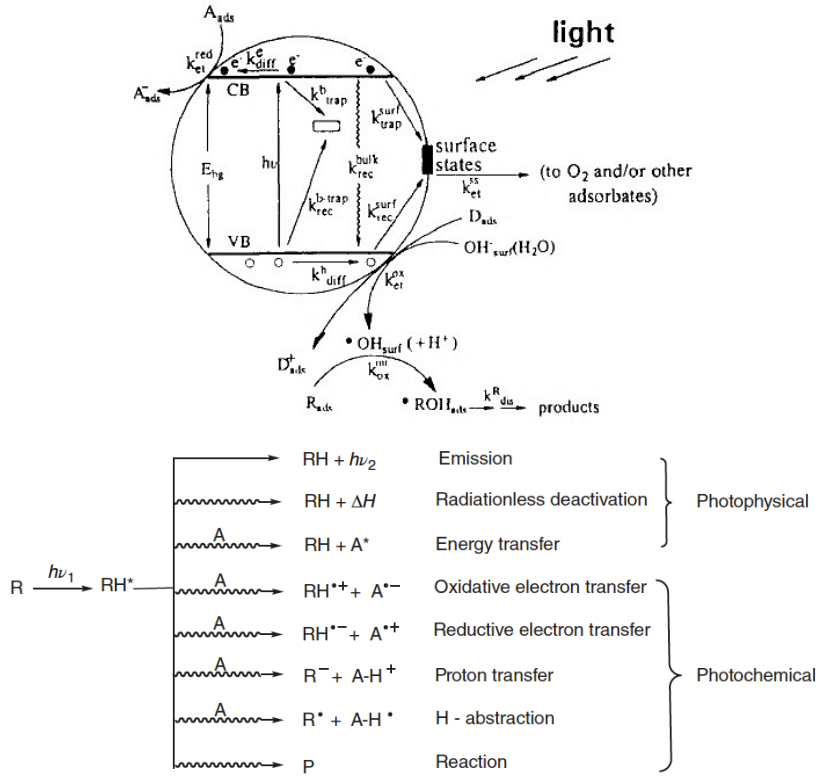

Figure 2.14. **Schematic illustration of photochemical and photophysical processes for semiconductor particles[44,45].**

In particular, radiative decay can occur via bulk or surface trap recombination, while excitons can be dissociatively trapped into reactive or unreactive surface sites. Interfacial electron transfer is then classified according to the disproportionation mechanism, i.e. different acceptor/donor moieties can lead to either oxidative or reductive quenching. Remarkably, semiconductor systems undergo two *concerted* electron transfer steps with two reactants, simultaneously harvesting both photo-generated charge carriers. This process is in stark contrast with the one characterising molecular photo-sensitisers, that usually act as single-electron reductant/oxidant, requiring the use of sacrificial moieties to regenerate the ground state electronic configuration. Finally, product formation ensues successful competition against back-electron transfer and is mathematically expressed by the following formula:

$$\Phi_P = \eta_r \eta_{IFET} \eta_p \qquad \textbf{2.30}$$

where η_i account for reactive e^-/h^+ pair formation, interfacial electron-transfer and product formation. Moreover, Kisch importantly differentiated between photochemical processes that produce two separate products from intermediate radicals (Type-A reactions) with single product formation following radical-radical coupling (Type-B reactions)[54]. Recently, König extended such classification with B' and B" mechanisms to include synthetic reactions involving addition/elimination of multiple functional groups[55].

The atypical photochemical behaviour of semiconductor system with respect to molecular counterparts has sometimes led to inappropriate efficiency and outcomes estimation[56–58]. It is therefore worth noting that, as photochemical rates depend on the amount of photon absorbed, reaction rates normalised to weight are not meaningful unless photoreactor engineering is the primary concern. Since photochemical rate constant depend on quantum yield, incident light intensity, light-path and extinction coefficient, optimal concentration should be determined for each photochemical unit, as shown in Figure 2.15. For the case of hydrogen generation, common reaction metrics are defined as follows:

$$QE_{PTH} = \frac{\text{number of } H_2 \text{ molecules formed}}{\text{number of photons absorbed}} \cdot 100\% \qquad \textbf{2.31}$$

$$STH = \frac{r_{H_2} \cdot \mu_{H_2O/H_2-O_2}}{P_{AM1.5G} \cdot A_{\emptyset}} \cdot 100\% \qquad \textbf{2.32}$$

where QE_{PTH} expresses the photon-to-hydrogen quantum efficiency , while STH the solar-to-hydrogen conversion efficiency. In the latter formula, r_{H_2} refers to the H_2 formation rate ($[mol\ s^{-1}]$), μ_{H_2O/H_2-O_2} to the chemical potential ($[J\ mol^{-1}]$), extracted from water ($2.37\ kJ\ mol^{-1}$), $P_{AM1.5G}$ ($[W\ m^{-2}]$), to the total incoming power for the reference AM1.5G spectrum and $A_{\emptyset}$ the irradiation spot-size area($[m^2]$)[57]. When alternative redox reactions are performed instead of water splitting, chemical conversion efficiency is estimated according to the μ deposited into the reaction products. Importantly, positive μ entail endothermic reactions, termed photosynthetic process, while negative μ represent exothermic reactions that do *not* harvest radiation chemical potential but accelerate reaction kinetics, thus are termed photocatalytic reactions[31,59].

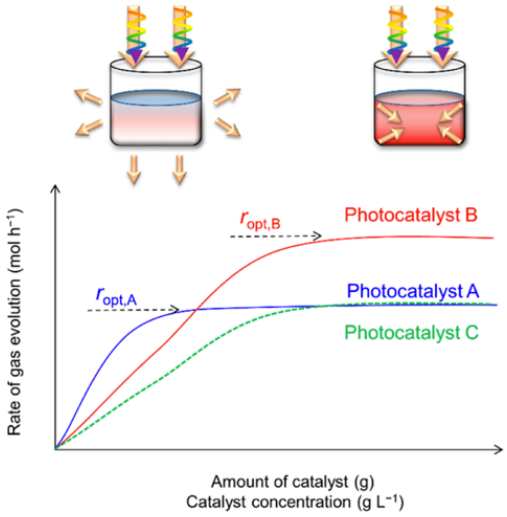

Figure 2.15. **Reaction rate as a function of catalyst concentration for different semiconductor systems[48].**

References

1. Pearson, P. N. & Palmer, M. R. Atmospheric carbon dioxide concentrations over the past 60 million years. *Nature* **406**, 695–699 (2000).
2. Sapart, C. J. *et al.* Natural and anthropogenic variations in methane sources during the past two millennia. *Nature* **490**, 85–88 (2012).
3. Cook, J. *et al.* Consensus on consensus: a synthesis of consensus estimates on human-caused global warming. *Environ. Res. Lett.* **11**, 1–7 (2016).
4. *World Energy Outlook 2018*. *International Energy Agency Publications* (2018).
5. Lewis, N. S. & Nocera, D. G. Powering the planet: Chemical challenges in solar energy utilization. *Proc. Natl. Acad. Sci.* **103**, 15729–15735 (2006).
6. Tachibana, Y., Vayssieres, L. & Durrant, J. R. Artificial photosynthesis for solar water-splitting. *Nat. Photonics* **6**, 511–518 (2012).
7. Kornienko, N., Zhang, J. Z., Sakimoto, K. K., Yang, P. & Reisner, E. Interfacing nature's catalytic machinery with synthetic materials for semi-artificial photosynthesis. *Nat. Nanotechnol.* **13**, 890–899 (2018).
8. United States Department of Energy. *DOE Technical Targets for Hydrogen Production from Photoelectrochemical Water Splitting*. (2011).
9. Japanese Ministerial Council on Renewable Energy - Hydrogen and Related Issues. *Basic Hydrogen Strategy*. (2017).
10. Jang, J.-W. *et al.* Toward practical solar hydrogen production-an artificial photosynthetic leaf-to-farm challenge. *Chem. Soc. Rev.* **48**, 1908–1971 (2019).
11. Goto, Y. *et al.* A Particulate Photocatalyst Water-Splitting Panel for Large-Scale Solar Hydrogen Generation. *Joule* **2**, 509–520 (2018).
12. Hisatomi, T. & Domen, K. Reaction systems for solar hydrogen production via water splitting with particulate semiconductor photocatalysts. *Nat. Catal.* **2**, 387–399 (2019).
13. Fabian, D. M. *et al.* Particle suspension reactors and materials for solar-driven water splitting. *Energy Environ. Sci.* **8**, 2825–2850 (2015).
14. Ciamician, G. The photochemistry of the future. *Science.* **36**, 385–394 (1912).
15. Verhoeven, J. W. Glossary of Terms used in Photochemistry. *Pure Appled Chem.* **68**, 2223–2286 (1996).
16. Kisch, H. *Semiconductor Photocatalysis*. (2014).
17. Barber, J. Biological solar energy. *Philos. Trans. Math. Phys. Eng. Sci.* **365**, 1007–1023 (2007).
18. Böer, K. W. The solar spectrum at typical clear weather days. *Sol. Energy* **19**, 525–538 (1977).
19. Blankenship, R. E. *et al.* Comparing Photosynthetic and Photovoltaic Efficiencies and Recognizing the Potential for Improvement. *Science.* **332**, 805–809 (2011).
20. Bolton, J. R. & Hall, D. O. Conversion and Storage. *Annu. Rev. Energy* **4**, 353–401 (1979).
21. Ross, R. T. & Hsiao, T.-L. Limits on the yield of photochemical solar energy conversion. *J. Appl. Phys.* **48**, 4783–4785 (1977).

22. Bolton, J. R. Solar Fuels : The production of energy-rich compounds by the photochemical conversion and storage of solar energy. *Science.* **202**, 705–711 (1978).
23. Bolton, J. R., Haught, A. F. & Ross, R. T. Photochemical Energy Storage: An Analysis of Limits. in *Photochemical Conversion and Storage of Solar Energy* 297–346 (1981).
24. Bolton, J. R., Strickler, S. J. & Connolly, J. S. Limiting and realizable efficiencies of solar photolysis of water. *Nature* **316**, 495–500 (1985).
25. Archer, M. D. & Bolton, J. R. Requirements for Ideal Performance of Photochemical and Photovoltaic Solar Energy Converters. *J. Phys. Chem.* **94**, 8028–8036 (1990).
26. Shockley, W. & Queisser, H. J. Detailed Balance Limit of Efficiency of p-n Junction Solar Cells. *J. Appl. Phys.* **32**, 510–519 (1961).
27. Baierlein, R. The elusive chemical potential. *Am. J. Phys.* **69**, 423–434 (2001).
28. McConnell, I., Li, G. & Brudvig, G. W. Energy Conversion in Natural and Artificial Photosynthesis. *Chem. Biol.* **17**, 434–447 (2010).
29. Fujishima, A. & Honda, K. Electrochemical Photolysis of Water at a Semiconductor Electrode. *Nature* **238**, 37–38 (1972).
30. Kirch, M., Lehn, J.-M. & Sauvage, J.-P. Hydrogen Generation by Visible Light Irradiation of Aqueous Solutions of Metal Complexes. An approach to the photochemical conversion and storage of solar energy. *Helv. Chim. Acta* **62**, 1345–1384 (1979).
31. Bard, A. J. Photoelectrochemistry and heterogeneous photo-catalysis at semiconductors. *J. Photochem.* **10**, 59–75 (1979).
32. Grätzel, M. Artificial Photosynthesis: Water Cleavage into Hydrogen and Oxygen by Visible Light. *Acc. Chem. Res.* **14**, 376–384 (1981).
33. Đokicá, M. & Soo, H. Sen. Artificial photosynthesis by light absorption, charge separation, and multielectron catalysis. *Chem. Commun.* **54**, 6554–6572 (2018).
34. Serpone, N. *et al.* Why do Hydrogen and Oxygen Yields from Semiconductor-Based Photocatalyzed Water Splitting Remain Disappointingly Low? Intrinsic and Extrinsic Factors Impacting Surface Redox Reactions. *ACS Energy Lett.* **1**, 931–948 (2016).
35. Madelung, O. II-VI compounds. in *Semiconductors: Data Handbook* 173–244 (2004).
36. Steigerwald, M., Bawendi, M. G., Steigerwald, M. L. & Brus, L. E. The Quantum Mechanics of Larger Semiconductor Clusters. *Annu. Rev. Phys. Chem.* **41**, 477–96 (2003).
37. Yang, W. *et al.* Electron Accumulation Induces Efficiency Bottleneck for Hydrogen Production in Carbon Nitride Photocatalysts. *J. Am. Chem. Soc.* **141**, 11219–11229 (2019).
38. Edvinsson, T. Optical quantum confinement and photocatalytic properties in two-, one-and zero-dimensional nanostructures. *R. Soc. Open Sci.* **5**, 180387–180403 (2018).
39. Li, X., Yu, J. & Jaroniec, M. Hierarchical photocatalysts. *Chem. Soc. Rev.* **45**, 2603–2636 (2016).
40. Kovalenko, M. V. *et al.* Prospects of Nanoscience with Nanocrystals. *ACS*

Nano **9**, 1012–1057 (2015).
41. Wu, K. & Lian, T. Quantum confined colloidal nanorod heterostructures for solar-to-fuel conversion. *Chem. Soc. Rev.* **45**, 3759–4034 (2016).
42. Alivisatos, A. P. Perspectives on the Physical Chemistry of Semiconductor Nanocrystals. *J. Phys. Chem.* **100**, 13226–13239 (1996).
43. Murray, C. B., Norris, D. J. & Bawendi, M. G. Synthesis and Characterization of Nearly Monodisperse CdE (E = S, Se, Te) Semiconductor Nanocrystallites. *J. Am. Chem. Soc* **115**, 8706–8715 (1993).
44. Weiss, E. A. Designing the surfaces of semiconductor quantum dots for colloidal photocatalysis. *ACS Energy Lett.* **2**, 1005–1013 (2017).
45. Amirav, L. & Alivisatos, A. P. Photocatalytic Hydrogen Production with Tunable Nanorod Heterostructures. *J. Phys. Chem. Lett* **1**, 1051–1054 (2010).
46. Peng, X. *et al.* Shape control of CdSe nanocrystals. *Nature* **404**, 3408–3413 (2000).
47. Mokari, T., Rothenberg, E., Popov, I., Costi, R. & Banin, U. Selective Growth of Metal Tips onto Semiconductor Quantum Rods and Tetrapods. *Science.* **304**, (2004).
48. Habas, S. E., Yang, P. & Mokari, T. Selective Growth of Metal and Binary Metal Tips on CdS Nanorods. *J. Am. Chem. Soc.* **130**, 3294–3295 (2008).
49. Talapin, D. V. *et al.* Seeded Growth of Highly Luminescent CdSe/CdS Nanoheterostructures with Rod and Tetrapod Morphologies. *Nano Lett.* **7**, 2951–2959 (2007).
50. Amirav, L. & Alivisatos, A. P. Luminescence Studies of Individual Quantum Dot Photocatalysts. *J. Am. Chem. Soc.* **135**, 13049–13053 (2013).
51. Kalisman, P., Nakibli, Y. & Amirav, L. Perfect photon-to-hydrogen conversion efficiency. *Nano Lett.* **16**, 1776–1781 (2016).
52. Amirav, L., Oba, F., Aloni, S. & Alivisatos, A. P. Modular Synthesis of a Dual Metal-Dual Semiconductor Nano-Heterostructure. *Angew. Chemie Int. Ed.* **54**, 7007–7011 (2015).
53. Serpone, N. *et al.* Standardization protocol of process efficiencies and activation parameters in heterogeneous photocatalysis: Relative photonic efficiencies ζr. *J. Photochem. Photobiol. A Chem.* **94**, 191–203 (1996).
54. Kisch, H. Semiconductor photocatalysis for chemoselective radical coupling reactions. *Acc. Chem. Res.* **50**, 1002–1010 (2017).
55. Ghosh, I. *et al.* Organic semiconductor photocatalyst can bifunctionalize arenes and heteroarenes. *Science.* **365**, 360–366 (2019).
56. Kisch, H. On the Problem of Comparing Rates or Apparent Quantum Yields in Heterogeneous Photocatalysis. *Angew. Chemie Int. Ed.* **49**, 9588–9589 (2010).
57. Qureshi, M. & Takanabe, K. Insights on Measuring and Reporting Heterogeneous Photocatalysis: Efficiency Definitions and Setup Examples. *Chem. Mater.* **29**, 158–167 (2017).
58. Kunz, L. Y. *et al.* Artificial inflation of apparent photocatalytic activity induced by catalyst-mass-normalization and a method to fairly compare heterojunction systems. *Energy Environ. Sci.* **12**, 1657–1667 (2019).
59. Osterloh, F. E. Photocatalysis versus Photosynthesis: A Sensitivity Analysis of Devices for Solar Energy Conversion and Chemical

Transformations. *ACS Energy Lett.* **2**, 445–453 (2017).
60. Coontz, R. *et al.* Toward a Hydrogen Economy. *Science.* **305**, 957–976 (2004).
61. Tang, J., Durrant, J. R. & Klug, D. R. Mechanism of photocatalytic water splitting in TiO_2. Reaction of water with photoholes, importance of charge carrier dynamics, and evidence for four-hole chemistry. *J. Am. Chem. Soc.* **130**, 13885–13891 (2008).
62. Wolff, C. *et al.* All-in-one visible-light-driven water splitting by combining nanoparticulate and molecular co-catalysts on CdS nanorods. *Nat. Energy* **3**, 862–869 (2018).
63. You, B., Han, G. & Sun, Y. Electrocatalytic and photocatalytic hydrogen evolution integrated with organic oxidation. *Chem. Commun.* **54**, 5943–5955 (2018).
64. Nakibli, Y. & Amirav, L. Selective Growth of Ni Tips on Nanorod Photocatalysts. *Chem. Mater.* **28**, 4524–4527 (2016).
65. Norris, D. J., Sacra, A., Murray, C. B. & Bawendi, M. G. Measurement of the size dependent hole spectrum in CdSe quantum dots. *Phys. Rev. Lett.* **72**, 2612–2615 (1994).
66. Ekimov, A. I. *et al.* Absorption and intensity-dependent photoluminescence measurements on CdSe quantum dots: assignment of the first electronic transitions. *J. Opt. Soc. Am. B* **10**, 100–107 (1993).
67. Hoang, T. B. *et al.* Temperature dependent photoluminescence of single CdS nanowires. *Appl. Phys. Lett.* **89**, 1231231–1231233 (2006).
68. Puthussery, J., Lan, A., Kosel, T. H. & Kuno, M. Band-Filling of Solution-Synthesized CdS Nanowires. *ACS Nano* **2**, 357–367 (2008).
69. Shabaev, A. & Efros, A. L. 1D Exciton Spectroscopy of Semiconductor Nanorods. *Nano Lett.* **4**, 1821–1825 (2004).
70. Sitt, A., Sala, F. Della, Menagen, G. & Banin, U. Multiexciton Engineering in Seeded Core/Shell Nanorods: Transfer from Type-I to Quasi-type-II Regimes. *Nano Lett.* **9**, 3470–3476 (2009).
71. Rainò, G. *et al.* Probing the Wave Function Delocalization in CdSe/CdS Dot-in-Rod Nanocrystals by Time- and Temperature-Resolved Spectroscopy. *ACS Nano* **5**, 4031–4036 (2011).
72. Smith, E. R., Luther, J. M. & Johnson, J. C. Ultrafast Electronic Delocalization in CdSe/CdS Quantum Rod Heterostructures. *Nano Lett.* **11**, 4923–4931 (2011).
73. Wu, K. *et al.* Universal Length Dependence of Rod-to-Seed Exciton Localization Efficiency in Type I and Quasi-Type II CdSe@CdS Nanorods. *ACS Nano* **9**, 4591–4599 (2015).
74. Christodoulou, S. *et al.* Band structure engineering via piezoelectric fields in strained anisotropic CdSe/CdS nanocrystals. *Nat. Commun.* **6**, 7905–7912 (2015).
75. Lakowicz, J. R. *Principles of Fluorescence Spectroscopy*. (2006).
76. Tarafder, K., Surendranath, Y., Olshansky, J. H., Alivisatos, A. P. & Wang, L.-W. Hole Transfer Dynamics from a CdSe/CdS Quantum Rod to a Tethered Ferrocene Derivative. *J. Am. Chem. Soc.* **136**, 5121–5131 (2014).
77. Mokari, T., Sztrum, C. G., Salant, A., Rabani, E. & Banin, U. Formation of asymmetric one-sided metal-tipped semiconductor nanocrystal dots and

rods. *Nat. Mater.* **4**, 855–863 (2005).
78. Wu, K. *et al.* Hole Removal Rate Limits Photodriven H $_2$ Generation Efficiency in CdS-Pt and CdSe/CdS-Pt Semiconductor Nanorod–Metal Tip Heterostructures. *J. Am. Chem. Soc.* **136**, 7708–7716 (2014).
79. Lupo, M. G. *et al.* Ultrafast Electron−Hole Dynamics in Core/Shell CdSe/CdS Dot/Rod Nanocrystals. *Nano Lett.* **8**, 4582–4587 (2008).
80. Utterback, J. K. *et al.* Observation of trapped-hole diffusion on the surfaces of CdS nanorods. *Nat. Chem.* **8**, 1061–1066 (2016).
81. Grennell, A. N., Utterback, J. K., Pearce, O. M., Wilker, M. B. & Dukovic, G. Relationships between Exciton Dissociation and Slow Recombination within ZnSe/CdS and CdSe/CdS Dot-in-Rod Heterostructures. *Nano Lett.* **17**, 3764–3774 (2017).
82. Utterback, J. K., Hamby, H., Pearce, O. M., Eaves, J. D. & Dukovic, G. Trapped-Hole Diffusion in Photoexcited CdSe Nanorods. *J. Phys. Chem. C* **122**, 16974–16982 (2018).
83. Pearce, O. M., Duncan, J. S., Damrauer, N. H. & Dukovic, G. Ultrafast Hole Transfer from CdS Quantum Dots to a Water Oxidation Catalyst. *J. Phys. Chem. C* **122**, 17559–17565 (2018).
84. Tran, K. & Ulissi, Z. W. Active learning across intermetallics to guide discovery of electrocatalysts for CO_2 reduction and H_2 evolution. *Nat. Catal.* **1**, 696–703 (2018).
85. Hopkinson, M. N., Gómez-Suárez, A., Teders, M., Sahoo, B. & Glorius, F. Accelerated discovery in photocatalysis using a mechanism-based screening method. *Angew. Chemie Int. Ed.* **128**, 4434–4439 (2016).
86. Würth, C., Grabolle, M., Pauli, J., Spieles, M. & Resch-Genger, U. Relative and absolute determination of fluorescence quantum yields of transparent samples. *Nat. Protoc.* **8**, 1535–1550 (2013).
87. Morris-Cohen, A. J., Vasilenko, V., Amin, V. A., Reuter, M. G. & Weiss, E. A. Model for Adsorption of Ligands to Colloidal Quantum Dots with Concentration-Dependent Surface Structure. *ACS Nano* **6**, 557–565 (2012).
88. Uematsu, T., Shimomura, E., Torimoto, T. & Kuwabata, S. Evaluation of Surface Ligands on Semiconductor Nanoparticle Surfaces Using Electron Transfer to Redox Species. *J. Phys. Chem. C* **120**, 16012–12023 (2016).
89. Tachiya, M. Application of a generating function to reaction kinetics in micelles. Kinetics of quenching of luminescent probes in micelles. *Chem. Phys. Lett.* **33**, 289–292 (1975).
90. Ross, R. T. & Calvin, M. Thermodynamics of Light Emission and Free-Energy Storage in Photosynthesis. *Biophys. J.* **7**, 595–614 (1967).
91. Wang, Z. J., Garth, K., Ghasimi, S., Landfester, K. & Zhang, K. A. I. Conjugated Microporous Poly(Benzochalcogenadiazole)s for Photocatalytic Oxidative Coupling of Amines under Visible Light. *ChemSusChem* **8**, 3459–3464 (2015).
92. Xiao, X., Jiang, J. & Zhang, L. Selective oxidation of benzyl alcohol into benzaldehyde over semiconductors under visible light: The case of $Bi_{12}O_{17}Cl_2$ nanobelts. *Appl. Catal. B Environ.* **142**–**143**, 487–493 (2013).
93. Su, Y., Straathof, N. J. W., Hessel, V. & Noël, T. Photochemical Transformations Accelerated in Continuous-Flow Reactors: Basic Concepts and Applications. *Chem. - A Eur. J.* **20**, 10562–10589 (2014).

94. Chang, C.-C., Chen, L.-C. C. & Liu, S.-J. L. Investigation of electro-oxidation of methanol and benzyl alcohol at boron-doped diamond electrode: evidence for the mechanism for fouling film formation. *J. Phys. Chem. B* **110**, 19426–19432 (2006).
95. Serpone, N. & Emeline, A. V. Suggested terms and definitions in photocatalysis and radiocatalysis. *Int. J. Photoenergy* **4**, 91–131 (2007).
96. Kamat, P. V., Christians, J. A. & Radich, J. G. Quantum dot solar cells: hole transfer as a limiting factor in boosting the photoconversion efficiency. *Langmuir* **30**, 5716–5725 (2014).
97. DiMeglio, J. L. & Bartlett, B. M. Interplay of corrosion and photocatalysis during nonaqueous benzylamine oxidation on cadmium sulfide. *Chem. Mater.* **29**, 7579–7586 (2017).
98. Kisch, H. & Bahnemann, D. Best Practice in Photocatalysis: Comparing Rates or Apparent Quantum Yields? *J. Phys. Chem. Lett.* **6**, 1907–1910 (2015).
99. Gomollón-Bel, F. Ten Chemical Innovations That Will Change Our World. *Chem. Int.* **41**, 1–17 (2019).
100. Baker, C. O., Huang, X., Nelson, W. & Kaner, R. B. Polyaniline nanofibers: broadening applications for conducting polymers. *Chem. Soc. Rev.* **46**, 1510–1525 (2017).
101. Jäckle, S. *et al.* Potential of PEDOT:PSS as a hole selective front contact for silicon heterojunction solar cells. *Sci. Rep.* **7**, 2170–2177 (2017).
102. Chen, K., Deng, X., Dodekatos, G. & Tüysüz, H. Photocatalytic Polymerization of 3,4-Ethylenedioxythiophene over Cesium Lead Iodide Perovskite Quantum Dots. *J. Am. Chem. Soc.* (2017).
103. Kirkwood, N. *et al.* Finding and Fixing Traps in II–VI and III–V Colloidal Quantum Dots: The Importance of Z-Type Ligand Passivation. *J. Am. Chem. Soc.* **140**, 15712–15723 (2018).
104. Trent, J. S., Scheinbeim, J. I. & Couchman, P. R. Ruthenium tetraoxide staining of polymers for electron microscopy. *Macromolecules* **16**, 589–598 (1983).
105. Kirchmeyer, S. & Reuter, K. Scientific importance, properties and growing applications of poly(3,4-ethylenedioxythiophene). *J. Mater. Chem.* **15**, 2077–2088 (2005).
106. Kuehnel, M. F. & Reisner, E. Solar Hydrogen Generation from Lignocellulose. *Angew. Chemie Int. Ed.* **57**, 3290–3296 (2018).
107. Wakerley, D. W. *et al.* Solar-driven reforming of lignocellulose to H_2 with a CdS/CdOx photocatalyst. *Nat. Energy* **2**, 17021–17030 (2017).
108. Kasap, H., Achilleos, D. S., Huang, A. & Reisner, E. Photoreforming of lignocellulose into H_2 using nano-engineered carbon nitride under benign conditions. *J. Am. Chem. Soc.* 28 (2018).
109. Uekert, T., Kuehnel, M. F., Wakerley, D. W. & Reisner, E. Plastic waste as a feedstock for solar-driven H_2 generation. *Energy Environ. Sci.* **11**, 2853–2857 (2018).
110. Uekert, T., Kasap, H. & Reisner, E. Photoreforming of Nonrecyclable Plastic Waste over a Carbon Nitride/Nickel Phosphide Catalyst. *J. Am. Chem. Soc.* **141**, 15201−15210 (2019).
111. Simon, T. *et al.* Redox shuttle mechanism enhances photocatalytic H_2

generation on Ni-decorated CdS nanorods. *Nat. Mater.* **13**, 1013–1018 (2014).
112. Ishibashi, K., Fujishima, A., Watanabe, T. & Hashimoto, K. Detection of active oxidative species in TiO_2 photocatalysis using the fluorescence technique. *Electrochem. commun.* **2**, 207–210 (2000).
113. Han, X. *et al.* Structural insight into catalytic mechanism of PET hydrolase. *Nat. Commun.* **8**, 2106–2011 (2017).
114. Habisreutinger, S. N., Schmidt-Mende, L. & Stolarczyk, J. K. Photocatalytic Reduction of CO_2 on TiO_2 and Other Semiconductors. *Angew. Chemie Int. Ed.* **52**, 7372–7408 (2013).
115. Stolarczyk, J. K., Bhattacharyya, S., Polavarapu, L. & Feldmann, J. Challenges and Prospects in Solar Water Splitting and CO_2 Reduction with Inorganic and Hybrid Nanostructures. *ACS Catal.* (2018).
116. Tollefson, J. Can the World Slow Global Warming? *Nature* **572**, 325–326 (2019).
117. Manzi, A. *et al.* Light-Induced Cation Exchange for Copper Sulfide Based CO_2 Reduction. *J. Am. Chem. Soc.* **137**, 14007–14010 (2015).
118. Wang, D. *et al.* How and Why Nanoparticle's Curvature Regulates the Apparent pK_a of the Coating Ligands. *J. Am. Chem. Soc.* **133**, 2192–2197 (2011).
119. Woehrle, G. H., Brown, L. O. & Hutchison, J. E. Thiol-Functionalized, 1.5-nm Gold Nanoparticles through Ligand Exchange Reactions: Scope and Mechanism of Ligand Exchange. *J. Am. Chem. Soc.* **127**, 2172–2183 (2005).
120. Fogg, P. G. T. *Carbon Dioxide in Non-Aqueous Solvents at Pressure less than 200 kPa*. (1992).
121. Rosen, B. A. *et al.* Ionic Liquid-Mediated Selective Conversion of CO_2 to CO at Low Overpotentials. *Science.* **334**, 643–644 (2011).
122. Dong, C. *et al.* Size-dependent activity and selectivity of carbon dioxide photocatalytic reduction over platinum nanoparticles. *Nat. Commun.* **9**, 1252–1262 (2018).
123. Ran, J., Jaroniec, M. & Qiao, S.-Z. Cocatalysts in Semiconductor-based Photocatalytic CO_2 Reduction: Achievements, Challenges, and Opportunities. *Adv. Mater.* **30**, 1704649–1704679 (2018).
124. McQuillin, F. J. *Homogeneous Hydrogenation in Organic Chemistry*. (1976).
125. Prier, C. K., Rankic, D. A. & MacMillan, D. W. C. Visible Light Photoredox Catalysis with Transition Metal Complexes: Applications in Organic Synthesis. *Chem. Rev.* **113**, 5322–5363 (2013).
126. Romero, N. A. & Nicewicz, D. A. Organic Photoredox Catalysis. *Chem. Rev.* **116**, 10075–10166 (2016).
127. Balzani, V., Bergamini, G. & Ceroni, P. Photochemistry and photocatalysis. *Rend. Lincei* (2017).
128. Magagnano, G. *et al.* Photocatalytic ATRA reaction promoted by iodo-Bodipy and sodium ascorbate. *Chem. Commun.* **53**, 1591–1594 (2017).
129. Pal, A., Ghosh, I., Sapra, S. & König, B. Quantum Dots in Visible-Light Photoredox Catalysis: Reductive Dehalogenations and C−H Arylation Reactions Using Aryl Bromides. *Chem. Mater.* **29**, 5225–5231 (2017).

130. Zhang, Z., Edme, K., Lian, S. & Weiss, E. A. Enhancing the Rate of Quantum-Dot-Photocatalyzed Carbon−Carbon Coupling by Tuning the Composition of the Dot's Ligand Shell. *J. Am. Chem. Soc.* **139**, 4246–4249 (2017).
131. Caputo, J. A. *et al.* General and Efficient C−C Bond Forming Photoredox Catalysis with Semiconductor Quantum Dots. *J. Am. Chem. Soc.* **139**, 4250–4253 (2017).
132. Nicewicz, D. A. & MacMillan, D. W. C. Merging photoredox catalysis with organocatalysis: the direct asymmetric alkylation of aldehydes. *Science.* **322**, 77–80 (2008).
133. Lewis, N. S. Developing a scalable artificial photosynthesis technology through nanomaterials by design. *Nat. Nanotechnol.* **11**, (2016).
134. Pinaud, B. A. *et al.* Technical and economic feasibility of centralized facilities for solar hydrogen production via photocatalysis and photoelectrochemistry. *Energy Environ. Sci.* 1983–2002 (2013). doi:10.1039/c3ee40831k
135. O'Regan, B. & Grätzel, M. A low-cost, high-efficiency solar cell based on dye-sensitized colloidal TiO_2 films. *Nature* **353**, 737–740 (1991).
136. Mazzaro, R. *et al.* Uniform Functionalization of High-Quality Graphene with Platinum Nanoparticles for Electrocatalytic Water Reduction. *ChemistryOpen* **4**, 268–273 (2015).
137. Grzelczak, M., Vermant, J., Furst, E. M. & Liz-Marzá, L. M. Directed Self-Assembly of Nanoparticles. *ACS Nano* **4**, 3591–3605 (2010).
138. Cambié, D. & Noël, T. Solar Photochemistry in Flow. *Top. Curr. Chem.* **376**, 45 (2018).
139. Pieber, B., Shalom, M., Antonietti, M., Seeberger, P. H. & Gilmore, K. Heterogeneous Photocatalysis in Serial Micro-Batch Reactors. *Angew. Chemie Int. Ed.* **57**, 9976–9979 (2018).
140. Italia, V. *et al.* Laser-Inscribed Glass Microfluidic Device for Non-Mixing Flow of Miscible Solvents. *Micromachines* **10**, 23–32 (2018).
141. Ashton, P. R. *et al.* A Three-Pole Supramolecular Switch. *J. Am. Chem. Soc.* **121**, 3951–3957 (1999).
142. Niu, W.-J. *et al.* Dumbbell-shaped carbon quantum dots/AuNCs nanohybrid as an efficient ratiometric fluorescent probe for sensing cadmium (II) ions and l-ascorbic acid. *Carbon N. Y.* **96**, 1034–1042 (2016).
143. Ju, E. *et al.* Heterogeneous Assembled Nanocomplexes for Ratiometric Detection of Highly Reactive Oxygen Species in Vitro and in Vivo. *ACS Nano* **6**, 6014–6023 (2019).
144. Kodaimati, M. S. *et al.* Viewpoint: Challenges in Colloidal Photocatalysis and Some Strategies for Addressing Them. *Inorg. Chem.* **57**, 3659–3670 (2018).
145. Carbone, L. *et al.* Synthesis and Micrometer-Scale Assembly of Colloidal CdSe/CdS Nanorods Prepared by a Seeded Growth Approach. *Nano Lett.* **7**, 2942–2950 (2007).

Chapter 3 Photosynthetic H_2 production and Organics Transformations

3.1 Introduction

Photosynthetic generation of hydrogen (H_2) and oxygen (O_2) from water is considered the "holy grail" reaction of photochemical research. This process generates a fuel with a gravimetric energy density 3 times larger compared to gasoline ($120 \div 142\ MJ\ kg^{-1}$ vs $44 \div 46\ MJ\ kg^{-1}$), which in turns releases water vapour upon combustion with O_2, effectively recycling the initial feedstock in a circular loop. H_2 production is of such strategical importance that a hydrogen-based economy has been proposed as the future paradigm beyond fossil fuels consumption[60]. Within this framework, however, O_2 generation does not offer comparable economic attractiveness and, at industrial scale, air distillation largely outperforms any other production method. The water oxidation half-reaction has been indeed hampering significant advancement in overall water splitting (OWS) research because of its sluggish reaction kinetics[61]. Additionally, simultaneous synthesis of H_2 and O_2 approximately requires 8.7% of the energy stored in the product fuel to prevent flammability of the mixture itself[13]. Overall, significant challenges ought to be overcome in order to reach practical solar-to-hydrogen (STH) conversion efficiency, that was estimated to amount to 5% and 10% for suspended particles photocatalysts and photo-electrochemical devices[10,12]. For the former technology, a remarkable 2% STH efficiency was obtained using a CDots-C_3N_4 composite, with a photo-activity demonstrated over the course of 200 days, yet fundamental intrinsic losses limited reaction's quantum efficiency to 16%.

A major improvement in the field was then reported by Amirav et al., that exploited CdSe@CdS-Pt to demonstrate 100% photon-to-hydrogen conversion efficiency for the H^+ reduction half-reduction[51].

The process relied, however, on harsh basic conditions to accelerate hole extraction, leveraging on the presence of isopropanol as a sacrificial reagent to turn over the catalytic cycle. Later, the Stolarczyk group improved such reaction conditions employing Pt-NRs decorated with a molecular co-catalyst, i.e. $Ru(tpy)(bpy)Cl_2$. This architecture newly exhibited OWS, nevertheless, oxygen evolution quantum yield reached only 0.27% and material's photoactivity abruptly decreased after 2 hours of operation[62].

In light of the oxygen evolution reaction bottleneck, alternative anodic chemistries have been recently proposed in order to upgrade the demanding OWS reaction. In particular, owing to the possibility to decouple the two redox half-reactions into different environments, simultaneous organic transformations and H_2 generation have been demonstrated via photoelectrochemical route[63]. Similar report for particles-based systems are lagging behind because, taken together, there are still considerable challenges to be overcome for full-redox decoupled homogeneous reactions: i) achievement of high performances in mild experimental conditions; ii) extension of catalytic turn-over; and iii) operando characterisation of the reaction mixture. As a result, the present work describes the effort to adopt Pt-SR in the photosynthetic production of solar chemicals, surpassing these limitations and demonstrating simultaneous production of H_2 and value-added oxidative products.

In this chapter we first present screening of feasible organic transformation trough steady-state and time-resolved reductive quenching. We rapidly summarise thermodynamic limitations for such full-cycle redox reactions and later report Pt-SR performance and characterisation under both monochromatic and solar-simulated radiation. Finally, initial evidence for a broad gallery of additional organic transformations corroborates the excellent solar-to-chemical efficiency figures-of-merit for CdSe@CdS-Pt nanorods.

3.2 Spectrophotometric Characterisation of CdSe@CdS SR

The prominent material investigated in this work is core-shell CdSe@CdS seeded rod (SR) nanostructure. Synthesis of such material followed the protocol from

Nakibli and Amirav and is described in Chapter 6[64]. Briefly, SR are composed by a CdSe quantum dot (QD) embedded in a CdS nanorod (NR), with typical dimension of $4.5\ nm$ and $50\ nm$, respectively. Since the bulk Bohr exciton radium for CdSe is $\sim 10\ nm$[65,66] while for CdS it is $\sim 5.5\ nm$[67,68], the structure is quantum confined in the radial direction, but not in the axial one. This is clearly demonstrated in Figure 3.1A, where the first exciton peak of CdSe QDs red-shifts with increasing QD diameter, i.e. decreased confinement yields longer absorption onset wavelength. On the other hand, exciton transition energies are independent of the NR length. Remarkably, carrier motion in the radial and axis direction can be separately described by adiabatic approximation, owing to the large difference in QD size to NR length[69]. When assembled together, SR can be tuned from a type-I to a quasi type-II structure depending on QD diameter, NR length and interfacial strain[70–74]. Optical features of the heterostructure are characterised by a sharp absorption edge of CdS NR shell at $470\ nm$, while strong "band-edge" emission is recorded at $575\ nm$ after radiative recombination in the CdSe QD, which presents a weak absorption band at $570\ nm$. After synthesis, SR nanostructures are sterically stabilised by octadecylphosphonic (ODPA) and phosphonopropionic acid (PPA) ligands and dispersed in toluene, whereas in aqueous environment mercaptoundecanoic acid (MUA) ligands stabilised SR via electrostatic repulsion.

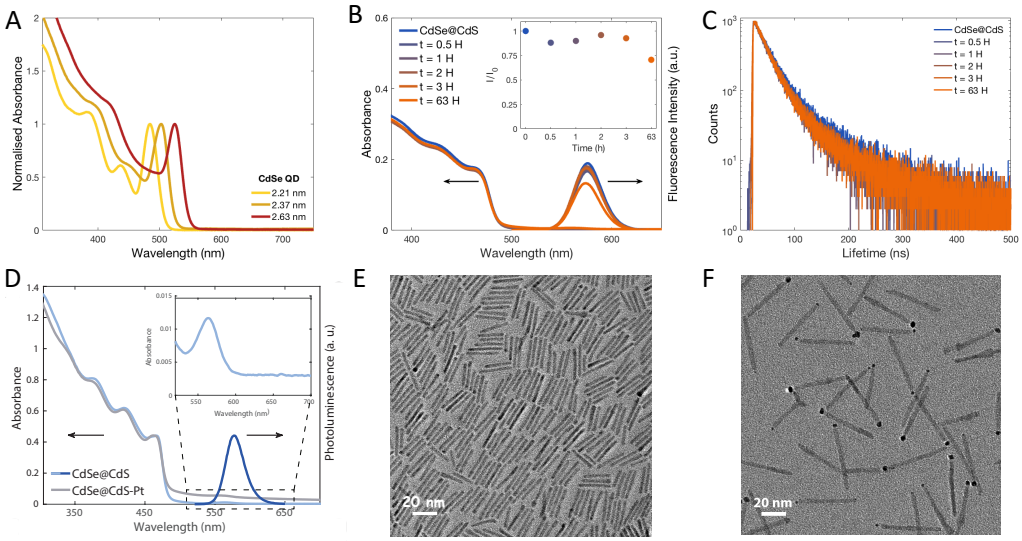

Figure 3.1. ***Spectroscopic and material's characterisation of bare and Pt-tipped CdSe@CdS SR.***

A) Absorption spectra of different-sized CdSe QDs. B) Absorption (left-hand side axis), fluorescence (right-hand side axis) and C) lifetime traces of SR registered between 0 (blue curve) and 63 hours (orange curve) of continuous LED ($\lambda = 455\ nm$) irradiation. D) Absorption (left-hand side axis, light-blue and silver curves), fluorescence (right-hand side axis, dark-blue curve) and TEM characterisation of the synthesised E) bare and F) Pt-tipped SR. Inset in Figure 3.1D highlights the CdSe QDs absorption onset when embedded in CdS NR shell.

Figure 3.1B shows that CdSe@CdS are extremely photostable when dispersed in degassed toluene, perfectly retaining optical properties even after $63\ H$ of continuous irradiation. On the other hand, MUA ligands are easily oxidised by the photo-generated VB h^+ when SR are continuously irradiated. This causes ligand detachment, which is detected by an increase in emission intensity, and prompt deterioration of NRs. For this reason, we typically perform ligand exchange, i.e. organic to aqueous phase transition, just before any spectroscopic or photocatalytic experiments.

The solvent in which SR are dispersed generated different photophysical behaviour, that can be detected, for example, in lifetime measurements. Figure 3.1C shows a characteristic emission intensity decay curve of NRs in toluene, described by a multi-exponential law:

$$I(t) = \sum_{i=1}^{n} \alpha_i \exp\left(-t/\tau_i\right) \qquad \textbf{3.1}$$

where τ_i represent different excited-state lifetimes, that contribute with a fractional contribution $f_i = \alpha_i\tau_i / \sum_j \alpha_j\tau_j$ to the average excited-state lifetime, defined as follows[75]:

$$\bar{\tau} = \frac{\sum_{i=1}^{n} \alpha_i {\tau_i}^2}{\sum_{i=1}^{n} \alpha_i \tau_i} \qquad \textbf{3.2}$$

Table 3.1 summarises the values measured in both organic and aqueous solvent, that are in good agreement with the ones obtained by Tarafder, Alivisatos et al.[76]. Goodness-of-fit was assessed through the reduced chi-squared methods, that is defined as follows:

$$\chi_R^2 = \left(\sum_{i=1}^{N} \frac{[N(t_i) - N_C(t_i)]^2}{N_C(t_i)} \right) / \nu \qquad \textbf{3.3}$$

where $N(t_i)$ and $N_C(t_i)$ represent the measured and expected values, while ν is the number of datapoints used in the fitting.

	$\tau_1\ (ns)$	$f_1\ (\%)$	$\tau_2\ (ns)$	$f_2\ (\%)$	$\bar{\tau}\ (ns)$	χ_R^2
SR-toluene	26.8	97	130.6	3	40.2	1.03
SR- H_2O	6.7	96	29.5	4	10.4	1.07

Table 3.1. ***Excited-state lifetime of CdSe@CdS SR in organic and aqueous solvents.*** Data were fitted using a linear least-squares method.

The two-exponential decay behaviour can be physically rationalised by the unavoidable polydispersity of the sample, but also by the different exciton dynamics in the axial or radial direction.

In order to obtain efficient charge separation, 'bare' CdSe@CdS SR are then decorated with Pt, Ni or Au tips at their apexes, following protocols developed by Mokari, Banin et al.[47,48,77]. Notably, the efficiency of charge separation across the heterojunction is close to unity[78], demonstrated by the complete fluorescence quenching of Pt-SR. Amirav and Alivisatos later demonstrated, through single-NR photoluminescence investigation, that charge-separated states for Pt-SR are long-lived - $100\ ns$ - and addition of reductive quenchers such as methanol or isopropylalcohol further extend it up to $330 \pm 35\ ns$[50]. This superior optoelectronic behaviour ensues from ultrafast h^+ transfer from CdS NR to CdSe QD, occurring on a $650\ fs$ timescale[79]. Interestingly, a body of research form the Dukovic group

recently demonstrated that trapped h^+ can profoundly affect the behaviour of nonuniform NR morphologies, i.e. presenting "bulb" regions with decreased quantum confined[80–83]. In such structures, the longest live charged separated state is formed by rod-trapped h^+ and bulb-localised e^-, effectively revealing an alternative to heterostructures design for photochemical device applications.

3.3 Fluorescence Quenching Screening

The assessment of alternative oxidative chemistries beyond water oxidation opens experimental investigation to a vast chemical exploration space. Notably, in the catalysis research field, that has surely represented one the most ground-breaking discipline for human civilisation since last century, scientific development has been plagued by a refractory trail-and-error approach. Both design of new catalytically active materials and screening of reaction conditions heavily relied on such method. Nevertheless, development of modern high-throughput computational techniques, coupled to the leap in the advancement of machine and deep learning tools, are effectively subverting this trend[84]. Fundamental feedstock for such data-driven operational tools are material's descriptors, that represent the theoretical driver for the construction of materials-function classification.

In the case of light-promoted catalytic reactions, photo-induced electron transfer effectively describes the capability of the active species to interact with reagent moieties. To this extent, fluorescence quenching establishes a fast, readily accessible and rigorous technique to characterise photochemically-active semiconductors. Recently, Glorius et al. termed luminescent spectroscopy screening as a "mechanism-based" approach which surpasses experimental serendipity discovery[85]. Remarkably, analysis of luminescence quenching has considerable advantages compared to ultrafast and electrochemical techniques. On one hand, transient absorption measurements require complex and expensive apparatuses and non-trivial data analysis, while, on the other hand, the irreversible

nature of numerous chemical reactions hinders rigorous electrochemical characterisation.

In light of this, fluorescence quenching screening was elected to discover possible oxidative transformation to be performed by CdSe@CdS nanorods. Figure 3.2A presents the gallery of organic moieties along with the intensity of fluoresce decrease, according to the formula: $\% = \left(1 - I_{QUENCH}/I_0\right) \cdot 100\%$. It should be noted that functionalisation of CdSe@CdS with metal tips quenches the luminescence almost completely ($\sim 95\%$), thus spectroscopic screening was carried out using 'bare' nanorods, rather that the full CdSe@CdS-Pt photochemical unit. Remarkably, bare NRs represent an ideal platform for optical spectroscopic studies, owing to their exceptional molar extinction coefficient ($\varepsilon \sim 10^7\ M^{-1}cm^{-1}$ at $\lambda = 400\ nm$) and high fluorescence quantum yield, typically around 40% (see relative quantum-yield measurement[86] in Figure 3.3A). In order to assess photoluminescence behaviour in reaction like conditions, we performed screening experiments in aqueous solution, typically using a 60:40 water/acetonitrile ratio when organic molecules resulted insoluble in pure water.

Among the family of electron-donors tested, we selected compounds presenting different functional groups and relative derivatives that are of industrial importance. In particular, aromatic amines and alcohols presented noticeable fluorescence quenching, the amount being, as expected, proportional to the oxidation potential.

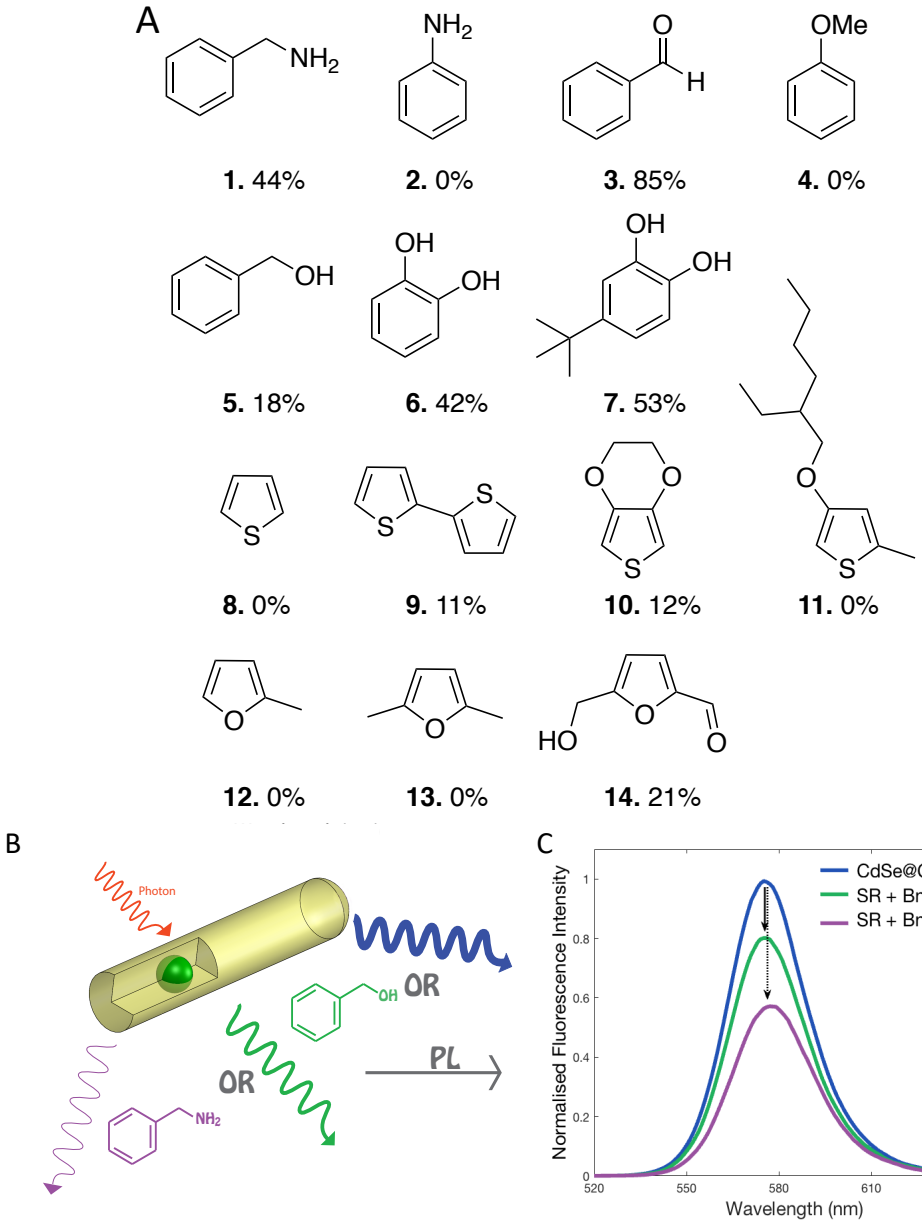

Figure 3.2. ***Fluorescence Quenching Screening of electron-donor moieties for oxidative organic transformations.***

A) Gallery of organic compounds screened, along with fluorescence quenching efficiency at 0.05 M concentration: 1) benzylamine, 2) aniline, 3) benzaldehyde, 4) anisole, 5) benzylalcohol, 6) catechol, 7) tert-butyl catechol, 8) thiophene, 9) bithiophene, 10) 3,4-ethylenedioxythiophene, 11) 4-((2-ethylhexyl)oxy)-2-methylthiophene, 12) 2-methyl furan, 13) 2,5-dimethylfuran and 14) 5-hydroxymethylfurfural. B) Schematic representation of fluorescence quenching and C) normalised fluorescence intensity data for bare CdSe@CdS NRs and its interaction with 0.15 mmol of benzylamine ($BnNH_2$) and benzylalcohol (BnOH) in a H_2O/CH_3CN (60/40) solution.

For example, benzylamine and benzylalcohol, that have $E_{ox}^{0} = 1.32\,V$ vs NHE and $E_{ox}^{0} = 1.98\,V$ vs NHE, showed respectively 44% and 18% quenching, evidenced in Figure 3.2C. Surprisingly, we did not record decrease in intensity

emission using aniline, which oxidation potential was estimated around $1\,V$ vs NHE, while catechols and its derivatives, which are widely employed in the production of fertiliser, presented significant quenching reaching $\sim 50\%$. Thiophene derivatives also demonstrated weak interaction with NRs, yet 3,4-ethylenedioxythiophene (EDOT) showed non-negligible quenching and was later considered due to the possibility to photochemically synthesise the corresponding p-type conductive polymer. To this extent, biomass derivates like 5-(hydroxymethyl)furfural and similar furans were also screened for their prospective conversion in polymers which can substitute polyethylene (PET).

Initially, we focused on further investigation of benzylamine ($BnNH_2$) and benzylalcohol (BnOH) spectroscopic behaviour by means of Stern-Volmer analysis. Figure 3.3 B-D present data for the complete spectrophotometric characterisation of the CdSe@CdS-quencher system.

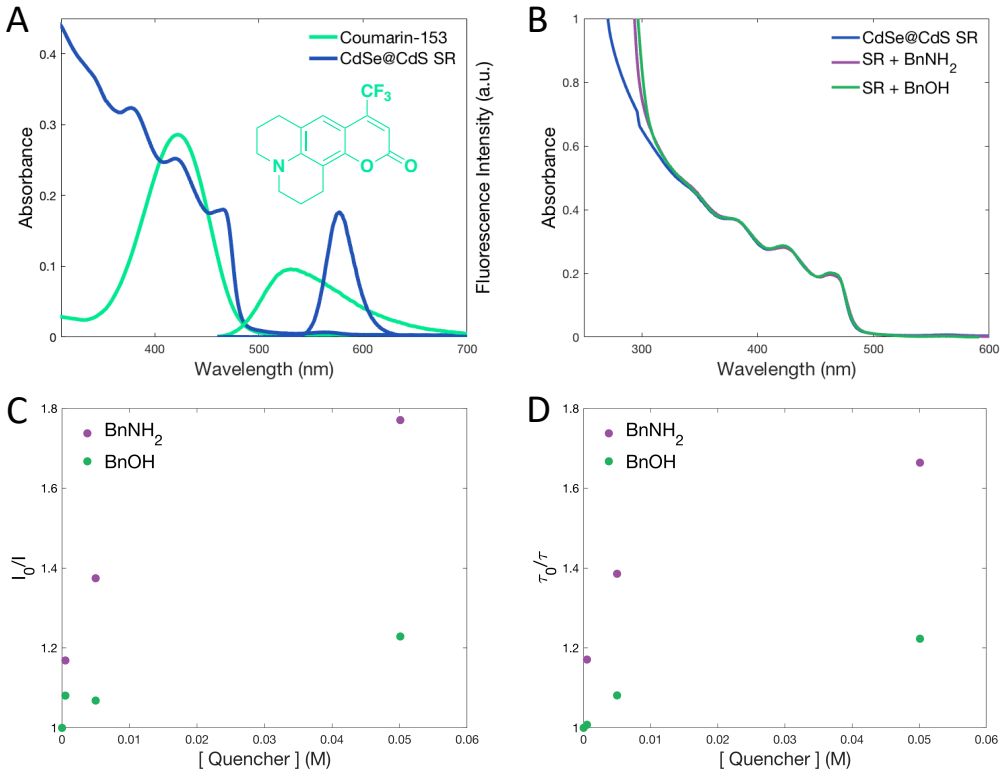

Figure 3.3. ***Spectroscopic characterisation of the CdSe@CdS-Quencher system.***
A) Relative fluorescence quantum yield of CdSe@CdS NRs in toluene, measured using Coumarin-153 as fluorescence standard ($\Phi_f = 0.53$ in ethanol), $\lambda_{ex} = 400\,nm$[34]. B) Absorbance, C) fluorescence and D) lifetime data for Stern-Volmer analyses of the bare NRs- $BnNH_2$/BnOH system in a H_2O/CH_3CN (60/40) solution.

Specifically, absorption spectra recorded before and after addition of the organic molecules reveal unaltered spectral features for the nanorods, thus ruling out ground-state interaction between the luminophore and both quencher species. Secondly, analysis of the decay behaviour of fluorescence and lifetime signals with increasing $BnNH_2$ and BnOH evidence a non-trivial interpretation scenario. On one hand, the decrease in emission intensity follows a trend consistent to lifetime decay, conforming to classical dynamic-type quenching of organic and organo-metallic luminophores. On the other hand, the unusual non-linear slope at high quencher concentrations, reveals a saturation behaviour that was previously reported for protein moieties[75], but also for similar colloidal nanostructures[83,87,88].

Based on the data collected, we considered two different approaches to describe the non-linear saturation behaviour, the first following Stern-Volmer analysis and the second according to Langmuir isotherm model.

Firstly, downward curving Stern-Volmer is a characteristic signature of quencher interaction with enzyme-like moieties exhibiting distinct surface-recognition sites. An example of such peculiar architecture is provided in Figure 3.4A, showing how endonuclease III enzymes displays tryptophan residues embedded in exposed or buried domain, thus presenting different accessibility for quenchers. This situation is analogous to quenching processes characteristic of two fluorophores populations, one interacting to a lower degree with respect to the other. Nonetheless, the resulting downward curving trend of Stern-Volmer analysis can be mathematically analysed by considering the difference between quenched and unquenched emission spectra, $\Delta I = I_0 - I$. In this way it is possible to separate the contribution to emission quenching for sites with distinct accessibility into $I = I_{0,a} + I_{0,b}$, and in turn deriving a quenching constant for the accessible fraction ($k_{SV,a}$) as follows:

$$I_0 = \frac{I_{0,a}}{1 + k_{SV,a}[Q]} + I_{0,b} \qquad \textbf{3.4}$$

After some mathematical reorganisation, a modified Stern-Volmer equation is obtained by considering the difference ΔI:

$$\frac{I_0}{\Delta I} = \frac{1}{f_a k_{SV,a}[Q]} + I_{0,b} \qquad \textbf{3.5}$$

where f_a designates the fraction of initial fluorescence that is accessible to quenching:

$$f_a = \frac{I_{0,a}}{I_{0,a} + I_{0,b}} \qquad \textbf{3.6}$$

By plotting $I_0/\Delta I$ vs $1/[Q]$ it is therefore possible to graphically extrapolate values for f_a and $k_{SV,a}$. In the former case, the inset of Figure 3.4B shows that the intercept of the modified Stern-Volmer curve yields a value of $f_a = 0.49$. A physical interpretation of this situation is straightforward when considering that at infinite quencher concentration ($1/[Q] = 0$), only the inaccessible fluorophore fraction will still contribute to luminescence. Thus, in our case, only half of the population of excited states undergoes collisional quenching, with kinetics estimated in the order of $k_{SV,a} = 391.5\ M^{-1}$. Drawing a parallel to buried and exposed domains present in enzyme structures, we speculate that photo-generated h^+ available for reductive quenching in SR are exposed when trapped at the NR surface or buried when confined in the QD. This interpretation is consistent with the scenario described by latest finding from the Dukovic group discussed in the previous paragraph[81], yet it deserves confirmation by additional ultrafast spectroscopic characterisation.

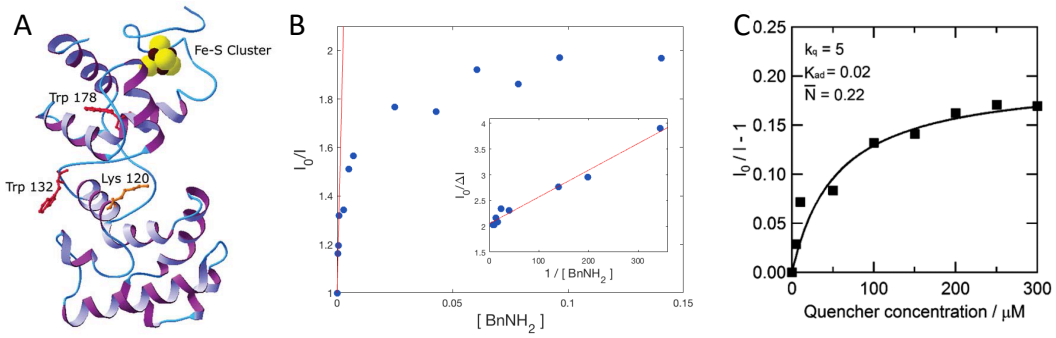

Figure 3.4. ***Fluorescence quenching for the CdSe@CdS-SR/ $BnNH_2$ system: interpretation according to Stern-Volmer and Langmuir models.***

A) Structure of the endonuclease III enzyme, showing exposed (Trp 132) and buried (Trp 178) tryptophan recognition sites[20]. B) Fluorescence quenching curve for the bare-SR/BnNH2 system, fitted with modified Stern-Volmer curve in the low concentration regime (see inset). C) Fluorescence quenching curve of the CdSe QD-benzoquinone systems fitted with a Langmuir model[35].

In the second place, the concave down behaviour recorded in titration experiment was interpreted according the Langmuir isotherm model. The Stern-Volmer analysis does not account for the capacity of the nanostructures surfaces to simultaneously accommodate multiple quencher, as a result, Weiss Kuwabata and Dukovic groups developed a model that could better suit interfacial landscape of such systems[83,87,88]. Within this framework, small-organic molecules are considered permeable to some extent through the ligand layer. Percolation through the nanostructure ligand layer, that should be therefore not perceived as a completely insulating membrane, requires a physical description accounting for the number of available surface sites. This situation is well described by Langmuir isotherm:

$$\theta = \theta_{max} \frac{k_a[Q]}{1 + K_a[Q]} \qquad \textbf{3.7}$$

expressing the mean fractional surface coverage θ of quenchers on the nanostructure, in terms of the saturation fraction θ_{max} and adsorption constant K_a. The latter quantity depends only on system's temperature and change in free energy upon quencher adsorption, but not on nanostructures concentration. Nonetheless, because of the change in surface ligand density upon dilution, Langmuir isotherm should be adapted into a function describing fractional surface coverage of *available* surface sites, θ_a. This accounts for changes in exposed surface area upon dilution and was described using Tachiya model for heterogeneous micellar systems, who used a binomial distribution instead of the Poisson model to include saturation phenomena in surface coverage[89]. Weiss and Kuwabata adapted this model to colloidal nanostructures, expressing the probability of finding m adsorbed quenchers in an ensemble of QDs with N *total* surface sites as follows:

$$P(m|N, \theta_a, \eta) = \sum_{n=0}^{N} P_{sites}(n|N, \eta)\, P_{quencher}(m|n, \theta_a) \qquad \textbf{3.8}$$

The first term refers to the probability of finding a QD with n available surface sites, where η is the mean value of available surface sites, whereas the second term assesses the probability of finding m adsorbed quenchers on a QD with n available surface sites.

Fitting obtained using this model by Uematsu, Kuwabata et al., showed in Figure 3.4C, is in good agreement with the experimental data obtained for the SR/$BnNH_2$

system. The analysis of these authors revealed, however, that non negligible fluctuations in the quenching behaviour occur when nanostructures are probed at different times after ligand exchange. This phenomenon is appreciable also in our case and rigorous assessment of data fitting is currently being developed through additional investigations.

3.4 Thermodynamic Considerations

As thoroughly explained in Chapter 2, solar-to-chemical energy conversion poses thermodynamic limitations to be considered when assessing the effective maximum performance of any photochemical device. A rigorous development of the scientific framework for such conversion process was first developed by Bolton, Haught and Ross[23]. The interested reader is referred to those works, that are distilled into crucial aspects in the present section. In particular, the ideal limiting solar-to-chemical conversion efficiency is defined as the product three terms: i) of the fraction of absorbed photon with $E < E_g$ (η_{abs}), ii) the fraction of excited-states converted into chemical energy (η_c) and iii) the quantum efficiency of the solar-to-fuel conversion process (η_ϕ):

$$\eta = \eta_{abs}\eta_c\eta_\phi \qquad \textbf{3.9}$$

While η_{abs} and η_ϕ are straight-forwardly obtained by computation of the integrated photon flux determined by E_g and by experimental assessment of QE_{PTH}, respectively, η_c is defined as follows:

$$\eta_c = \frac{E_g - E_{loss}}{E_g} \qquad \textbf{3.10}$$

Here, it is possible to notice that E_{loss} ($[J]$) includes photophysical and photochemical processes competing with conversion of excitation energy into chemical energy. Irrespective of the mechanism of quantum conversion, entropic losses inevitably reduce the chemical potential that can be extracted by an excited state, whose energy is determined by E_g. For photochemical processes, entropy is created, in first approximation, by mixing of the ground and excited state populations[90]:

$$E_{loss} = E_g - E_{redox} \approx T\Delta S_{mix} \quad [J] \qquad \textbf{3.11}$$

where E_{redox} ($[J]$) represents the net available work that can be extracted by the quantum converter to carry out a specific reaction. Figure 3.5A shows that, in the region of interest for solar photochemistry ($400\,nm \leq \lambda_g \leq 1000\,nm$), such losses are estimated in the order of $E_{loss} = 0.40 \pm 0.07\,eV$. In the case of electrochemical conversion processes, the Gibbs free energy (ΔG_{redox}) per mole required for a specific redox reaction is produced across electrochemical potential μ_i:

$$\mu_i = \frac{\Delta G_{redox}}{n} = \widetilde{\mu}_i - z \cdot \mathcal{F} \cdot E_i^0 \quad [J\,mol^{-1}] \qquad \textbf{3.12}$$

where n is the number of moles, $\widetilde{\mu}_i$ the chemical potential of the species i, z represents the number of electrons involved in the reaction, $\mathcal{F}$ the Faraday constant and E_i^0 the electrical potential. The latter quantity is determined by considering the separated red-ox half reactions occurring at the cathode and anode, respectively:

$$E^0 = E^0_{cathode} - E^0_{anode} \quad [V] \qquad \textbf{3.13}$$

For the water-dissociation reaction, redox half-reactions are defined as:

$$2H^+ + 2e^- \rightarrow H_2\,, \qquad E^0_{cathode,pH=7} = -0.414\,[V] \qquad \textbf{3.14}$$

$$H_2O \rightarrow \frac{1}{2}O_2 + 2H^+ + 2e^-\,, \qquad E^0_{anode,pH=7} = 0.816\,[V] \qquad \textbf{3.15}$$

amounting to a total of $E^0_{H^+/OH^-} = 1.228\,V$. Consequently, it follows that promotion of alternative anodic chemistries establishes a different potential barrier, that, in our case, is expressed by the oxidation potential of $BnNH_2$[91] and BnOH[92]:

$$2BnNH_2 \rightarrow BI + NH_4^+ + H^+ + 2e^-\,, \qquad E^0_{anode} = 1.324\,[V] \qquad \textbf{3.16}$$

$$BnOH \rightarrow BnCHO + 2H^+ + 2e^-\,, \qquad E^0_{anode} = 1.98\,[V] \qquad \textbf{3.17}$$

where BI and $BnCHO$ indicate benzylidenebenzylamine and benzylaldehyde, respectively. It is possible to notice that, by coupling H^+reduction and $BnNH_2$/BnOH oxidation, the electrochemical barrier increases to $E^0_{H^+/BnNH_2} = 1.738\,V$ and $E^0_{H^+/BnOH} = 2.394\,V$. Reactions that are more demanding than the OWS reaction require therefore a higher driving force, that in turn determines a threshold wavelength corresponding to the minimum E_{rxn} to be extracted from solar radiation:

$$\lambda_{max} = \frac{hc}{\Delta G_{redox}/_{n_{PS}} + E_{loss}} \quad [m] \qquad \textbf{3.18}$$

This formula expresses the wavelength at which sufficient solar chemical potential is transferred in n_{PS} photosynthetic units to match the reaction electrical potential requirements (E^0). Specifically, for single semiconductor absorbers $n_{PS} = 1$, whereas Z-scheme system exploit two distinct light-harvesting systems, thus $n_{PS} = 2$. Limiting to the case of a single absorber, threshold wavelength can be calculated for the full-cycle redox reactions encompassing simultaneous H^+ reduction and oxidation of water ($\lambda_{max,H^+/OH^-}$), $BnNH_2$ ($\lambda_{max,H^+/BnNH_2}$) or BnOH ($\lambda_{max,H^+/BnOH}$). The values obtained, as shown in Figure 3.5B, are $788\,nm$, $583\,nm$ and $478\,nm$, respectively.

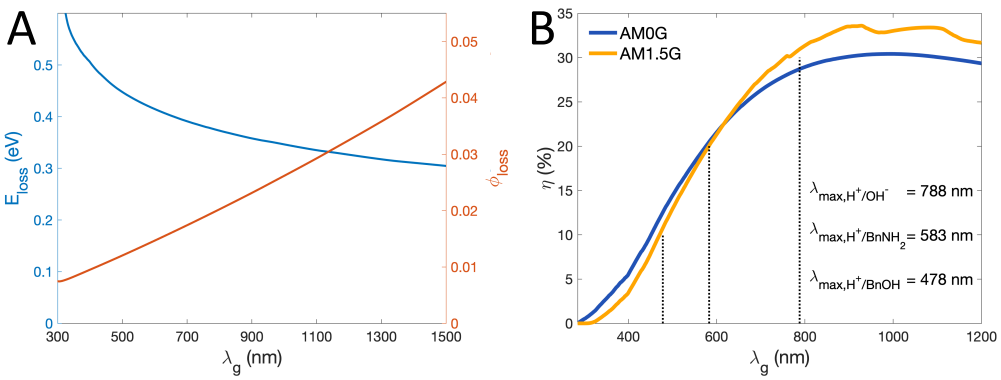

Figure 3.5. ***Entropic losses and corresponding threshold wavelength for overall water splitting, H_2/ benzylidenebenzylamine or H_2 /benzaldehyde reactions.***

A) Energy losses (left-hand side axis, E_{loss}, blue curve) and fraction of dissipated excite-state population (right-hand side axis, ϕ_{loss}, orange curve) as a function of threshold band-gap (λ_g) as defined by Bolton, Ross and Hsiao[38]. B) Maximum solar-to-chemical efficiency for the simultaneous reduction of H^+, coupled to water, benzylamine and benzylalcohol oxidation as a function of threshold band-gap. Maximum threshold to drive the respective reactions *(λ_{max})* are calculated for the AM1.5G solar spectrum (orange curve).

Knowledge of the threshold wavelengths required to carry out the different reactions allows to calculate the fraction of solar spectrum available to perform them, thus determining η_{abs}. Moreover, η_c can be computed by evaluating the E_{loss} function at λ_{max}. Finally, overall maximum solar-to-chemical energy conversion is determined, according to Equation 3.18, by assuming unitary quantum efficiency η_ϕ. The results of such calculation, that are presented in Figure 3.6, yield values of $\eta_{max,H^+/OH^-} = 31\%$, $\eta_{max,H^+/BnNH_2} = 20\%$ and $\eta_{max,H^+/BnOH} = 11\%$.

Table 3.2 summarises the thermodynamic framework comparing OWS with alternative full-cycle redox transformations based on H^+reduction and $BnNH_2$ or BnOH oxidation.

Reaction	$E^0(V)$	$\lambda_{max}(nm)$	$E_g(eV)$	$E_{loss}(eV)$	$\eta_{abs}(\%)$	$\eta_c(\%)$	$\eta_{max}(\%)$
H_2/O_2	1.228	788	1.57	0.375	45	0.76	31
H_2/BI	1.738	583	2.13	0.427	21	0.80	20
$H_2/BnCHO$	2.394	478	2.84	0.489	6	0.82	11

Table 3.2. ***Thermodynamic limitations for simultaneous H_2 production coupled to O_2, benzylidenebenzylamine (BI) and benzylaldehyde (BnCHO) synthesis.***
For each reaction are specified the electrochemical potential (E^0), maximum wavelength to be used to drive the reaction (λ_{max}), corresponding band-gap (E_g), energy losses at the threshold wavelength (E_{loss}), absorption (η_{abs}), chemical (η_c) and maximum (η_{max}) efficiencies.

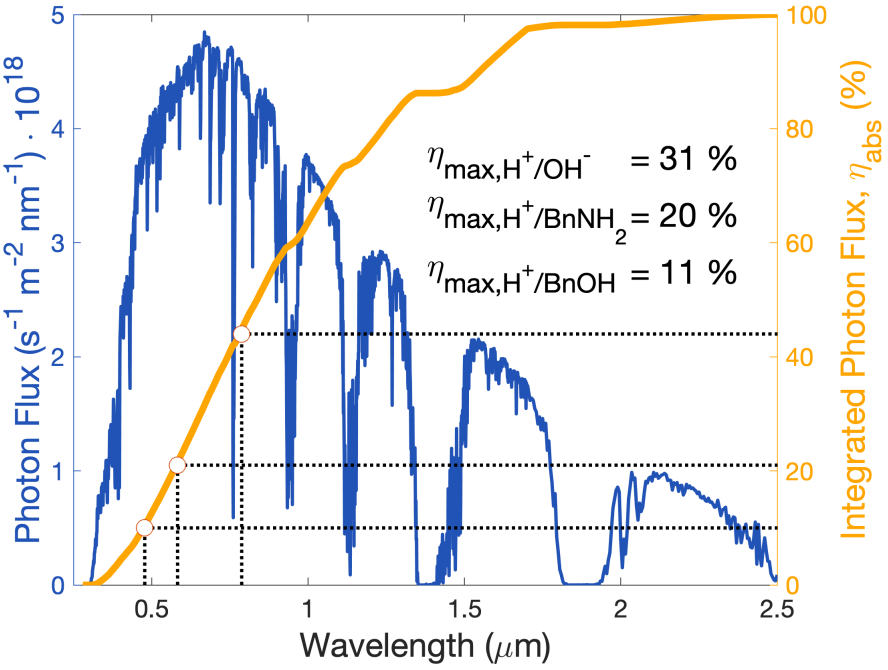

Figure 3.6. ***Maximum thermodynamic solar-to-chemical energy conversion for overall water splitting, H_2/ benzylidenebenzylamine or H_2 /benzaldehyde reactions.***
Reaction maximum efficiencies are indicated along with the fraction of photon absorbed (right-hand side axis, η_{abs}, orange curve) according to the AM1.5G photon flux (left-hand size axis, blue curve).

3.5 Light-to-chemical energy conversion

Following rigorous assessment of $BnNH_2$ and BnOH as alternative redox partner for the water reduction half-reaction, we performed photochemical experiments under various conditions and using different reactor set-up. This effort aimed to provide evidence for interlaboratory reproducibility, in light of the artificial figures-of-merit sometimes reported in this research field[58]. In particular, all the experiments were conducted in gas-tight reactor, after regular calibration of the gas-chromatograph response curve, as detailed in the Appendix. Moreover, reactions were performed at room temperature, under neutral pH and avoiding the use of toxic or non-innocent solvents. In case any organic moiety resulted insufficiently soluble in pure water, we indeed used water/organic solvent mixtures that were limited mostly to acetonitrile or ethanol.

Firstly, we therefore tested Pt-SR for the simultaneous H_2 generation and $BnNH_2$ oxidation, in a water-acetonitrile (60/40) mixture, using concentration of $[Pt-SR] = 3.5 \cdot 10^{-8} M$ and $[BnNH_2]_{t=0} = 0.05\ (M)$ for the NRs and organic substrate, respectively. The initial use of a monochromatic ($\lambda = 455\ nm$) LED source allows us to precisely asses the photon-to-hydrogen quantum efficiency, $QE_{PTH}(\%)$. Figure 3.7A presents the hydrogen production performance under these experimental conditions, corroborating the high sensitivity of NRs to the substrate, as registered during fluorescence quenching.

In particular, the reaction proceeded for nearly 10 hours, reaching a maximum QE_{PTH} of 37%. After sharp activation within the first hour of irradiation, activity persists until the consumption of initial reagent determines a decrease in activity. Remarkably, in spite of the hours-long induction period previously observed for the activation of CdSe@CdS structures[64], $BnNH_2$ oxidation demonstrates excellent kinetics already in the first stages of photosynthetic activity.

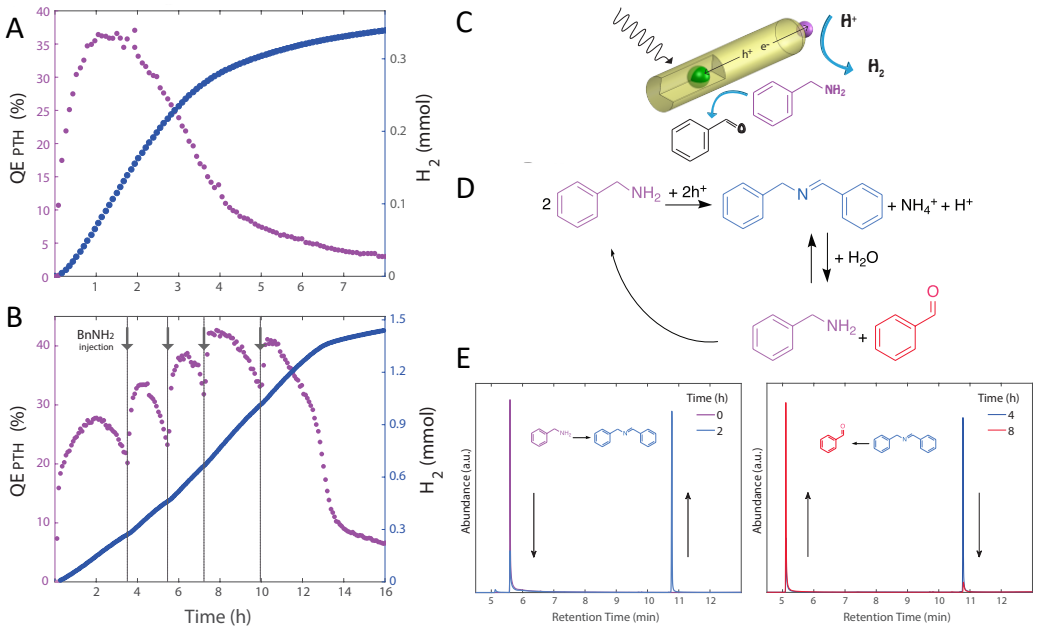

Figure 3.7. ***Photosynthetic H_2 production coupled to benzylamine oxidation via light-to-chemical energy conversion.***

A) and B) H_2 production assessment via photon-to-hydrogen quantum efficiency (left-hand size axes, QE_{PTH}, lilac dotted-curves) and total H_2 $mmol$ produced (right-hand side axes, blue dotted-curves) over time, with and without addition of fresh reagent. C) Schematic representation of the full-cycle photosynthetic redox reaction, entailing concerted H^+ reduction and $BnNH_2$ oxidation. D) Schematic reaction mechanism and E) corresponding GC-MS data evidencing $BnNH_2$ consumption (lilac curve) and subsequent benzylidenebenzylamine (blue curve) and benzaldehyde (red curve) production. Experimental conditions used: $[BnNH_2]_{t=0} = 0.05\ (M)$, *[Pt-SR] = 3.5·10^{-8} M* with catalyst loading = *7·10^{-5} %*, reaction volume = *10 mL*, light source: *455 nm* LED (*50mW*), *T = 25ºC*, solvent: H_2O/CH_3CN (60/40).

Later, when tested upon continuous addition of fresh reagent, at the onset of decreased performance, Pt-NRs show restored and even improved performance. Specifically, over the course of a 16-hour, 1.42 mmol of H_2 are produced with a maximum turnover frequency of ~300,000 H_2 molecules per NR per hour. In this case, ~43% photon-to-hydrogen conversion efficiency is achieved, as shown in Figure 3.7B. In light of this latter result, we expect that photosynthetic operation in flow regimes can further improve overall reaction conditions[93]. Constant replenishment of feedstock reagent can not only extend the current turnover of ~10^6 H_2 molecules per NR produced in 18 hours, but also remove oxidative products from the reaction cell, that might deteriorate activity over time.

Along with the assessment of H_2 production performance, the oxidative reaction mechanism was investigated via Gas Chromatography Mass Spectroscopy (GC-

MS) analysis. Figure 3.7C-D schematically show the balanced oxidation half-reaction, where it is possible to notice that for every two molecules of starting $BnNH_2$, one molecule of BnCHO is obtained. Specifically, two equivalents of benzylamine sequentially harvests, via direct photo-induced ET, two h^+ from the VB of Pt-SR to yield the corresponding benzylic imine (BI). This molecule in turns hydrolyses to $BnNH_2$ and BnOH, providing both a product and new starting reagent for the oxidative half-cycle. GC-MS traces in Figure 3.7E corroborate such mechanism, providing evidence for initial conversion of $BnNH_2$ into BI, followed by gradual and selective transformation of this one into the end product. The residual photosynthetic activity after peak production can be accordingly justified, as oxidation of $BnNH_2$ continues also after complete conversion of the starting substrate.

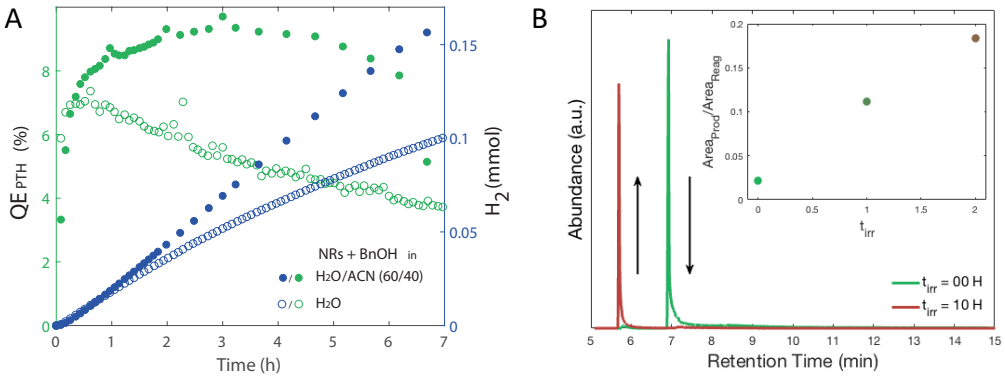

Figure 3.8. ***Photosynthetic H_2 production coupled to benzylalcohol oxidation via light-to-chemical energy conversion.***

A) H_2 production assessment via photon-to-hydrogen quantum efficiency (left-hand size axes, QE_{PTH}, green curves) and total H_2 $mmol$ produced (left-hand side axes, blue curves) over time, in either H_2O (empty dotted-curves) or H_2O/CH_3CN (60/40) (filled dotted-curves) solution. B) GC-MS data evidencing BnOH consumption (green curve) and progressive benzaldehyde (red curve) formation. Experimental conditions used: $[BnOH]_{t=0} = 0.05\ (M)$, *[Pt-SR] = 3.5·10^{-8} M* with catalyst loading = *7·10^{-5} %*, reaction volume = *10 mL*, light source: *455 nm* LED (*50mW*), *T = 25ºC*.

The promising screening results obtained for quenching with benzylalcohol encouraged us to couple H_2 production also with this substrate. We therefore repeated previous experiments using BnOH with the same parameters, adding performance assessment both in pure water and water/acetonitrile mixture. The reduced interaction observed in fluorescent quenching experiments and increased thermodynamic limitations anticipated the reduced yield obtained with BnOH.

Figure 3.8A shows indeed that a maximum QE_{PTH} of 9.4% and 7.3% were obtained in water/acetonitrile mixture and pure water, respectively. For such reaction we registered turn over frequencies, measured in molecules per rod per hour, of ~71,000 in the former and ~58,000 in the latter case. For the photosynthetic reduction of H^+ and oxidation of BnOH we found out that BnCHO is produced via sequential transfer of two h^+ and elimination of two protons. This mechanism is evidenced by GC-MS signals, reported in Figure 3.8B, and is consistent with previously investigated anaerobic electrochemical oxidation of the same compound[94].

Furthermore, additional spectrophotometric analyses were conducted in order to prove material's stability and reaction selectivity during photochemical experiments. Preventing light-promoted degradation of photo-actives component is indeed a crucial factor in the development of photochemical devices[95]. As can be seen in Figure 3.9A, CdSe@CdS-Pt SR show both excellent colloidal and chemical stability when stressed by continuous irradiation. The unaltered quantum features and baseline scattering demonstrates that Pt-SR effectively turnover the photochemical reaction in a catalytic way. We attribute the remarkable stability of the colloidal nanostructure to the excellent kinetics associated with the oxidation half-reaction, that provide efficient photogenerated h^+ removal and prevent photo-corrosive phenomena. The latter process represents the true Achilles' tendon of metal-chalcogenide photosynthetic units, that suffer from severe agglomeration and significant drop in performance when h^+ are accumulated in the semiconductor VB[78,96,97].

Absorbance spectroscopy can reveal further precious insights on the reaction selectivity, as shown in Figure 3.9B. For the case of the H^+/BnOH reaction, for example, dilution of the crude solution mixture evidence, in the UV region, the evolution of additional spectral features with respect to the initial BnOH trace. Firstly, it is possible to notice that BnOH absorbance lies above Pt-SR trace with a distinct feature at $\sim 260\ nm$. With time progression, a shoulder appears around $\sim 290\ nm$, along with the concomitant rise of a principal peak at $\sim 250\ nm$. Such spectral signature perfectly superimposes to the reference benzaldehyde optical

absorbance, that is turn clearly distinguished from benzoic acid spectrum, which presents a dominant peak around $\sim 220\ nm$.

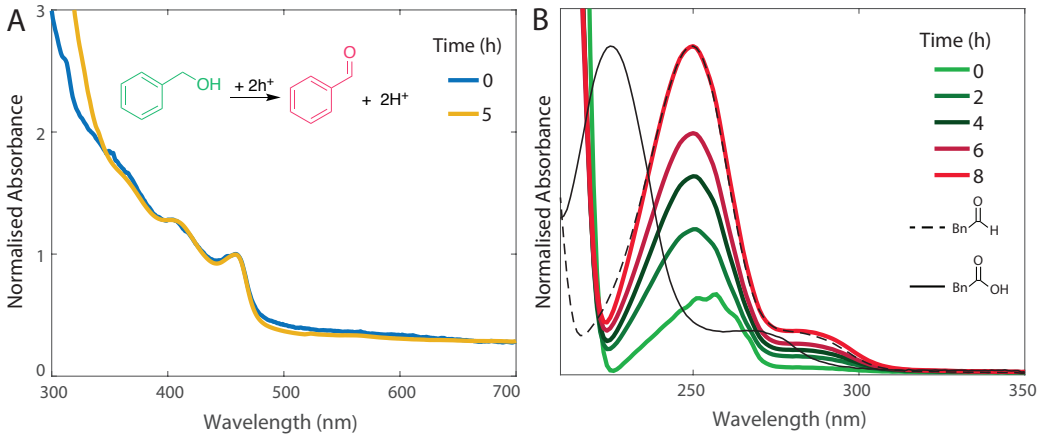

Figure 3.9. ***Spectrophotometric assessment of the photosynthetic reaction: material's stability and reaction selectivity.***
A) Absorption spectra recorded before (blue curve) and after (yellow curve) the photosynthetic production of H_2 and BnCHO. Spectra are normalised at the CdSe@CdS-Pt absorption edge. B) Absorption spectra for H_2/BnCHO reaction aliquots, showing conversion of the initial BnOH (light-green curve) into BnCHO (red curve). Reference traces for BnCHO (black dotted-curve) and BnCOOH (black solid-curve) are added for convenience. Spectra are normalised at the CdSe@CdS-Pt absorption edge.

Importantly, spectrophotometric assessment offers therefore the opportunity to validate proposed reaction mechanism ensuing from traditional chemical analyses. Such strategy has critical implications in the field of photochemistry, where lab-scale investigation are still performed with reactor volumes that are too small to allow for frequent monitoring of reaction intermediates aliquots. Nevertheless, the superior sensitivity of optical spectroscopy tools provides rigorous assessment of minute ($\sim 50\ \mu L$) volumes even at early substrate conversion yields, complementing traditional NMR techniques in the overall chemical characterisation of reaction products.

Finally, control experiments were performed in a water/acetonitrile (60/40) mixture, in absence of (i) Pt-SR, (ii) light, or (iii) hole-scavenger. No H_2 was detected in the former two cases, whereas residual activity ($QE_{PTH} < 0.4\%$) observed in absence of hole scavengers can be ascribed to the combined H_2 generation and photo-oxidation of the mercaptoundecanoic-acid ligands stabilizing the NRs, and even oxidation of the CdS itself. Such detrimental process

unsurprisingly results in the rapid degradation of the colloidal system, which terminates activity within the first hour.

3.6 Solar-to-chemical energy conversion

After properly assessing the quantum efficiency of the reaction performance under monochromatic irradiation[98], photosynthetic activity was assessed using a solar radiation as input source. While QE_{PTH} evaluation is straightforward in the former case, experiments using simulated solar sunlight entail a panchromatic spectrum, whose photon flux can be calculated according to the following formula:

$$J_{ph} = \int_{\lambda_1}^{\lambda_2} \frac{J_{AM1.5G,e,\lambda}}{E_\lambda} \cdot \eta_{abs,\lambda}\, d\lambda \cdot A_\emptyset \quad [\, s^{-1}\, nm^{-1}] \qquad \textbf{3.19}$$

where J_i denote photon -suffix '*ph*'- or energy - suffix '*e*'- fluxes, E the photon energy, $A_\emptyset$ spot-size area and $\eta_{abs,\lambda}$ the fraction of light absorbed by the photocatalyst, or light harvesting efficiency, at each wavelength – suffix λ. The latter quantity, the same used for the calculation of maximum conversion efficiency, is determined by the Beer-Lambert-Bouguer law for liquid solutions:

$$\eta_{abs,\lambda} = 1 - 10^{-A_\lambda} = 1 - 10^{-\varepsilon_\lambda cl} \qquad \textbf{3.20}$$

while the integral is evaluated in a spectral range specified by experimental conditions. As previously mentioned, Pt-SRs present absorption traces characterised by a non-negligible scattering caused by Pt nanoparticles. In order to properly assessed the absorbed photon-flux, we therefore computed the contribution of scattering in two ways: on one hand we fitted absorption curves to the Rayleigh model and, on the other hand, we performed reflectance/transmittance measurements using an integrating sphere.

The intensity of Rayleigh scattering scales with the fourth power of incident wavelength and is expressed as follows:

$$A = log\left(\frac{I_0}{I_0 - I_{scatt}}\right) + A_0 = log\left(\frac{I_0}{1 - k\lambda^{-4}}\right) + A_0 \qquad \textbf{3.21}$$

The formula states that incoming intensity I_0 is reduced by a scattering contribution I_{scatt}, which is proportional to λ^{-4} multiplied by a constant of proportionality k. Figure 3.10A shows that utilisation of a pure scattering model perfectly fits the absorbance traces recorded for three different concentration of Pt-SR, absorbing 68.4% ($A = 0.5$), 90% ($A = 1$) and 99% ($A = 2$) of the incoming light. In the second place, Figure 3.10B presents data collected for Pt-SR when analyses in an integrating sphere setup. It is possible to notice that, in this case, transmittance and reflectance contributions can be satisfactory estimated for diluted samples, however, meaningful characterisation of concentrated solution are hampered by the high scattering contribution.

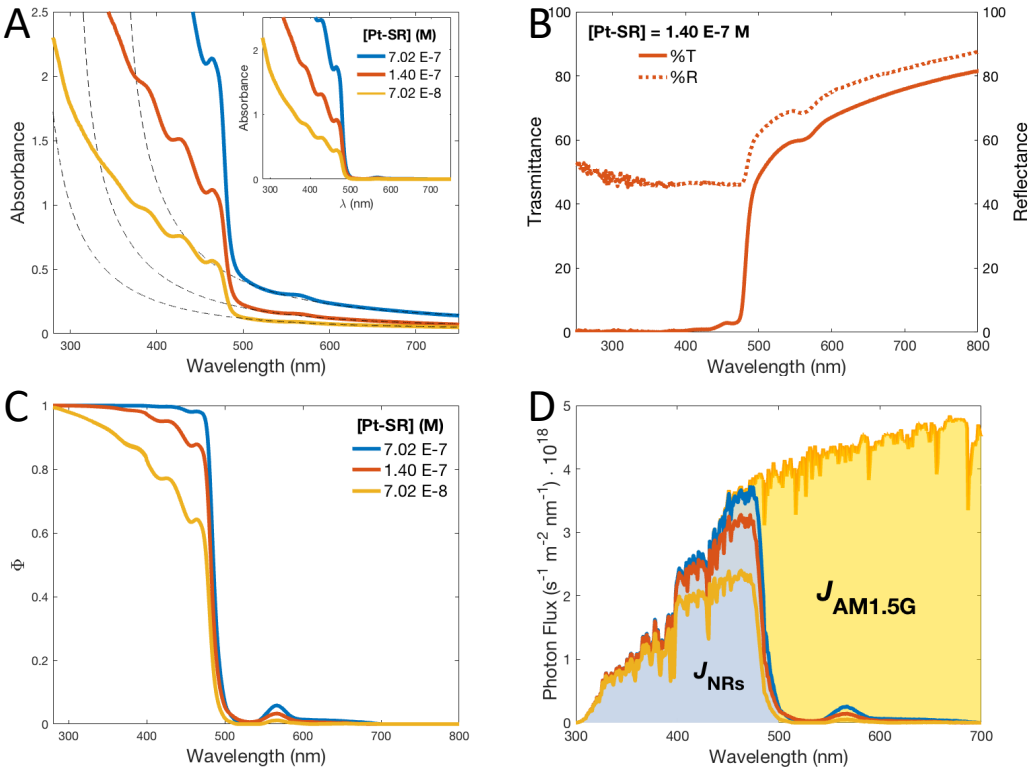

Figure 3.10. ***Absorbance spectroscopy characterisation and computation of the corresponding absorbed photon fluxes for varying [Pt-SR] concentrations.***
A) Absorbance, B) Transmittance (left-hand side axis, solid curve) and Reflectance (right-hand side axis, dotted curve) spectra for [Pt-SR] with concentration of $7.02 \cdot 10^{-7}$ *M* (blue curve), $1.40 \cdot 10^{-7}$ *M* (red curve) and $7.02 \cdot 10^{-8}$ *M* (yellow curve). C) Fraction of light absorbed and D) corresponding absorbed AM1.5G photon flux by the different *[Pt-SR] samples.*

Considering therefore the data provided by absorbance spectroscopy, rigorously fitted with a Rayleigh model, the light harvesting efficiency $\eta_{abs,\lambda}$ can be computed

by expressing UV-Vis data in terms of fraction of light absorbed, as shown in Figure 3.10C. Finally, solar photon fluxes scaled according to NRs absorbance are obtained through equation 3.19. Table 3.3 summarises the parameters obtained after fitting absorbance curve with Rayleigh scattering models, along with the fraction of AM1.5G spectrum absorbed by the different Pt-SR samples, reported in Figure 3.10D.

[Pt-SR] (M)	$A(\lambda = 455\ nm)$	Φ (%)	k (nm^4)	$J_{ph}(s^{-1}m^2)$
$7.02 \cdot 10^{-8}$	0.5	68.4	$1.70 \cdot 10^{10}$	$3.27 \cdot 10^{20}$
$1.40 \cdot 10^{-7}$	1	90	$9.00 \cdot 10^{9}$	$4.03 \cdot 10^{20}$
$7.02 \cdot 10^{-7}$	2	99	$5.01 \cdot 10^{9}$	$4.33 \cdot 10^{20}$

Table 3.3. ***Computation of the absorbed photon fluxes for varying [Pt-SR]***

After rigorously defining the framework to asses quantum efficiency for solar-driven photochemical experiments, we acknowledged the lack of performance metrics that could assess chemical reactions other than overall water splitting. The STH definition is indeed bounded to the realisation of the water reduction and oxidation half-reactions, that add up to $237.1\ kJ\ mol^{-1}$ of chemical potential extracted from solar radiation. In our case, however, the chemical potential of solar radiation is extracted proportionally to the electrochemical potential of $BnNH_2$ and BnOH oxidation previously defined. Express computation of the chemical potential μ for these reactions yields the following values:

$$\mu_{H^+/BnNH_2} = -2 \cdot 96{,}485 \left[\frac{kJ}{V \cdot mol}\right] \cdot \{-0.414 - (1.324)\}[V] = 335.4\ [kJ\ mol^{-1}] \quad \textbf{3.22}$$

$$\mu_{H^+/BnOH} = -2 \cdot 96{,}485 \left[\frac{kJ}{V \cdot mol}\right] \cdot \{-0.414 - (1.98)\}[V] = 462.0\ [kJ\ mol^{-1}] \quad \textbf{3.23}$$

Remarkably, our investigations reveal therefore the necessity to extend the current definition of solar energy conversion limited to STH efficiency. In particular, surpassing the long-standing plague of sacrificial reagents exploitation, we defined a new performance metric accounting for a gallery of different photosynthetic reaction able to extract different amount of chemical potential μ_{rxn} from solar radiation. We conveniently defined such index solar-to-chemical (STC) conversion efficiency:

$$STC = \frac{J_{mol} \cdot \mu_{rxn}}{P_{AM1.5G} \cdot A_{\emptyset}} \cdot 100\% \qquad \textbf{3.24}$$

where J_{mol} is the rate of the reaction ($[\, mol\ s^{-1}\,]$) harvesting a fraction μ_{rxn} of chemical potential ($[\, J\ mol^{-1}\,]$) from sunlight, whose incident power is defined by $P_{AM1.5G}$ ($[\, W\ m^{-2}]$).

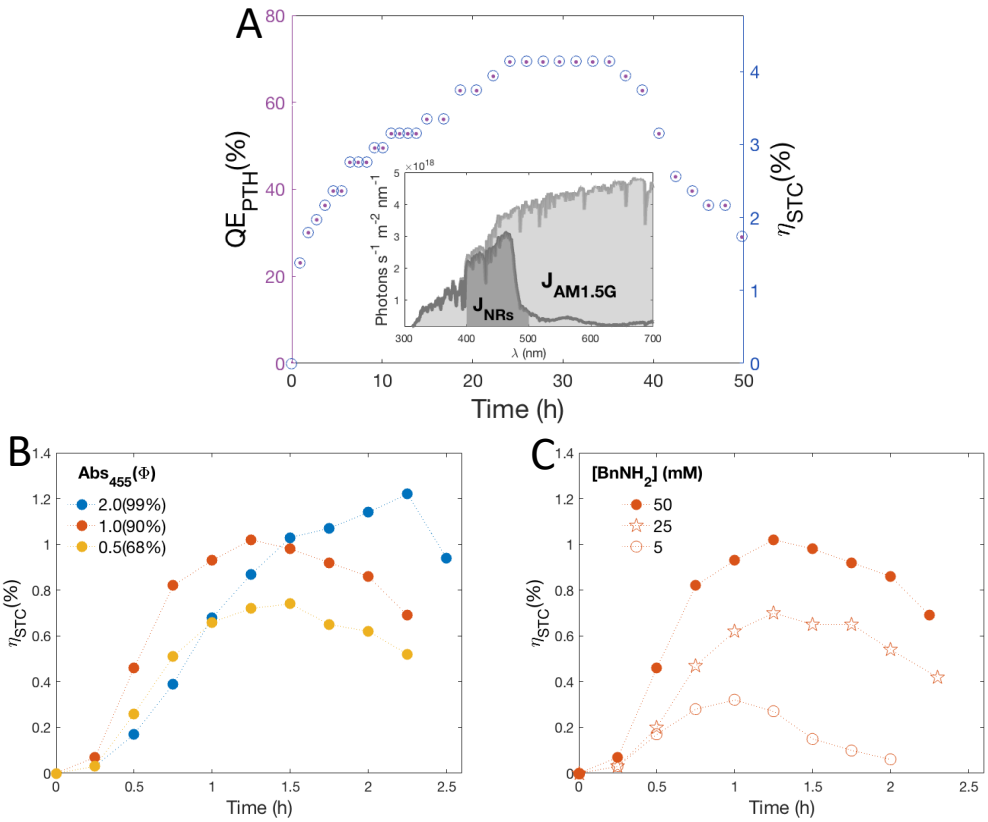

Figure 3.11. ***Photosynthetic H_2 production coupled to benzylamine oxidation via solar-to-chemical (STC) energy conversion.***

A) H_2 production assessment via photon-to-hydrogen quantum efficiency (left-hand size axes, $_{QE_{PTH}}$, lilac dotted-curve) and solar-to-chemical (STC) conversion efficiency (left-hand side axes, blue dots) over time. Experimental conditions: $[BnNH_2]_{t=0} = 0.1(M)$, *[Pt-NRs] = 3.5·10⁻⁸ M* with catalyst loading = *3.5·10⁻⁵ %*, reaction volume = *10 mL*, light source: AMG 0.1 solar-simulator fractioned with a 400nm long-pass filter, *T = 25°C*, solvent: H_2O/CH_3CN (60/40). Inset: AMG1.5 photons flux (light gray curve) superimposed to the scaled photons flux absorbed by NRs (dark gray curve). Dark gray area indicates the fraction of light included between long-pass filter and QD valence band. B) Parametric investigation of the same reaction using different photocatalyst concentrations: 7.02·10⁻⁷ M (blue curve), 1.40·10⁻⁷ M (red curve) and 7.02·10⁻⁸ M (yellow curve) C) Parametric investigation of the same reaction using different $BnNH_2$ concentrations: 50 mM (filled-dots), 25 mM (starred-dots) and 5 mM (empty-dots). Experimental conditions for B) and C) reaction volume = *5 mL,* light source: AMG 0.1 solar-simulator, *T = 25°C*, solvent: H_2O/CH_3CN (60/40).

Figure 3.11A-C present the data for the photosynthetic reduction of H^+ coupled to $BnNH_2$ oxidation under simulated solar-sunlight. Reactions were performed using varying concentration of Pt-SR, starting reagent and different incident solar fluxes, with and without low-pass filters, yet all of them were carried out at room temperature in a water/acetonitrile mixture (60/40). In particular, it is possible to notice that, when irradiated at 0.1 sun (Figure 3.11A), STC efficiency reaches a value of 4.2%. Considering previously calculated ideal solar-to-chemical conversion efficiency for such reaction, this value is one fourth of the thermodynamic limit of 16.8%. To this extent, it is important to underline that the low irradiance used in this experiment corresponds to an absorbed solar photon flux of $J_{ph} = 4.82 \cdot 10^{15}\ s^{-1}$, which is two orders of magnitude lower compared to the photon flux Φ_{ph} used with monochromatic-LED ($1.15 \cdot 10^{17}\ s^{-1}$) or AM1.5G ($1.1 \div 1.5 \cdot 10^{17} s^{-1}$) sources. Being the rate of photochemical reactions proportional to incident light intensity, the reaction performed at 0.1 sun extends to 50 hours, while it reaches peak performance within two hours at AM1.5G. We speculate that, in the former case, sufficient time for ligand reorganisation, as previously reported[51,64], allows for optimal surface exposure of Pt-SR to quenching moieties and consequently improved performance. This is also corroborated by the excellent QE_{PTH} reached after ~25 hours of irradiation, peaking at 69%.

On the other hand, performance at AM1.5G, reported in Figure 3.11B-C, reached STC values between 0.3% and 1.2%, according to the different Pt-SR and $BnNH_2$ concentration used. Figure 3.11B presents data collected for the parametric investigation conducted at varying Pt-NRs absorbances. Specifically, already with a [Pt-SR] concentration of $7.02 \cdot 10^{-8}\ M$, an STC of 0.74% is achieved, with a quantum efficiency of 8.19%. Increasing the catalyst loading boosts STC efficiency above 1%, with minor changes in QE_{PTH}, settling at $9 - 10\%$. Not surprisingly, as long as the initial substrate concentration is held at fixed values, quantum efficiency performance is not relevantly affected by variation in the absorber concentration. This is consistent with fact the photon-to-hydrogen conversion is predominantly governed by the quenching efficiency. Photocatalyst's concentration do not affect neither Stern-Volmer[75] nor Langmuir descriptions[87] (see equations 2.9, 3.5 and 3.7), accordingly QE_{PTH}, i.e. η_ϕ, are demonstrated to be constant at fixed initial substrate

concentration. A different argument holds for the overall STC performance, which scales with the amount of light absorbed according to η_{abs}. To this extent, determination of optimal photocatalyst concentration is of fundamental importance for semiconductor-based systems, as witnessed by the distinctive behaviour of Pt-NRs at $7.02 \cdot 10^{-7}\ M$ (blue curve in Figure 3.11B). Such samples, prepared with a concentration corresponding to total light absorption at the peak excitonic shoulder ($A = 2, \Phi = 99\%$), reach maximum efficiency at delayed timed with respected to the more diluted counterparts. This is possibly justified by non-uniform solution irradiation caused by scattering occurring in the thin sample's layer closest to irradiance source. Figure 3.11C shows instead that, as expected, lower concentration of initial starting reagent reduces reaction time windows. Moreover, the lower STC efficiencies observed with decreasing initial $BnNH_2$ concentration, spanning from $STC = 0.32\%$ ($QE_{PTH} = 2.71\%$) for $[BnNH_2]_{t=0H} = 5\ mM$ to $STC = 1.02\%$ ($QE_{PTH} = 8.55\%$) for $[BnNH_2]_{t=0H} = 50\ mM$, are consistent with the decreased interaction between quencher and nanorods, as previously investigated by means of fluorescence spectroscopy.

A summary of the parametric study conducted for Pt-SR solar-to-chemical performance for the $H^+/BnNH_2$ photosynthetic reaction using simulated AM1.5G solar source is provided in Table 3.4.

Finally, also for the experiments performed with simulated solar sunlight, control tests carried out in absence of Pt-SR, light and hole-scavenger confirm the light-triggered nature of H_2 and BnCHO generation.

Pt-SR Concentration Optimisation							
[Pt-SR] (M)	# SR	J_{ph} (s^{-1})	J_{H_2} ($mmol\ h^{-1}$)	TOF ($H_2\ SR^{-1}\ h^{-1}$)	TON ($H_2\ SR^{-1}$)	STC (%)	Fig 3.11B
$7.02 \cdot 10^{-7}$	$4.23 \cdot 10^{17}$	$1.51 \cdot 10^{17}$	0.046	$6.55 \cdot 10^{4}$	$1.01 \cdot 10^{5}$	1.22	●
$1.40 \cdot 10^{-7}$	$2.11 \cdot 10^{17}$	$1.41 \cdot 10^{17}$	0.039	$1.10 \cdot 10^{5}$	$1.82 \cdot 10^{5}$	1.02	●
$7.02 \cdot 10^{-8}$	$1.06 \cdot 10^{17}$	$1.14 \cdot 10^{17}$	0.028	$1.59 \cdot 10^{5}$	$2.53 \cdot 10^{5}$	0.74	●
$BnNH_2$ Concentration Optimisation							
[$BnNH_2$] (M)	# SR	J_{ph} (s^{-1})	J_{H_2} ($mmol\ h^{-1}$)	TOF ($H_2\ SR^{-1}\ h^{-1}$)	TON ($H_2\ SR^{-1}$)	STC (%)	Fig 3.11C
50	$2.11 \cdot 10^{17}$	$1.41 \cdot 10^{17}$	0.039	$1.10 \cdot 10^{5}$	$1.82 \cdot 10^{5}$	1.02	●
25	$2.11 \cdot 10^{17}$	$1.41 \cdot 10^{17}$	0.026	$7.51 \cdot 10^{4}$	$1.17 \cdot 10^{5}$	0.70	☆
5	$2.11 \cdot 10^{17}$	$1.41 \cdot 10^{17}$	0.012	$3.49 \cdot 10^{4}$	$3.71 \cdot 10^{4}$	0.32	○

Table 3.4. ***Parametric investigation of the photosynthetic $H^+/BnNH_2$ redox reaction.***

3.7 Alternative Reducing Agents

After thorough investigation of the $BnNH_2$ and BnOH organic transformations, we evaluated additional processes photo-oxidative processive that could prospectively be coupled to H_2 generation. In particular, based on fluorescence quenching screening, we selected candidate substrates that could generate high-value added products, in order to elevate the techno-economic attractiveness of the photosynthetic solar-to-chemical conversion process. To this extent, significant attention was dedicated to the possibility of controlling polymerisation reactions, considering two distinct strategies to be coupled to hydrogen production:

- Photo-oxidative polymerisation reactions
- Polymers photo-reforming.

This effort aims to control via light-triggered pathways bond-breaking and bond-making mechanisms of monomeric and polymeric substrates. Notably, having IUPAC identified reversible deactivation of radical polymerisations as a ground-breaking innovation to be realised in the chemical research field, photochemistry offers an attractive strategy to tackle such challenge[99]. The redox potential of excited-state equivalents can indeed ameliorate the harsh experimental conditions that are frequently used in oxidative polymerisation and polymers degradation reactions.

Firstly, photo-polymerisation reactions targeted the synthesis of p-type compounds such as polyaniline or poly(3,4-Ethylenedioxythiophene) (PEDOT). These materials are commonly used in thin-film photovoltaic devices as hole-selective contacts, thanks to their capability to extract photo-generated h^+ carriers from the active layer and transport them to the metal electrode[100,101]. Moreover, PEDOT was recently reported to efficiently encapsulate nanocrystals synthesised in thermodynamic metastable phases[102]. Similarly, we envisioned the possibility not only to promote photo-oxidative polimerisation with CdSe@CdS SR, but also to create a conductive shell on the surface of the nanostructure. This selective p-type layer was expected to effectively facilitate the removal of h^+ buried in the CdSe QDs, offering an attractive strategy to improve charge extraction in core-shell nanostructures.

In the first place, we performed fluoresce quenching analysis of aniline in aqueous solution. Surprisingly, we observed an enhancement of emission intensity upon increase of organic moiety concentration in solution. This phenomenon, that corresponds to an unusual decrease in the I_0/I ratio upon aniline titration, was nevertheless recently reported for the interaction of a wide variety of colloidal inorganic nanostructures with amine ligands[103]. In this scenario, traps located on the surface of the nanostructure are effectively passivated by the titrant in solution, resulting in a proportional increase in photoluminescence quantum yield with increasing electron-donor concentration. In light of this, we speculated that aniline could similarly interact with SR by percolating through the ligand shell and reduce the concentration of surface traps through Lewis-acid/Lewis-base type coordination. Leveraging on such chemical and optoelectronic interaction, we

performed photochemical irradiation of both Pt-SR and bare NRs solution, in order to be able to assess possible changes in the emission intensity. The results of such experiments are sown in Figure 3.12C-D. It is possible to notice that, while in the first stages of irradiation only minor changes are detected through absorbance spectroscopy, a gelly-like compound precipitates in the reaction solution after overnight monochromatic irradiation. While simultaneous H_2 production performance assessment revealed poor quantum efficiencies ($QE_{PTH} < 2\%$), chemical analyses provided initial evidence of polyaniline formation. By means of matrix-assisted laser desorption/ionisation (MALDI) the presence of short-chained polyaniline assemblies was confirmed, yet the high polydispersity didn't allow for rigorous determination of initial reagent conversion. Furthermore, further ongoing investigations are being conducted in order to determine the possible formation of a polymer/nanostructure composite. On one hand, absorbance spectroscopy measurements focussed on the identification of fine changes in the absorption onset of the CdSe QDs. Through h^+ delocalisation across the surrounding conductive polymer wrap, the decrease quantum confinement is expected to be reflected in a red-shifted absorption edge. On the other hand, TEM analysis has been carried out to image polymeric structure formations around the inorganic nanostructure, using ad-hoc ruthenium tetraoxide stains[104].

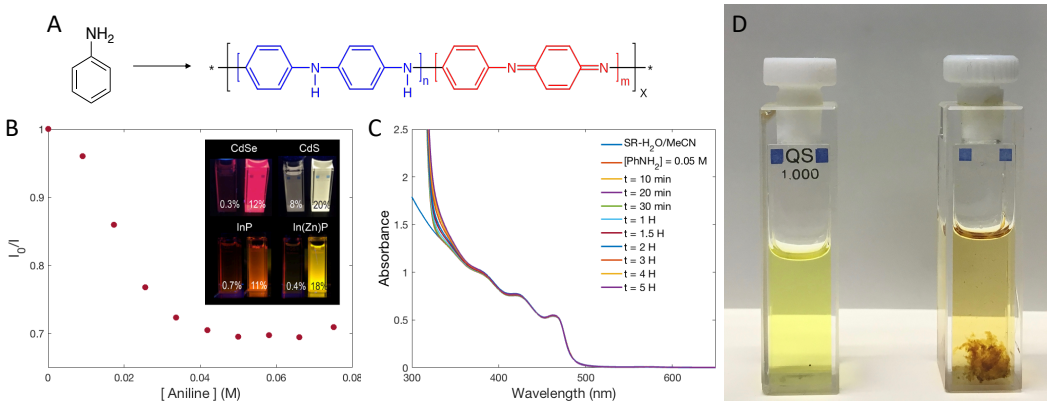

Figure 3.12. ***Photo-oxidation of aniline.***

A) Schematic representation of the polymerisation of aniline into polyaniline. B) Fluorescence quenching of CdSe@CdS SR with aniline. The inset shows fluorescence quantum yield enhancement for different classes of colloidal inorganic nanostructures[53]. C) and D) Absorbance spectra recorded during photo-oxidation experiments, evidenced formation of a solid precipitate after overnight irradiation.

Later, similar photo-polymerisation reactions were explored using 3,4-ethylenedioxythiophene (EDOT) to produce the corresponding polymer. Compared to aniline, EDOT presents a much higher thermodynamic penalty to be overcome, owing to its oxidation potential of $1.9\,V$ vs NHE[102]. Nevertheless, quenching experiments displayed moderate interaction with bare NRs, with a fluorescence decrease amounting to $\sim 12\%$ at $[EDOT] = 0.05\,M$ in water/acetonitrile (60/40) mixture. On one hand, the possibility of directly oxidising EDOT results remarkable with respect to similar photocatalytic approach, which are limited to oxidation of the corresponding trimer (terDOT) owing to its lower oxidation potential ($0.8\,V$ vs NHE)[102]. On the other hand, the scarce optoelectronic interaction was reflected in low reaction kinetics, with observed $\mathrm{QE}_{PTH} < 1\%$ when Pt-NRs where irradiated with a $455\,nm$ monochromatic source. A straightforward way to increase quenching efficiency is to increase the initial substrate concentration, however solubility limitations prevented us to use $[EDOT] > 0.05\,M$. Aiming at avoiding the use of toxic solvents, we tackled this problem by including polystyrene sulfonate (PSS) in the initial reaction cell. This polymer, used to improve EDOT solubility in aqueous environment, allows indeed for the industrial production of EDOT, whose resulting PEDOT:PSS composite has a wide range of application in the optoelectronic field[105]. Initial optimisation of such reactions condition did not yield appreciable changes in the reactions performance, with the use of higher pH conditions ($pH = 8,9,10$) also resulting ineffective in the promotion of polymerisation.

Nonetheless, the use of higher basicity, despite the harsher experimental conditions, presents interesting application opportunities in the field of photo-reforming. Such process accomplishes H_2 generation via light-promoted mechanisms through the use of unprocessed biomass as electron-donor agent, effectively upgrading the value of abundant, cheap and waste resources[106]. In recent years, the Reisner group pioneered the use of inorganic nanostructures, such as core-shell CdSe@CdO_x QDs and carbon nitride composites, to demonstrate efficient hydrogen generation via biomass degradation[107,108]. Later, the same group extended this approach including polyethylene terephthalate (PET) bottles as prospective electron donors to be used in combination with H^+ reduction at high

pH[109,110]. Similar experimental conditions have been previously employed also for CdS-based nanorods, with the remarkable report of perfect quantum-efficiency for H_2 generation coupled to acetone oxidation at $pH = 14$[51,111]. As a result, PET photo-reforming was considered as a valid alternative to extend the use of Pt-SR for photosynthetic purposes. Initially, pH effects on NRs activity was investigated through monitoring of $OH^{\cdot}$ radicals production, as can be seen in Figure 3.13A-B. Firstly, OH^- anions in solution were demonstrated to interact with the excited state of bare NRs, reaching almost 50% quenching efficiency at $[OH^-] = 1\ M$. Later, $OH^{\cdot}$ radicals production via oxidation of OH^- anions was detected via spectrophotometric tools using terephthalic acid (TA) as a fluorescent probe[112]. Figure 3.13B shows that, by monochromatic irradiation of of Pt-SR dispersed in an aqueous solution at $pH = 14$, TA is converted into the corresponding hydroxy product, whose emission rises in the region between $400\ nm$ and $500\ nm$ with increasing irradiation time. Having proved efficient generations of $OH^{\cdot}$ radicals, we proceeded with photocatalytic tests aiming at simultaneously producing H_2 and degrading a commercial PET bottle. Figure 3.13C show hydrogen generation performance over the course of a 40-hour irradiation experiment using $455\ nm$ monochromatic light. Following PET flakes pre-treatment for 5 hours in a 1M KOH solution, used to initiate polymer's chains disassembly and additives removal, QE_{PTH} reached a maximum value of 4%, with a successive gradual decrease in performance, attributed to photocatalysts degradation. As reported elsewhere, PET decomposition is limited by its low solubility in aqueous environment, which in turns augments the crucial role of pre-treatment for the overall reaction efficiency. As a result, in order to increase the NRs interaction with PET assemblies dissolved in solution, two strategies were surveyed: in the first place, the use of aqueous mixtures containing DMSO and, secondly, substitution of the usual MUA ligands with an amphiphilic polymeric moiety. On one hand, DMSO was considered because of the improved solubility of the polymer in such solvent, while, on the other hand, hyperbranched polyethyleneimine (PEI) was exploited for its ability to confer a positive charged to the nanostructure surface. This was expected to facilitate interaction with PET, according to the similar mechanism described for such polymer degradation when promoted by the PET-consuming *Ideonella*

sakaiensis microbe[113]. Reaction optimisation for such experimental parameters is still undergoing for both PET and polylactic acid (PLA) polymers, the latter being evaluated for its higher solubility in aqueous solvent.

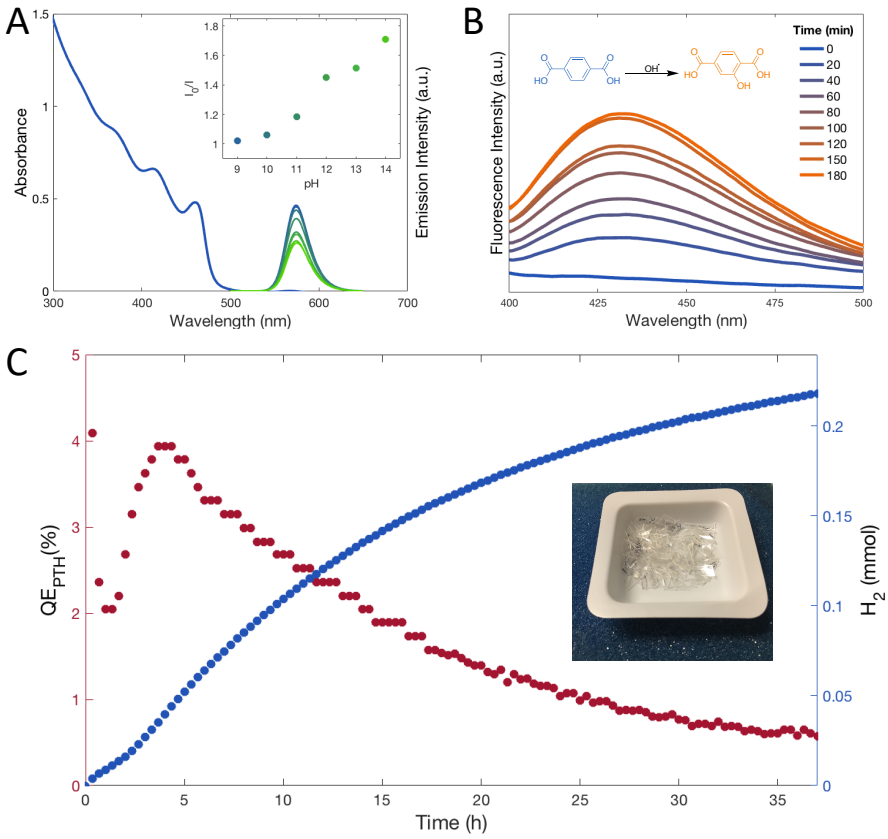

Figure 3.13. ***Photo-oxidation of polyethylene-terephthalate (PET).***
A) Fluorescence quenching of CdSe@CdS SR at increasing KOH concentration. B) Fluorescence intensity monitoring of $OH^{\cdot}$ radicals formation using terephthalic acid as a probe[62]. C) Photo-reforming experiment of a commercial PET bottle (see picture), using Pt-SR in water at pH=14. Left-hand side axis shows quantum efficiency performance (red curve), while on the right-hand size axis the total amount of $H_2\ mmol$ produced is reported (blue curve).

Finally, the capability of CdSe@CdS nanorods to drive organic transformation was tested for the photo-oxidation of several biomass derivatives. In particular, we were intrigued by the possibility to convert 5-hydroxymethylfurfural (HMF) intro a precursor that is later used to obtain PET polymer substituents. As schematically pictured in Figure 3.14A, HMF indeed oxidises, via either acidic or basic pathways, into 2,5-furandicarboxylicacid (FDCA) and is later reacted with ethyene glycol to

yield polyethylene furanoate (PEF). This process in industrially performed by means of chemical oxidation with hydrogen peroxide, tert-butyl hydroxide peroxide or similar, thus photo-oxidations stands again as a compelling strategy to alleviate harsh experimental conditions. Figure 3.14B-C show the characterisation of simultaneous H^+ reduction coupled to HMF oxidation, performed in pure water, in inert atmosphere and under 455 nm monochromatic light. Altough H_2 generation performance is modest, initial un-optimised reactions revealed 50% conversion of the initial starting reagent. High-performance liquid chromatography (HPLC) characterisation reveals, however, the presence of multiple reaction products. Nevertheless, as can be seen from the UV-Vis spectra evolution in Figure 3.14A, transformation of the initial reagents is accompanied by a steep rise in the absorption shoulder above the first exciton peak of Pt-SR, which could offer additional tools to operando characterise and rigorously asses reaction mechanism. Ongoing development are therefore tuning reaction parameters like pH, oxygen content in solution and solvent mixture to eventually guide the selectivity of the oxidation reaction according to similar pathways previously reported.

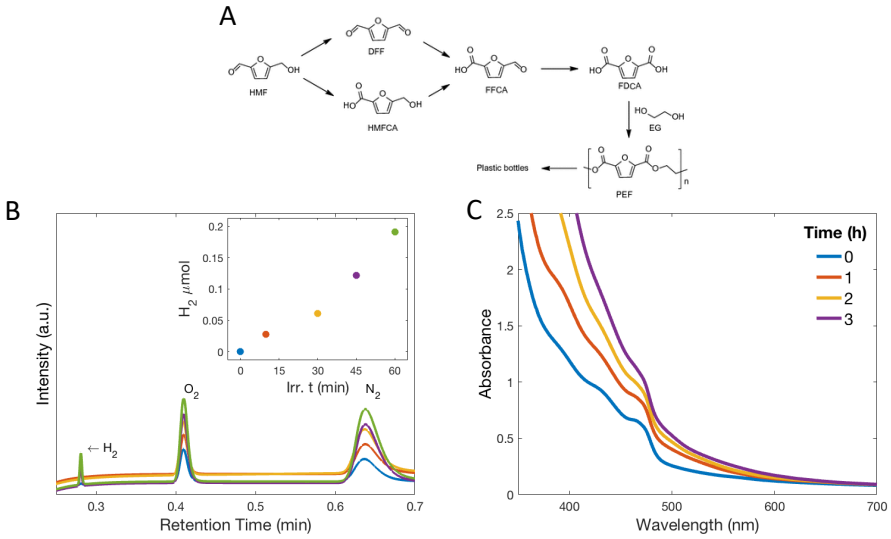

Figure 3.14. ***Photo-oxidation of 5-hydroxymethylfurfural (HMF).***
A) Schematic representation of the oxidative transformation of HMF into 2,5-diformylfuran (DFF), 5-hydroxymethyl-2-furan carboxylic acid (HMFCA), 5-formyl-2-furancarboxylic acid (FFCA), 2,5-furandicarboxylixacid (FDCA), and polymerisation of the latter into polyethylene furanoate (PEF) through reaction with ethylene glycol (EG). B) and C) Photo-oxidation of HMF assessed through gas-chromatography and absorbance spectroscopy.

3.8 Summary

In summary, this chapter has explored the possibility to simultaneously promoting H_2 generation and organic transformations via homogeneous photosynthetic reactions. The long-standing challenge of achieving overall water splitting polarised the research effort in the field, firmly separating investigations on fuel-forming from photo-redox reactions. Nevertheless, the water reduction half-reaction has been thoroughly studied in combination with sacrificial oxidative processes. In light of this, we shifted the approach of half-cycle reaction optimisation, surpassing the use of hole-scavengers for fundamental investigation to value-added chemical production. As a result, we proposed closed redox cycle reaction that entail the simultaneous synthesis of fuels (H_2) and organic oxidative products.

Aiming at establishing insightful material-function correlations, we examined a gallery of different compounds through fluorescence quenching screening method. This strategy, first proposed by Hopkinson, Glorius et al. for organo-metallic photo-active compounds, was equivalently validated for colloidal semiconductor light-harvesters. Remarkably, the technique offers readily available, cheap and rigorous spectroscopic data, allowing us to select $BnNH_2$, BnOH, aniline, EDOT and HMF as candidate substrate for prospective photosynthetic transformation. The former two molecules evidence strong optoelectronic interaction with CdSe@CdS SR, yielding quantum efficiencies up to 45% when tested under continuous monochromatic irradiation. Using hybrid CdSe@CdS-Pt SR, we estimated that 20% of the incoming power is efficiently converted into stored chemical potential, with turn over frequencies of ~300,000 H_2 molecules per SR per hour.

Later, we envision the demonstration of a proof-of-concept photochemical device powered by solar radiation. To this extent, we thoroughly characterise the optical response of Pt-SR under polychromatic light, inquiring the effect of different irradiance level on catalyst and substrate loading. Notably, quantum

efficiency performance corroborates fluorescence quenching findings, resulting in extensive utilisation of absorbed panchromatic light. Having realised a truly catalytic photosynthetic reaction, we assess the reaction performance by a convenient index, namely solar-to-chemical conversion efficiency, or STC. This figure of merit allows to properly assess any reaction storing chemical potential after solar-energy conversion, thus extending the limited framework of the STH metric used for overall water splitting. To this extent, we compute the efficiency of the H_2 and benzaldehyde forming reaction with an impressive 4.2% and 1.2% values for 0.1 and 1 sun irradiation, respectively. Reaction mechanisms are verified both through mass and optical spectroscopy measurements, the latter offering superior advantages for operando analysis of small-scale processes.

Finally, the photosynthetic activity of hybrid Pt-SR is explored through further photo-oxidative reactions. Initial evidence of light-driven control of polymerisation and de-polymerisation processes is provided for several compounds of industrial interest. In particular, conductive polyaniline and PEDOT synthesis are explored for the formation of novel hybrid nanostructured composited, while photo-reforming of PET and PLA is tackled in sight of possible valorisation of abundant and cheap waste products.

References

1. Pearson, P. N. & Palmer, M. R. Atmospheric carbon dioxide concentrations over the past 60 million years. *Nature* **406**, 695–699 (2000).
2. Sapart, C. J. *et al.* Natural and anthropogenic variations in methane sources during the past two millennia. *Nature* **490**, 85–88 (2012).
3. Cook, J. *et al.* Consensus on consensus: a synthesis of consensus estimates on human-caused global warming. *Environ. Res. Lett.* **11**, 1–7 (2016).
4. *World Energy Outlook 2018*. *International Energy Agency Publications* (2018).
5. Lewis, N. S. & Nocera, D. G. Powering the planet: Chemical challenges in solar energy utilization. *Proc. Natl. Acad. Sci.* **103**, 15729–15735 (2006).
6. Tachibana, Y., Vayssieres, L. & Durrant, J. R. Artificial photosynthesis for solar water-splitting. *Nat. Photonics* **6**, 511–518 (2012).
7. Kornienko, N., Zhang, J. Z., Sakimoto, K. K., Yang, P. & Reisner, E. Interfacing nature's catalytic machinery with synthetic materials for semi-artificial photosynthesis. *Nat. Nanotechnol.* **13**, 890–899 (2018).
8. United States Department of Energy. *DOE Technical Targets for Hydrogen Production from Photoelectrochemical Water Splitting*. (2011).
9. Japanese Ministerial Council on Renewable Energy - Hydrogen and Related Issues. *Basic Hydrogen Strategy*. (2017).
10. Jang, J.-W. *et al.* Toward practical solar hydrogen production-an artificial photosynthetic leaf-to-farm challenge. *Chem. Soc. Rev.* **48**, 1908–1971 (2019).
11. Goto, Y. *et al.* A Particulate Photocatalyst Water-Splitting Panel for Large-Scale Solar Hydrogen Generation. *Joule* **2**, 509–520 (2018).
12. Hisatomi, T. & Domen, K. Reaction systems for solar hydrogen production via water splitting with particulate semiconductor photocatalysts. *Nat. Catal.* **2**, 387–399 (2019).
13. Fabian, D. M. *et al.* Particle suspension reactors and materials for solar-driven water splitting. *Energy Environ. Sci.* **8**, 2825–2850 (2015).
14. Ciamician, G. The photochemistry of the future. *Science.* **36**, 385–394 (1912).
15. Verhoeven, J. W. Glossary of Terms used in Photochemistry. *Pure Appled Chem.* **68**, 2223–2286 (1996).
16. Kisch, H. *Semiconductor Photocatalysis*. (2014).
17. Barber, J. Biological solar energy. *Philos. Trans. Math. Phys. Eng. Sci.* **365**, 1007–1023 (2007).
18. Böer, K. W. The solar spectrum at typical clear weather days. *Sol. Energy* **19**, 525–538 (1977).
19. Blankenship, R. E. *et al.* Comparing Photosynthetic and Photovoltaic Efficiencies and Recognizing the Potential for Improvement. *Science.* **332**, 805–809 (2011).
20. Bolton, J. R. & Hall, D. O. Conversion and Storage. *Annu. Rev. Energy* **4**, 353–401 (1979).
21. Ross, R. T. & Hsiao, T.-L. Limits on the yield of photochemical solar energy conversion. *J. Appl. Phys.* **48**, 4783–4785 (1977).
22. Bolton, J. R. Solar Fuels : The production of energy-rich compounds by the

photochemical conversion and storage of solar energy. *Science.* **202**, 705–711 (1978).
23. Bolton, J. R., Haught, A. F. & Ross, R. T. Photochemical Energy Storage: An Analysis of Limits. in *Photochemical Conversion and Storage of Solar Energy* 297–346 (1981).
24. Bolton, J. R., Strickler, S. J. & Connolly, J. S. Limiting and realizable efficiencies of solar photolysis of water. *Nature* **316**, 495–500 (1985).
25. Archer, M. D. & Bolton, J. R. Requirements for Ideal Performance of Photochemical and Photovoltaic Solar Energy Converters. *J. Phys. Chem.* **94**, 8028–8036 (1990).
26. Shockley, W. & Queisser, H. J. Detailed Balance Limit of Efficiency of p-n Junction Solar Cells. *J. Appl. Phys.* **32**, 510–519 (1961).
27. Baierlein, R. The elusive chemical potential. *Am. J. Phys.* **69**, 423–434 (2001).
28. McConnell, I., Li, G. & Brudvig, G. W. Energy Conversion in Natural and Artificial Photosynthesis. *Chem. Biol.* **17**, 434–447 (2010).
29. Fujishima, A. & Honda, K. Electrochemical Photolysis of Water at a Semiconductor Electrode. *Nature* **238**, 37–38 (1972).
30. Kirch, M., Lehn, J.-M. & Sauvage, J.-P. Hydrogen Generation by Visible Light Irradiation of Aqueous Solutions of Metal Complexes. An approach to the photochemical conversion and storage of solar energy. *Helv. Chim. Acta* **62**, 1345–1384 (1979).
31. Bard, A. J. Photoelectrochemistry and heterogeneous photo-catalysis at semiconductors. *J. Photochem.* **10**, 59–75 (1979).
32. Grätzel, M. Artificial Photosynthesis: Water Cleavage into Hydrogen and Oxygen by Visible Light. *Acc. Chem. Res.* **14**, 376–384 (1981).
33. Đokicá, M. & Soo, H. Sen. Artificial photosynthesis by light absorption, charge separation, and multielectron catalysis. *Chem. Commun.* **54**, 6554–6572 (2018).
34. Serpone, N. *et al.* Why do Hydrogen and Oxygen Yields from Semiconductor-Based Photocatalyzed Water Splitting Remain Disappointingly Low? Intrinsic and Extrinsic Factors Impacting Surface Redox Reactions. *ACS Energy Lett.* **1**, 931–948 (2016).
35. Madelung, O. II-VI compounds. in *Semiconductors: Data Handbook* 173–244 (2004).
36. Steigerwald, M., Bawendi, M. G., Steigerwald, M. L. & Brus, L. E. The Quantum Mechanics of Larger Semiconductor Clusters. *Annu. Rev. Phys. Chem.* **41**, 477–96 (2003).
37. Yang, W. *et al.* Electron Accumulation Induces Efficiency Bottleneck for Hydrogen Production in Carbon Nitride Photocatalysts. *J. Am. Chem. Soc.* **141**, 11219–11229 (2019).
38. Edvinsson, T. Optical quantum confinement and photocatalytic properties in two-, one-and zero-dimensional nanostructures. *R. Soc. Open Sci.* **5**, 180387–180403 (2018).
39. Li, X., Yu, J. & Jaroniec, M. Hierarchical photocatalysts. *Chem. Soc. Rev.* **45**, 2603–2636 (2016).
40. Kovalenko, M. V. *et al.* Prospects of Nanoscience with Nanocrystals. *ACS Nano* **9**, 1012–1057 (2015).

41. Wu, K. & Lian, T. Quantum confined colloidal nanorod heterostructures for solar-to-fuel conversion. *Chem. Soc. Rev.* **45**, 3759–4034 (2016).
42. Alivisatos, A. P. Perspectives on the Physical Chemistry of Semiconductor Nanocrystals. *J. Phys. Chem.* **100**, 13226–13239 (1996).
43. Murray, C. B., Norris, D. J. & Bawendi, M. G. Synthesis and Characterization of Nearly Monodisperse CdE (E = S, Se, Te) Semiconductor Nanocrystallites. *J. Am. Chem. Soc* **115**, 8706–8715 (1993).
44. Weiss, E. A. Designing the surfaces of semiconductor quantum dots for colloidal photocatalysis. *ACS Energy Lett.* **2**, 1005–1013 (2017).
45. Amirav, L. & Alivisatos, A. P. Photocatalytic Hydrogen Production with Tunable Nanorod Heterostructures. *J. Phys. Chem. Lett* **1**, 1051–1054 (2010).
46. Peng, X. *et al.* Shape control of CdSe nanocrystals. *Nature* **404**, 3408–3413 (2000).
47. Mokari, T., Rothenberg, E., Popov, I., Costi, R. & Banin, U. Selective Growth of Metal Tips onto Semiconductor Quantum Rods and Tetrapods. *Science.* **304**, (2004).
48. Habas, S. E., Yang, P. & Mokari, T. Selective Growth of Metal and Binary Metal Tips on CdS Nanorods. *J. Am. Chem. Soc.* **130**, 3294–3295 (2008).
49. Talapin, D. V. *et al.* Seeded Growth of Highly Luminescent CdSe/CdS Nanoheterostructures with Rod and Tetrapod Morphologies. *Nano Lett.* **7**, 2951–2959 (2007).
50. Amirav, L. & Alivisatos, A. P. Luminescence Studies of Individual Quantum Dot Photocatalysts. *J. Am. Chem. Soc.* **135**, 13049–13053 (2013).
51. Kalisman, P., Nakibli, Y. & Amirav, L. Perfect photon-to-hydrogen conversion efficiency. *Nano Lett.* **16**, 1776–1781 (2016).
52. Amirav, L., Oba, F., Aloni, S. & Alivisatos, A. P. Modular Synthesis of a Dual Metal-Dual Semiconductor Nano-Heterostructure. *Angew. Chemie Int. Ed.* **54**, 7007–7011 (2015).
53. Serpone, N. *et al.* Standardization protocol of process efficiencies and activation parameters in heterogeneous photocatalysis: Relative photonic efficiencies ζr. *J. Photochem. Photobiol. A Chem.* **94**, 191–203 (1996).
54. Kisch, H. Semiconductor photocatalysis for chemoselective radical coupling reactions. *Acc. Chem. Res.* **50**, 1002–1010 (2017).
55. Ghosh, I. *et al.* Organic semiconductor photocatalyst can bifunctionalize arenes and heteroarenes. *Science.* **365**, 360–366 (2019).
56. Kisch, H. On the Problem of Comparing Rates or Apparent Quantum Yields in Heterogeneous Photocatalysis. *Angew. Chemie Int. Ed.* **49**, 9588–9589 (2010).
57. Qureshi, M. & Takanabe, K. Insights on Measuring and Reporting Heterogeneous Photocatalysis: Efficiency Definitions and Setup Examples. *Chem. Mater.* **29**, 158–167 (2017).
58. Kunz, L. Y. *et al.* Artificial inflation of apparent photocatalytic activity induced by catalyst-mass-normalization and a method to fairly compare heterojunction systems. *Energy Environ. Sci.* **12**, 1657–1667 (2019).
59. Osterloh, F. E. Photocatalysis versus Photosynthesis: A Sensitivity Analysis of Devices for Solar Energy Conversion and Chemical Transformations. *ACS Energy Lett.* **2**, 445–453 (2017).

60. Coontz, R. *et al.* Toward a Hydrogen Economy. *Science.* **305**, 957–976 (2004).
61. Tang, J., Durrant, J. R. & Klug, D. R. Mechanism of photocatalytic water splitting in TiO_2. Reaction of water with photoholes, importance of charge carrier dynamics, and evidence for four-hole chemistry. *J. Am. Chem. Soc.* **130**, 13885–13891 (2008).
62. Wolff, C. *et al.* All-in-one visible-light-driven water splitting by combining nanoparticulate and molecular co-catalysts on CdS nanorods. *Nat. Energy* **3**, 862–869 (2018).
63. You, B., Han, G. & Sun, Y. Electrocatalytic and photocatalytic hydrogen evolution integrated with organic oxidation. *Chem. Commun.* **54**, 5943–5955 (2018).
64. Nakibli, Y. & Amirav, L. Selective Growth of Ni Tips on Nanorod Photocatalysts. *Chem. Mater.* **28**, 4524–4527 (2016).
65. Norris, D. J., Sacra, A., Murray, C. B. & Bawendi, M. G. Measurement of the size dependent hole spectrum in CdSe quantum dots. *Phys. Rev. Lett.* **72**, 2612–2615 (1994).
66. Ekimov, A. I. *et al.* Absorption and intensity-dependent photoluminescence measurements on CdSe quantum dots: assignment of the first electronic transitions. *J. Opt. Soc. Am. B* **10**, 100–107 (1993).
67. Hoang, T. B. *et al.* Temperature dependent photoluminescence of single CdS nanowires. *Appl. Phys. Lett.* **89**, 1231231–1231233 (2006).
68. Puthussery, J., Lan, A., Kosel, T. H. & Kuno, M. Band-Filling of Solution-Synthesized CdS Nanowires. *ACS Nano* **2**, 357–367 (2008).
69. Shabaev, A. & Efros, A. L. 1D Exciton Spectroscopy of Semiconductor Nanorods. *Nano Lett.* **4**, 1821–1825 (2004).
70. Sitt, A., Sala, F. Della, Menagen, G. & Banin, U. Multiexciton Engineering in Seeded Core/Shell Nanorods: Transfer from Type-I to Quasi-type-II Regimes. *Nano Lett.* **9**, 3470–3476 (2009).
71. Rainò, G. *et al.* Probing the Wave Function Delocalization in CdSe/CdS Dot-in-Rod Nanocrystals by Time- and Temperature-Resolved Spectroscopy. *ACS Nano* **5**, 4031–4036 (2011).
72. Smith, E. R., Luther, J. M. & Johnson, J. C. Ultrafast Electronic Delocalization in CdSe/CdS Quantum Rod Heterostructures. *Nano Lett.* **11**, 4923–4931 (2011).
73. Wu, K. *et al.* Universal Length Dependence of Rod-to-Seed Exciton Localization Efficiency in Type I and Quasi-Type II CdSe@CdS Nanorods. *ACS Nano* **9**, 4591–4599 (2015).
74. Christodoulou, S. *et al.* Band structure engineering via piezoelectric fields in strained anisotropic CdSe/CdS nanocrystals. *Nat. Commun.* **6**, 7905–7912 (2015).
75. Lakowicz, J. R. *Principles of Fluorescence Spectroscopy*. (2006).
76. Tarafder, K., Surendranath, Y., Olshansky, J. H., Alivisatos, A. P. & Wang, L.-W. Hole Transfer Dynamics from a CdSe/CdS Quantum Rod to a Tethered Ferrocene Derivative. *J. Am. Chem. Soc.* **136**, 5121–5131 (2014).
77. Mokari, T., Sztrum, C. G., Salant, A., Rabani, E. & Banin, U. Formation of asymmetric one-sided metal-tipped semiconductor nanocrystal dots and rods. *Nat. Mater.* **4**, 855–863 (2005).

78. Wu, K. *et al.* Hole Removal Rate Limits Photodriven H_2 Generation Efficiency in CdS-Pt and CdSe/CdS-Pt Semiconductor Nanorod–Metal Tip Heterostructures. *J. Am. Chem. Soc.* **136**, 7708–7716 (2014).
79. Lupo, M. G. *et al.* Ultrafast Electron−Hole Dynamics in Core/Shell CdSe/CdS Dot/Rod Nanocrystals. *Nano Lett.* **8**, 4582–4587 (2008).
80. Utterback, J. K. *et al.* Observation of trapped-hole diffusion on the surfaces of CdS nanorods. *Nat. Chem.* **8**, 1061–1066 (2016).
81. Grennell, A. N., Utterback, J. K., Pearce, O. M., Wilker, M. B. & Dukovic, G. Relationships between Exciton Dissociation and Slow Recombination within ZnSe/CdS and CdSe/CdS Dot-in-Rod Heterostructures. *Nano Lett.* **17**, 3764–3774 (2017).
82. Utterback, J. K., Hamby, H., Pearce, O. M., Eaves, J. D. & Dukovic, G. Trapped-Hole Diffusion in Photoexcited CdSe Nanorods. *J. Phys. Chem. C* **122**, 16974–16982 (2018).
83. Pearce, O. M., Duncan, J. S., Damrauer, N. H. & Dukovic, G. Ultrafast Hole Transfer from CdS Quantum Dots to a Water Oxidation Catalyst. *J. Phys. Chem. C* **122**, 17559–17565 (2018).
84. Tran, K. & Ulissi, Z. W. Active learning across intermetallics to guide discovery of electrocatalysts for CO_2 reduction and H_2 evolution. *Nat. Catal.* **1**, 696–703 (2018).
85. Hopkinson, M. N., Gómez-Suárez, A., Teders, M., Sahoo, B. & Glorius, F. Accelerated discovery in photocatalysis using a mechanism-based screening method. *Angew. Chemie Int. Ed.* **128**, 4434–4439 (2016).
86. Würth, C., Grabolle, M., Pauli, J., Spieles, M. & Resch-Genger, U. Relative and absolute determination of fluorescence quantum yields of transparent samples. *Nat. Protoc.* **8**, 1535–1550 (2013).
87. Morris-Cohen, A. J., Vasilenko, V., Amin, V. A., Reuter, M. G. & Weiss, E. A. Model for Adsorption of Ligands to Colloidal Quantum Dots with Concentration-Dependent Surface Structure. *ACS Nano* **6**, 557–565 (2012).
88. Uematsu, T., Shimomura, E., Torimoto, T. & Kuwabata, S. Evaluation of Surface Ligands on Semiconductor Nanoparticle Surfaces Using Electron Transfer to Redox Species. *J. Phys. Chem. C* **120**, 16012–12023 (2016).
89. Tachiya, M. Application of a generating function to reaction kinetics in micelles. Kinetics of quenching of luminescent probes in micelles. *Chem. Phys. Lett.* **33**, 289–292 (1975).
90. Ross, R. T. & Calvin, M. Thermodynamics of Light Emission and Free-Energy Storage in Photosynthesis. *Biophys. J.* **7**, 595–614 (1967).
91. Wang, Z. J., Garth, K., Ghasimi, S., Landfester, K. & Zhang, K. A. I. Conjugated Microporous Poly(Benzochalcogenadiazole)s for Photocatalytic Oxidative Coupling of Amines under Visible Light. *ChemSusChem* **8**, 3459–3464 (2015).
92. Xiao, X., Jiang, J. & Zhang, L. Selective oxidation of benzyl alcohol into benzaldehyde over semiconductors under visible light: The case of $Bi_{12}O_{17}Cl_2$ nanobelts. *Appl. Catal. B Environ.* **142**–**143**, 487–493 (2013).
93. Su, Y., Straathof, N. J. W., Hessel, V. & Noël, T. Photochemical Transformations Accelerated in Continuous-Flow Reactors: Basic Concepts and Applications. *Chem. - A Eur. J.* **20**, 10562–10589 (2014).
94. Chang, C.-C., Chen, L.-C. C. & Liu, S.-J. L. Investigation of electro-

oxidation of methanol and benzyl alcohol at boron-doped diamond electrode: evidence for the mechanism for fouling film formation. *J. Phys. Chem. B* **110**, 19426–19432 (2006).
95. Serpone, N. & Emeline, A. V. Suggested terms and definitions in photocatalysis and radiocatalysis. *Int. J. Photoenergy* **4**, 91–131 (2007).
96. Kamat, P. V., Christians, J. A. & Radich, J. G. Quantum dot solar cells: hole transfer as a limiting factor in boosting the photoconversion efficiency. *Langmuir* **30**, 5716–5725 (2014).
97. DiMeglio, J. L. & Bartlett, B. M. Interplay of corrosion and photocatalysis during nonaqueous benzylamine oxidation on cadmium sulfide. *Chem. Mater.* **29**, 7579–7586 (2017).
98. Kisch, H. & Bahnemann, D. Best Practice in Photocatalysis: Comparing Rates or Apparent Quantum Yields? *J. Phys. Chem. Lett.* **6**, 1907–1910 (2015).
99. Gomollón-Bel, F. Ten Chemical Innovations That Will Change Our World. *Chem. Int.* **41**, 1–17 (2019).
100. Baker, C. O., Huang, X., Nelson, W. & Kaner, R. B. Polyaniline nanofibers: broadening applications for conducting polymers. *Chem. Soc. Rev.* **46**, 1510–1525 (2017).
101. Jäckle, S. *et al.* Potential of PEDOT:PSS as a hole selective front contact for silicon heterojunction solar cells. *Sci. Rep.* **7**, 2170–2177 (2017).
102. Chen, K., Deng, X., Dodekatos, G. & Tüysüz, H. Photocatalytic Polymerization of 3,4-Ethylenedioxythiophene over Cesium Lead Iodide Perovskite Quantum Dots. *J. Am. Chem. Soc.* (2017).
103. Kirkwood, N. *et al.* Finding and Fixing Traps in II–VI and III–V Colloidal Quantum Dots: The Importance of Z-Type Ligand Passivation. *J. Am. Chem. Soc.* **140**, 15712–15723 (2018).
104. Trent, J. S., Scheinbeim, J. I. & Couchman, P. R. Ruthenium tetraoxide staining of polymers for electron microscopy. *Macromolecules* **16**, 589–598 (1983).
105. Kirchmeyer, S. & Reuter, K. Scientific importance, properties and growing applications of poly(3,4-ethylenedioxythiophene). *J. Mater. Chem.* **15**, 2077–2088 (2005).
106. Kuehnel, M. F. & Reisner, E. Solar Hydrogen Generation from Lignocellulose. *Angew. Chemie Int. Ed.* **57**, 3290–3296 (2018).
107. Wakerley, D. W. *et al.* Solar-driven reforming of lignocellulose to H_2 with a CdS/CdOx photocatalyst. *Nat. Energy* **2**, 17021–17030 (2017).
108. Kasap, H., Achilleos, D. S., Huang, A. & Reisner, E. Photoreforming of lignocellulose into H_2 using nano-engineered carbon nitride under benign conditions. *J. Am. Chem. Soc.* 28 (2018).
109. Uekert, T., Kuehnel, M. F., Wakerley, D. W. & Reisner, E. Plastic waste as a feedstock for solar-driven H_2 generation. *Energy Environ. Sci.* **11**, 2853–2857 (2018).
110. Uekert, T., Kasap, H. & Reisner, E. Photoreforming of Nonrecyclable Plastic Waste over a Carbon Nitride/Nickel Phosphide Catalyst. *J. Am. Chem. Soc.* **141**, 15201−15210 (2019).
111. Simon, T. *et al.* Redox shuttle mechanism enhances photocatalytic H_2 generation on Ni-decorated CdS nanorods. *Nat. Mater.* **13**, 1013–1018

(2014).
112. Ishibashi, K., Fujishima, A., Watanabe, T. & Hashimoto, K. Detection of active oxidative species in TiO_2 photocatalysis using the fluorescence technique. *Electrochem. commun.* **2**, 207–210 (2000).
113. Han, X. *et al.* Structural insight into catalytic mechanism of PET hydrolase. *Nat. Commun.* **8**, 2106–2011 (2017).
114. Habisreutinger, S. N., Schmidt-Mende, L. & Stolarczyk, J. K. Photocatalytic Reduction of CO_2 on TiO_2 and Other Semiconductors. *Angew. Chemie Int. Ed.* **52**, 7372–7408 (2013).
115. Stolarczyk, J. K., Bhattacharyya, S., Polavarapu, L. & Feldmann, J. Challenges and Prospects in Solar Water Splitting and CO_2 Reduction with Inorganic and Hybrid Nanostructures. *ACS Catal.* (2018).
116. Tollefson, J. Can the World Slow Global Warming? *Nature* **572**, 325–326 (2019).
117. Manzi, A. *et al.* Light-Induced Cation Exchange for Copper Sulfide Based CO_2 Reduction. *J. Am. Chem. Soc.* **137**, 14007–14010 (2015).
118. Wang, D. *et al.* How and Why Nanoparticle's Curvature Regulates the Apparent pK_a of the Coating Ligands. *J. Am. Chem. Soc.* **133**, 2192–2197 (2011).
119. Woehrle, G. H., Brown, L. O. & Hutchison, J. E. Thiol-Functionalized, 1.5-nm Gold Nanoparticles through Ligand Exchange Reactions: Scope and Mechanism of Ligand Exchange. *J. Am. Chem. Soc.* **127**, 2172–2183 (2005).
120. Fogg, P. G. T. *Carbon Dioxide in Non-Aqueous Solvents at Pressure less than 200 kPa*. (1992).
121. Rosen, B. A. *et al.* Ionic Liquid-Mediated Selective Conversion of CO_2 to CO at Low Overpotentials. *Science.* **334**, 643–644 (2011).
122. Dong, C. *et al.* Size-dependent activity and selectivity of carbon dioxide photocatalytic reduction over platinum nanoparticles. *Nat. Commun.* **9**, 1252–1262 (2018).
123. Ran, J., Jaroniec, M. & Qiao, S.-Z. Cocatalysts in Semiconductor-based Photocatalytic CO_2 Reduction: Achievements, Challenges, and Opportunities. *Adv. Mater.* **30**, 1704649–1704679 (2018).
124. McQuillin, F. J. *Homogeneous Hydrogenation in Organic Chemistry*. (1976).
125. Prier, C. K., Rankic, D. A. & MacMillan, D. W. C. Visible Light Photoredox Catalysis with Transition Metal Complexes: Applications in Organic Synthesis. *Chem. Rev.* **113**, 5322–5363 (2013).
126. Romero, N. A. & Nicewicz, D. A. Organic Photoredox Catalysis. *Chem. Rev.* **116**, 10075–10166 (2016).
127. Balzani, V., Bergamini, G. & Ceroni, P. Photochemistry and photocatalysis. *Rend. Lincei* (2017).
128. Magagnano, G. *et al.* Photocatalytic ATRA reaction promoted by iodo-Bodipy and sodium ascorbate. *Chem. Commun.* **53**, 1591–1594 (2017).
129. Pal, A., Ghosh, I., Sapra, S. & König, B. Quantum Dots in Visible-Light Photoredox Catalysis: Reductive Dehalogenations and C−H Arylation Reactions Using Aryl Bromides. *Chem. Mater.* **29**, 5225–5231 (2017).
130. Zhang, Z., Edme, K., Lian, S. & Weiss, E. A. Enhancing the Rate of

Quantum-Dot-Photocatalyzed Carbon−Carbon Coupling by Tuning the Composition of the Dot's Ligand Shell. *J. Am. Chem. Soc.* **139**, 4246–4249 (2017).
131. Caputo, J. A. *et al.* General and Efficient C−C Bond Forming Photoredox Catalysis with Semiconductor Quantum Dots. *J. Am. Chem. Soc.* **139**, 4250–4253 (2017).
132. Nicewicz, D. A. & MacMillan, D. W. C. Merging photoredox catalysis with organocatalysis: the direct asymmetric alkylation of aldehydes. *Science.* **322**, 77–80 (2008).
133. Lewis, N. S. Developing a scalable artificial photosynthesis technology through nanomaterials by design. *Nat. Nanotechnol.* **11**, (2016).
134. Pinaud, B. A. *et al.* Technical and economic feasibility of centralized facilities for solar hydrogen production via photocatalysis and photoelectrochemistry. *Energy Environ. Sci.* 1983–2002 (2013). doi:10.1039/c3ee40831k
135. O'Regan, B. & Grätzel, M. A low-cost, high-efficiency solar cell based on dye-sensitized colloidal TiO_2 films. *Nature* **353**, 737–740 (1991).
136. Mazzaro, R. *et al.* Uniform Functionalization of High-Quality Graphene with Platinum Nanoparticles for Electrocatalytic Water Reduction. *ChemistryOpen* **4**, 268–273 (2015).
137. Grzelczak, M., Vermant, J., Furst, E. M. & Liz-Marzá, L. M. Directed Self-Assembly of Nanoparticles. *ACS Nano* **4**, 3591–3605 (2010).
138. Cambié, D. & Noël, T. Solar Photochemistry in Flow. *Top. Curr. Chem.* **376**, 45 (2018).
139. Pieber, B., Shalom, M., Antonietti, M., Seeberger, P. H. & Gilmore, K. Heterogeneous Photocatalysis in Serial Micro-Batch Reactors. *Angew. Chemie Int. Ed.* **57**, 9976–9979 (2018).
140. Italia, V. *et al.* Laser-Inscribed Glass Microfluidic Device for Non-Mixing Flow of Miscible Solvents. *Micromachines* **10**, 23–32 (2018).
141. Ashton, P. R. *et al.* A Three-Pole Supramolecular Switch. *J. Am. Chem. Soc.* **121**, 3951–3957 (1999).
142. Niu, W.-J. *et al.* Dumbbell-shaped carbon quantum dots/AuNCs nanohybrid as an efficient ratiometric fluorescent probe for sensing cadmium (II) ions and l-ascorbic acid. *Carbon N. Y.* **96**, 1034–1042 (2016).
143. Ju, E. *et al.* Heterogeneous Assembled Nanocomplexes for Ratiometric Detection of Highly Reactive Oxygen Species in Vitro and in Vivo. *ACS Nano* **6**, 6014–6023 (2019).
144. Kodaimati, M. S. *et al.* Viewpoint: Challenges in Colloidal Photocatalysis and Some Strategies for Addressing Them. *Inorg. Chem.* **57**, 3659–3670 (2018).
145. Carbone, L. *et al.* Synthesis and Micrometer-Scale Assembly of Colloidal CdSe/CdS Nanorods Prepared by a Seeded Growth Approach. *Nano Lett.* **7**, 2942–2950 (2007).

Chapter 4 Alternative Full-Cycle Redox Reactions

4.1 Introduction

The remarkable performances obtained for combined hydrogen production and organic transformations opened the way to exploit CdSe@CdS semiconductor nanostructures for alternative redox reactions. König and Antonietti have recently proved the enormous attractiveness of such perspective by highlighting the flourishing utilisation of semiconductor materials in the field of organic synthesis[55]. Owing to the possibility to promote concerted reductive and oxidative photochemical events, semiconductors have been indeed tested for various chemo-selective radical coupling reactions, such as C-N and C-C couplings[16]. In this chapter, the versatility of CdSe@CdS-based photochemical devices was explored for photo-reductions, such as CO_2 reduction and hydrogenation reaction, photo-redox, in de-halogenation and C-C reactions, and micro heterogeneous-phase processes. In the latter part of the project, we envisioned the deployment of nanorods photosystems in microfluidic chips, with the aim of developing a scalable and working prototype of photoreactor device.

4.2 Photo-Reduction Reactions

Along with hydrogen production, photochemical research has thoroughly investigated other solar fuel forming reactions, the principal being CO_2 and N_2 reduction[114,115]. While the latter has severe performance limitations to be overcome, the former has received much attention in recent years due to the uncontrolled worldwide emission rate. From the 1.9 $Gtons$ of CO_2 emitted in 1900 to today values of 36.83 $Gtons$[116], carbon dioxide concentration skyrocketed to $> 400\ ppm$

in the atmosphere, being probably the highest in about 15 millions years[1]. Therefore, considering the energetically demanding CO_2 sequestration, carbon dioxide chemical conversion strategies are highly sought. In particular, when solar energy is deposited in C-H chemical bonds, $418.4\ kJ\ mol^{-1}$ can be stored. The possibility to store high chemical potentials with this process comes, however, at the cost of burdensome reaction conditions. CO_2 is in fact a chemically inert molecule, with closed-shell electronic configuration, that entails a multi-electronic reduction process including both C-O bond cleavage and C-H bond formation. Depending on the number of electrons involved, the following reactions can occur:

$$CO_2 + 2H^+ + 2e^- \rightarrow HCOOH \qquad E^0 = -0.61\ V$$
$$CO_2 + 2H^+ + 2e^- \rightarrow CO + H_2O \qquad E^0 = -0.53\ V$$
$$CO_2 + 4H^+ + 4e^- \rightarrow HCHO + H_2O \qquad E^0 = -0.48\ V$$
$$CO_2 + 6H^+ + 6e^- \rightarrow CH_3OH + H_2O \qquad E^0 = -0.38\ V$$
$$CO_2 + 8H^+ + 8e^- \rightarrow CH_4 + 2H_2O \qquad E^0 = -0.24\ V$$

It is possible to notice that the reduction potentials for CO, CH_3OH and CH_4 forming reactions are not prohibitively high, however such reaction pathways require proton-coupled electron transfer (PCET) mechanisms. So far, no spectroscopic evidence was ever provided for multi-electronic electron transfer, thus single electron transfer to CO_2 should necessarily be considered. Addition of one electron promotes bending of the molecule, yet the formation of the CO_2 radical anion requires $-1.90\ V\ vs\ NHE$. Almost no semiconductor provides such high thermodynamic reduction potential, comprehensively making CO_2 chemical conversion extremely difficult to tackle.

Considering that the CB edge potential of CdS lies around $-0.85\ V$ vs NHE at neutral pH[117], CdSe@CdS nanostructures necessarily require PCET mechanism to address CO_2 reduction. Initial investigation therefore assessed the potential of both Pt- and Ni-tipped SR to reduce carbon dioxide in aqueous solvent, under AM1.5G irradiation, using sacrificial hole scavengers such as N,N-Diisopropylethylamine, triethylamine or triethanolamine. No reduction products were detected, except for hydrogen, that most probably outcompetes other processes due to similar reduction potential:

$$2H^+ + 2e^- \rightarrow H_2 \qquad E^0 = -0.41\ V$$

In addition to that, we noticed extremely poor stability of the nanorods in solution, noticing formation of precipitated agglomerates within the first 30 minutes of irradiation (Figure IV-1a). Considering the partial hydration of carbon dioxide to carbonic acid, that causes pH to drop to a value ~6, we ascribed such instability to ligand shell degradation even at mild acidic pH. It was previously reported that, on one hand, the carboxylate group of mercaptoundecanoic acid (MUA) gets protonated, decreasing electrostatic stabilisation of the nanostructure because of favoured H-bonding between ligand shells[118], and, on the other hand, protonation of the thiolated heads can lead to desorption and agglomeration[119].

In light of this, we considered the possibility of using organic media to inhibit competing processes. Such strategy is also beneficial under a solubility point of view, since CO_2 at 1 atm reaches concentrations of $\sim 35\ mM$ in H_2O and of $\sim 210\ mM$ in MeOH and acetonitrile[120]. Excluding protic solvents like MeOH, that are used in common precipitation/redispersion processes with II-VI semiconductor nanostructures, we conducted further carbon dioxide conversion experiments in mixtures of toluene with acetonitrile or dimethylformamide (DMF). Surprisingly, hydrogen was again the only product detected, as can be seen in Figure 4.1B. This finding could be exclusively justified by the reduction of H^+ released after scavengers' oxidations, since water presence was avoided by the use of anhydrous solvents and inert reaction conditions. In order to reduce the selectivity towards H_2 production, two strategies were finally evaluated: firstly, the use of ionic liquid as solvent additives and, secondly, a different co-catalyst on the tip of nanorods. In the former case, ionic liquids were considered because of their capability to form complexes with CO_2 at the photoactive species surface, effectively lowering the reduction potential of the CO_2 radical anion formation[121]. In particular, 1-ethyl-3methylimidzolium tetrafluoroborate (EMIM-BF_4) was considered, yielding, however, no trace of carbon dioxide reduction products. Nevertheless, it is widely known from the electrochemistry community that more-selective co-catalyst other than Pt and Ni can be used for CO_2 reduction. In spite of recent demonstration of size-dependent selectivity of Pt-nanoparticles toward such purposes[122], Ag and Cu are generally preferred[123]. Unfortunately, synthesis of Ag- and Cu-tipped nanorods

is hampered by the cation exchange reaction occurring between Cd^{2+} and such metals[117], consequently we considered Au owing to its poor H_2 generation performances when connected to CdS@CdSe nanostructures. Figure 4.1C shows absorption and TEM data for the photoactive species used: regrettably, also Au-SR presented no CO_2 reduction activity in both aqueous, organic solvents and with multiple oxidative partners.

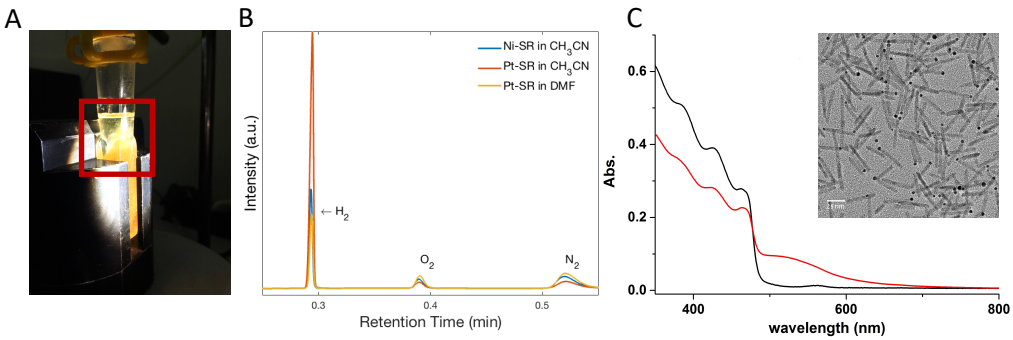

Figure 4.1. **Characterisation of CO_2 photo-reduction reactions**.
A) Precipitation of Pt-SR in acidic environment; Gas-Chromatographic traces using B) Ni-SR and Pt-SR in toluene – acetonitrile/DMF mixtures. C) Absorbance of SR (black curve) and corresponding Au-tipped nano-heterostructure (red-curve), accompanied by TEM characterisation of the latter.

The inactivity of CdSe@CdS SR towards CO_2 reduction still revealed unexpected efficient H_2 generation performance in non-aqueous media. Having observed reaction rates as high as $6\,\mu mol\,h^{-1}$, we envisioned to harvest such hydrogen flux as a reducing agent for in situ hydrogenation reactions. Current technology performing such processes employs hash experimental condition, such as high temperature and pressures, together with elaborate reactors[124]. Using light to promote local production of reducing equivalents, either in the form of H^+ or H_2, in homogeneous phase, stands therefore as a fascinating perspective. To this extent, our effort directed towards the transformation of molecules containing alkene and alkyne bonds, such as phenylacetylene, diphenylacetylene and styrene, nitro-containing compounds such as nitrobenzene and finally to BOC-protected amino-acids(Figure 4.2A). Initial investigations demonstrated excellent photostability of Pt-SR under irradiation, as shown in Figure 4.2B, however we noticed an increase in the nanorods fluorescence intensity signature. This finding, that revealed consistent throughout the whole gallery of target compounds, lead us to conjecture

detrimental electron accumulation at the metal-semiconductor interface, causing metal tip detachment and consequent increase in luminescence from bare nanorods. This, together with moderate substrate conversion, suggested the probable mismatch between H_2 available for hydrogenation at early reaction stages and substrate concentration. In light of this, we tested the effect of additional reagents to extend photostability and accumulate reducing equivalents. On one hand, proton-sources in the form of organic acids were used to supply a higher concentration of H^+ available for hydrogenation while, on the other hand, Pd/C was exploited to trap H_2 molecules formed and consequently create dense reducing reaction sites. Unfortunately, both strategies did not result in appreciable substrate conversion improvement, with only trace amount of stilbene found when diphenylacetylene was reduced using DMF as proton-source. Nevertheless, we still speculate that further extension of the current reaction conditions screened can improve conversion yields.

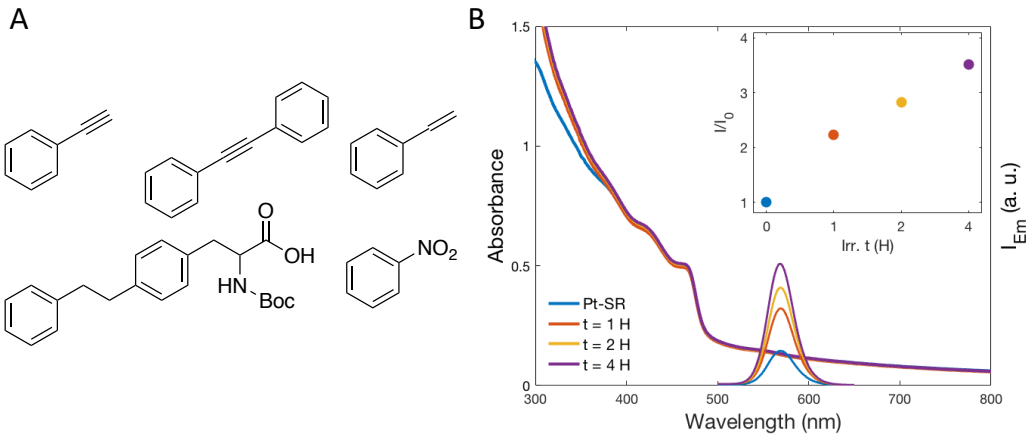

Figure 4.2. **Photo-hydrogenation reactions**.
A) Gallery of substrates screened (from top left, moving clockwise): phenylacetylene, diphenylacetylene, styrene, nitrobenzene and 3-(4-(benzyloxy)phenyl)-2-((*tert*-butoxycarbonyl)amino)propanoic acid. B) Absorption and fluorescence emission spectroscopy data for the hydrogenation of phenylacetylene.

4.3 Photo-Redox Reactions

Light-promoted mechanisms profoundly influenced many branches of chemical research. Among these, organic synthesis is probably the field that was most affected with the advent of photo-redox catalysis[125,126]. This approach allows to generate radical intermediates upon visible light excitation in mild and ecologically benign experimental conditions. The ability to perform single-electron transfer processes ensue form the creation of photo-induced excited states, that are potent reductant and oxidant reagents compared to their ground-state counterparts[127].

Semiconductor materials have, within this framework, been successfully employed in the promotion of numerous radical reactions. The heterogeneity of bulk structures can, however, impose limitations to the chemical selectivity and retard activity, yet the homogeneity of CdSe@CdS nanostructures could offer considerable advantages to mitigate such hindrance. As a result, we addressed the synthetically important carbon-halogen activation as testbed for the photocatalytic activity of hybrid nanostructured semiconductors. In particular, Pt-SR were considered for dehalogenation reactions and C-H arylations using hetero aryl halides.

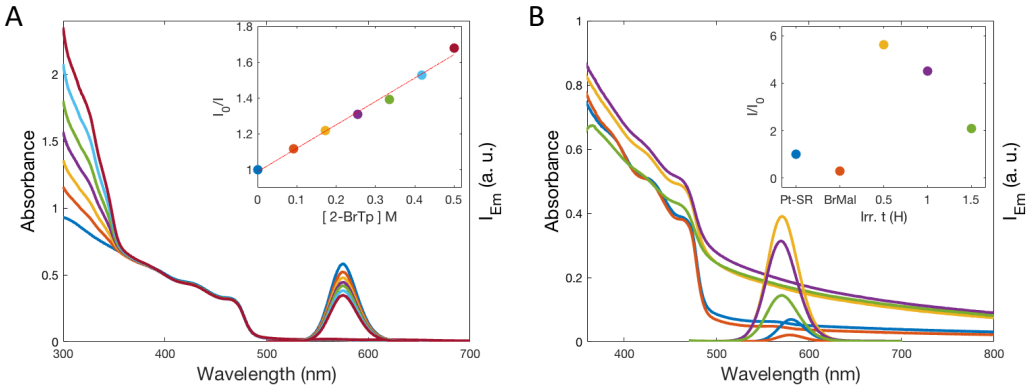

Figure 4.3. **Spectrophotometric analyses of photo-redox reactions using CdSe@CdS SR**.

A) Stern-Volmer analysis of 2-bromothiophene and CdSe@CdS SR in toluene and B) absorption and emission spectra for the dehalogenative reaction of diethyl 2-bromo-malonate using Pt-SR (10^{-8} M) in toluene under 450nm irradiation.

Figure 4.3 present a typical Stern-Volmer analysis that was conducted for various bromoarenes, showing linear dependence as a function a substrate concentration using toluene as a solvent. The quenching kinetics revealed sluggish, the highest being recorded for 2-bromothiophene, which showed a $k_q = 7.46 \cdot$

$10^7 M^{-1}s^{-1}$, meaning that a concentration of $0.766\ M$ is required to quench half of the excited-state population (with $\tau_0 = 17.5\ ns$).

Furthermore, when tested under 455 nm irradiation, using various sacrificial reagents to harvest photo-generated holes, Pt-SR showed poor photostability within the first hours of reaction, as shown in Figure 4.3B. Considering for example the de-halogenation of 2-bromothiophene, we speculated that the intermediate radical cation generated can act as poisoning agent if not properly trapped by hydrogen atom donors or by suitable reagents achieving C-C bond forming reactions. The former strategy was addressed by including various proton sources in solution, however the photocatalyst did not show improved stability. Accordingly, we introduced trapping reagents like alkenes to effectively promote atom-transfer radical additions[128]. This solution did not yield successful results, however, in the same months, Pal, König et al. demonstrated an effective way to trap heteroaryl radicals produced by ZnSe@CdS QDs using pyrroles[129]. Parallelly, the Weiss and Weix groups demonstrated, respectively, C-C coupling[130] and α-alkylation, β-amino alkylation, dehalogenation, amine arylation and decarboxylative radical formation using CdSe QDs[131], demonstrating the suitability of semiconductor nanostructures to photo-redox applications.

Finally, Ni-SR were considered as alternative candidates for sp_2-sp_3 cross couplings reaction developed by MacMillan[132]. The hybrid nanostructure used in this work is expected to integrate both the function of photo-redox and organo-catalytic components, owing to the close proximity of Ni nanoparticles, i.e. the reactive centre generating alkyl radicals, and the radical cations obtained from oxidative reactions occurring at the nanorods surface. To this extent, initial fluorescence quenching spectroscopic investigation revealed high affinity between NRs and 4-Bromo-acetophenone and N-Boc-Prolyne, that showed quenching of 37% and 42% of the initial a fluorescence, respectively at 0.05 M substrate concentration. Characterisation and optimization of such reaction is under development in our laboratory.

4.4 Proof-of-concept Photochemical Devices

A fundamental deliverable of the present work has been dedicated to developing a proof-of-concept practical implementation of photochemical systems in real-world devices. A major obstacle preventing direct solar-to-chemical energy conversion systems to "see the light of day" is widely recognised as being the realisation of simple and cheap devices[133]. Currently, artificial devices entailing photo-electrochemical cells or plastic 'baggie' systems containing a slurry of photoactive particles are designated as the most promising solution to implement such technology to industrial scale[134].

To this extent, colloidal nanostructures have been widely used in the realisation of sensitised photocathodes since the pioneering discovery by Grätzel[135]. Such device architecture was especially designed to promote photoinduced charge separation and extraction, yet inefficient electron and hole transfer dynamics still represent the main efficiency bottleneck. Being a fundamental limitation also for CdSe@CdS systems[78,96], we proposed to integrate colloidal nanorods on conductive solid substrates to improve hole extraction. To this extent, along with the effort to upgrade photo-generated hole utilisation via oxidative chemistries, our strategy foresaw, on one hand, the creation of a heterogeneous photoelectrochemical cell, and, on the other hand, the exploitation of microfluidic chip as photoreactors.

Firstly, owing to the expertise previously developed in our research group, graphene was considered as a platform to support Pt-SR for photo-electrochemical purposes. Mazzaro, Bergamini et al. indeed demonstrated that high-quality exfoliated graphene could host monodispersed Pt-nanoparticles to promote electrocatalytic H_2 production with a turnover frequency of ~ 46000 at zero overpotential[136]. Initially, deposition of Pt-SR on graphene was performed via spin-coating (Figure 4.4A), which revealed ineffective in generating photocurrent when the device was tested in a single compartment cell in a phosphate buffer solution at pH 7.2. We speculated that, even when a single monolayer of NRs could be assembled, short-circuit between holes extracted by graphene and electron

accumulated in the Pt tip will occur as long as the NRs are horizontally oriented on the substrate. As a consequence, vertically oriented assembly of Pt-SR was pursued in order to access the multitude of periodicity-dependent properties typically offered by self-assembled nano-systems[137]. Figure 4.4B shows that, using solvent drying-mediated self-assembly, it is possible to increase the spectrophotometric response of deposited Pt-SR when these are irradiated with 455 nm light during assembly. In fact, it was intended to exploit the electrostatic driving force of photo-generated charge carriers, via dipole-dipole interactions, as a driving force to vertically align nanorods during solvent evaporation. This strategy has been previously been proposed together with other field- or template-directed assembly, however it did not yield noticeable results in terms of photoelectrochemical performance.

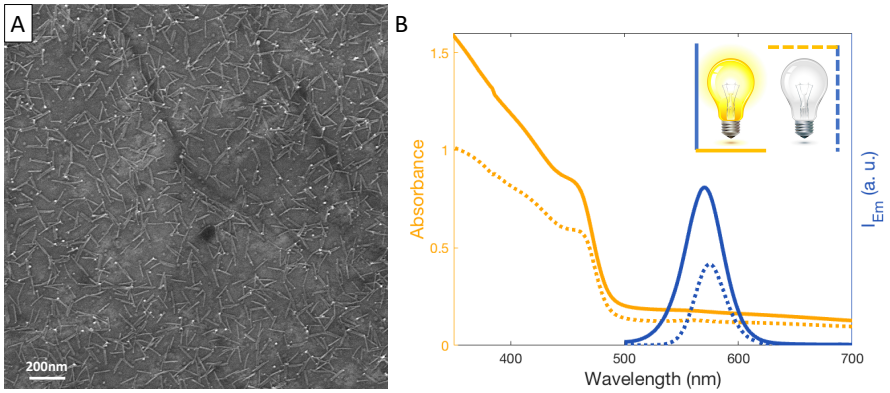

Figure 4.4. **Integration of Pt-SR on exfoliated graphene**.
A) TEM image of spin-coated Pt-SR. B) Absorbance (left-hand side, orange curve) and fluorescence emission (right-hand side, blue curve) of the self-assembled monolayer after drying-mediated deposition, with and without the use of 455 nm light during solvent evaporation.

Secondly, development of a functional photochemical device that could ensure efficient scale-up and scale-out deployment was envisioned via the utilisation of microfluidic chips. These devices, that are principally employed in the biological field, offer considerable advantages for chemical processing, a few being increased mass and heat transfer, improved control on reaction parameters like temperature and residence time and finally small and thus safe reagents volumes used in reaction optimisation. Notably, the superior performances of flow conditions in photochemical processes have been widely proved by recent works from Noel group and others[93,138,139]. In their reports it was demonstrated, for example, the

possibility to both reduce synthesis time from hours to minutes and also promote chemistries inaccessible in batch conditions.

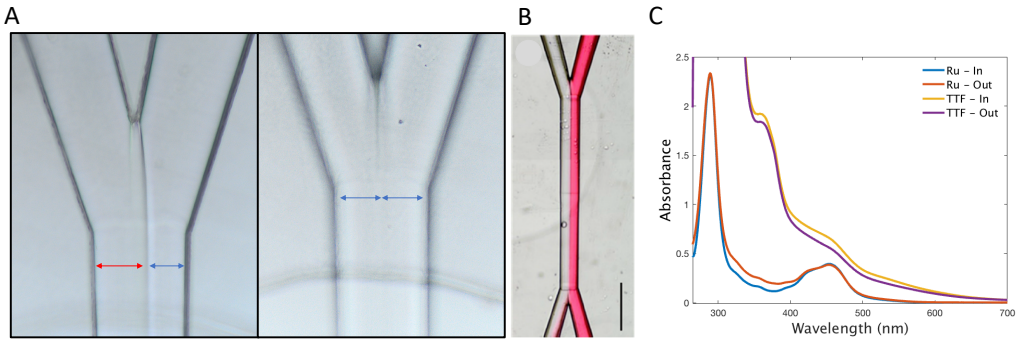

Figure 4.5. **Photochemical reactions in microfluidic chips**.
A) Optimisation of liquid-liquid interface between tangential streams of ethanol solvent via pressure tuning; B) Y-shaped microfluidic chip (500um scale bar); C) Absorbance data for input and output samples for the reaction between $Ru(bpy)_3^{2+}$ and TTF in a Y-shaped chip.

In the pursuit to design an artificial photochemical reactor allowing efficient promotion of the light-triggered reactions described in the present thesis, devices entailing tangential microfluidic channels were especially considered. In such configuration, light-active species and quenchers can be separated in different compartments, confining possible interaction only to the interfacial region between the contacting laminar fluids. Upon successful electron-transfer at the interface, not only decreased back-electron transfer and parasitic reaction, but also clean recycling of the photocatalyst can be envisioned thanks to rapid reactants escape out of the solvent cage created at the interface itself.

Motivated by the great potential provided by microfluidic devices, we started our investigation by performing a known photochemical reaction in a two-channel chip featuring parallel tangential flows of adjacent solvents. As can be seen in Figure 4.5A, by careful optimisation of flow pressures in the different channels, it is possible to prevent solvent mixing, both by using different or identical solvents in the two channels. Italia, Criante et al. indeed demonstrated that Rhodmine-6G is completely confined in one of the two streams when both channels where flushed with ethanol (Figure 4.5B)[140]. Provided such peculiar properties of Y-shaped microfluidic chips, we proposed to perform photochemical reactions by separating

photocatalyst and quencher species in different channels, according to the following scheme:

- Light absorption by photocatalyst and photo-induced electron-transfer to quencher species across the liquid-liquid interface;
- Fragmentation of donor/acceptor quencher species and concomitant regeneration of the photocatalyst by acceptor/donor species;
- Collection of reaction products and regenerated photocatalyst.

Figure 4.5C presents the spectrophotometric characterisation of input and output samples for the photochemical oxidation of tetrathiafulvalene (TTF) by Ruthenium tris-bipyridine ($Ru(bpy)_3^{2+}$) when carried out in a Y-shaped silica microfluidic chip, according to the formula:

$$Ru(bpy)_3^{2+} \xrightarrow{h\nu} [Ru(bpy)_3^{2+}]^*$$
$$[Ru(bpy)_3^{2+}]^* + TTF \leftrightarrow Ru(bpy)_3^{+} + TTF^{+}$$

Despite the absence of cross-mixing between the distinct flow streams, no spectral evidence of TTF^+ could be inferred from the output solution, as this product has a distinguishable red-shifted shoulder compared to the non-oxidised counterpart[141]. The unsuccessful experiment still served us to verify the possibility to carry out photochemical reactions in non-mixing tangential fluids, with relevant results expected to be obtained after optimisation of residence time and reagent's concentrations.

A more interesting scenario involves in fact the transition of the redox chemistries described in chapter 3 to a microfluidic configuration as schematically envisaged in Figure 4.6A. In such system 3-adjacent channels should promote photoinduced electron transfer from the photoactive species, present in the central stream, to donor and acceptor moieties, separated into two different side channels. The so-created radical anion and cation intermediates are then expected to interact with co-catalysts nanoparticles designed to activate reduction and oxidation half-reactions, respectively. Accomplishment of such elaborate photochemical reactor was initiated with the simpler microfluidic device configuration featuring a single straight channel. In Figure 4.6B a polydimethylsiloxane (PDMS) device entailing a channel of such shape has been functionalised with CdSe@CdS nanorods.

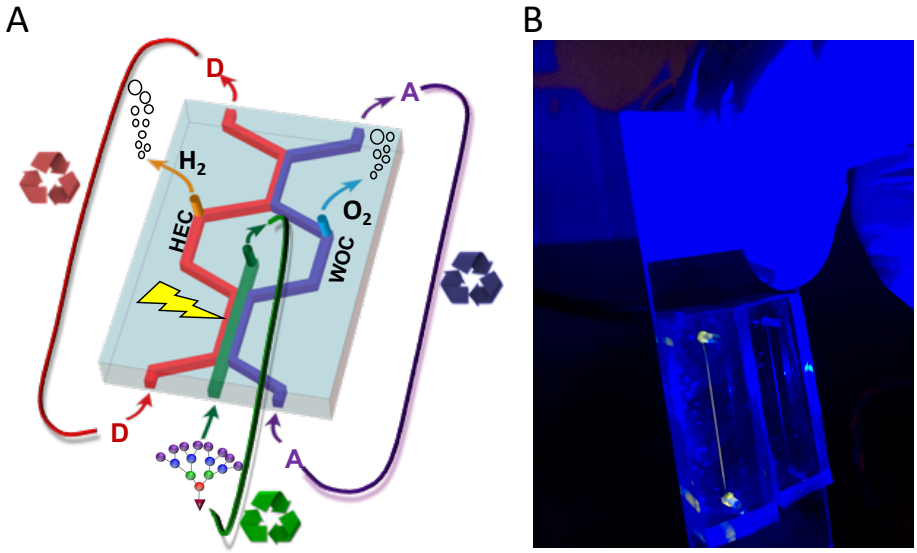

Figure 4.6. **Microfluidic chip based photochemical reactor**.
A) Schematic illustration of the 3 adjacent channels configuration designed to separate photocatalysts, Hydrogen Evolution Catalyst and Water Oxidation Catalyst in different reaction environment. B) Linear-shaped channel engraved in polydimethylsiloxane functionalised with CdSe@CdS nanorods.

Initially, leveraging on hydrophobic-hydrophilic repulsion, we injected octadecylphosphine-capped SR in the channel, followed by thorough washing with water, which resulted in the percolation of nanorods in the porous PDMS structure. This strategy would however allow photochemical activity only in organic solvents, thus mercaptoundecanoic-capped (MUA) SR should be used for this purpose. To this extent, we aimed to achieve a chemical functionalisation of the channel walls, effectively producing a high-absorbing thin film at the reactor surface. This strategy, provided robust NRs photostability, could yield reaction turnovers only limited by flow conditions. In this case, we proposed to form amide bonds between the carboxylic acid of MUA ligand and the amine group provided by (3-Aminopropyl)triethoxysilane (APTES). This solution has been previously reported via NHS-EDC coupling with Au-nanoparticles for fluorescent labelling purposes and is currently under development in our laboratories[142,143]. Alternatively, a strategy entailing MUA ligand displacement by (3-mercaptopropyl)trimethoxysilane (MPTES) will be pursued in order to achieve a closer binding between the NRs and channel walls via thiol-Cd^{2+} interaction from MPTES and NRs.

4.5 Summary

Together with fuel-forming reactions, organic synthesis represents a key perspective for any versatile photochemical device. This chapter devoted therefore to the exploitation of CdSe@CdS (SR) to the latter scenario, where demonstration for such material class are still missing. Seminal contribution for semiconductor nanostructured-based synthesis were, on the other hand, reported for similar systems by the Weiss, Weix and Soo research group[33,131,144]. To this extent, we speculated that the superior quantum efficiency performances provided by Pt-SR could be harvested to promote similar bond-breaking and bond-making reaction. Concerted electron-transfer processes characteristic of semiconductor systems offer, in this regards, peculiar reaction pathways for chemo-selective syntheses.

Firstly, we investigated the crucially important carbon dioxide reduction reaction.

Owing to the demanding thermodynamic and kinetic requirements, CO_2 activation was outcompeted by selectivity of both Pt-, Ni- and Au-SR towards H_2 generation. We found inefficient any strategy to hinder H^+ reduction, either by using coordinating additives like ionic liquids or aprotic environment provided by organic solvent. Surprisingly, H_2 selectivity prevailed also in this latter condition, that we took advantage of by designing in-situ hydrogenation reactions. Initial findings relating to such widely investigated process offers an attractive perspective for Pt-SR to promote it via light-triggered mechanism.

Later, mutual organic synthesis was directly targeted by considering de-halogenation and C-C coupling reactions. In this case, the nanometric spacing between the red-ox active sites of the nanostructure allows for realistic opportunities to promote radical coupling type-B mechanisms. In the same way, unsuccessful trapping of the radical intermediates created can cause photocatalyst

poisoning, which we speculate to currently limit our tentative hetero aryl dehalogenations.

Finally, a conclusive transition of the photochemical reactions promoted by hybrid SR to a real-photoreactor was encompassed by exploitation of microfluidic chips. Such devices imply the use of flow conditions, which were expected to be beneficial to solve the issues encountered in Chapter 3, but also eventually access CdSe@CdS systems to novel chemistries. Notably, we observed the possibility to infiltrate our SR in the pores of PDMS chips by physical method. In sight of the need to guarantee full recyclability of the catalyst during aqueous based reactions, chemical functionalisation of MUA-capped SR on the channels walls is currently under development to realise a proof-of-concept robust photosystem with wide application outlooks.

References

1. Pearson, P. N. & Palmer, M. R. Atmospheric carbon dioxide concentrations over the past 60 million years. *Nature* **406**, 695–699 (2000).
2. Sapart, C. J. *et al.* Natural and anthropogenic variations in methane sources during the past two millennia. *Nature* **490**, 85–88 (2012).
3. Cook, J. *et al.* Consensus on consensus: a synthesis of consensus estimates on human-caused global warming. *Environ. Res. Lett.* **11**, 1–7 (2016).
4. *World Energy Outlook 2018*. *International Energy Agency Publications* (2018).
5. Lewis, N. S. & Nocera, D. G. Powering the planet: Chemical challenges in solar energy utilization. *Proc. Natl. Acad. Sci.* **103**, 15729–15735 (2006).
6. Tachibana, Y., Vayssieres, L. & Durrant, J. R. Artificial photosynthesis for solar water-splitting. *Nat. Photonics* **6**, 511–518 (2012).
7. Kornienko, N., Zhang, J. Z., Sakimoto, K. K., Yang, P. & Reisner, E. Interfacing nature's catalytic machinery with synthetic materials for semi-artificial photosynthesis. *Nat. Nanotechnol.* **13**, 890–899 (2018).
8. United States Department of Energy. *DOE Technical Targets for Hydrogen Production from Photoelectrochemical Water Splitting*. (2011).
9. Japanese Ministerial Council on Renewable Energy - Hydrogen and Related Issues. *Basic Hydrogen Strategy*. (2017).
10. Jang, J.-W. *et al.* Toward practical solar hydrogen production-an artificial photosynthetic leaf-to-farm challenge. *Chem. Soc. Rev.* **48**, 1908–1971 (2019).
11. Goto, Y. *et al.* A Particulate Photocatalyst Water-Splitting Panel for Large-Scale Solar Hydrogen Generation. *Joule* **2**, 509–520 (2018).
12. Hisatomi, T. & Domen, K. Reaction systems for solar hydrogen production via water splitting with particulate semiconductor photocatalysts. *Nat. Catal.* **2**, 387–399 (2019).
13. Fabian, D. M. *et al.* Particle suspension reactors and materials for solar-driven water splitting. *Energy Environ. Sci.* **8**, 2825–2850 (2015).
14. Ciamician, G. The photochemistry of the future. *Science.* **36**, 385–394 (1912).
15. Verhoeven, J. W. Glossary of Terms used in Photochemistry. *Pure Appled Chem.* **68**, 2223–2286 (1996).
16. Kisch, H. *Semiconductor Photocatalysis*. (2014).
17. Barber, J. Biological solar energy. *Philos. Trans. Math. Phys. Eng. Sci.* **365**, 1007–1023 (2007).
18. Böer, K. W. The solar spectrum at typical clear weather days. *Sol. Energy* **19**, 525–538 (1977).
19. Blankenship, R. E. *et al.* Comparing Photosynthetic and Photovoltaic Efficiencies and Recognizing the Potential for Improvement. *Science.* **332**, 805–809 (2011).
20. Bolton, J. R. & Hall, D. O. Conversion and Storage. *Annu. Rev. Energy* **4**, 353–401 (1979).
21. Ross, R. T. & Hsiao, T.-L. Limits on the yield of photochemical solar energy conversion. *J. Appl. Phys.* **48**, 4783–4785 (1977).

22. Bolton, J. R. Solar Fuels : The production of energy-rich compounds by the photochemical conversion and storage of solar energy. *Science.* **202**, 705–711 (1978).
23. Bolton, J. R., Haught, A. F. & Ross, R. T. Photochemical Energy Storage: An Analysis of Limits. in *Photochemical Conversion and Storage of Solar Energy* 297–346 (1981).
24. Bolton, J. R., Strickler, S. J. & Connolly, J. S. Limiting and realizable efficiencies of solar photolysis of water. *Nature* **316**, 495–500 (1985).
25. Archer, M. D. & Bolton, J. R. Requirements for Ideal Performance of Photochemical and Photovoltaic Solar Energy Converters. *J. Phys. Chem.* **94**, 8028–8036 (1990).
26. Shockley, W. & Queisser, H. J. Detailed Balance Limit of Efficiency of p-n Junction Solar Cells. *J. Appl. Phys.* **32**, 510–519 (1961).
27. Baierlein, R. The elusive chemical potential. *Am. J. Phys.* **69**, 423–434 (2001).
28. McConnell, I., Li, G. & Brudvig, G. W. Energy Conversion in Natural and Artificial Photosynthesis. *Chem. Biol.* **17**, 434–447 (2010).
29. Fujishima, A. & Honda, K. Electrochemical Photolysis of Water at a Semiconductor Electrode. *Nature* **238**, 37–38 (1972).
30. Kirch, M., Lehn, J.-M. & Sauvage, J.-P. Hydrogen Generation by Visible Light Irradiation of Aqueous Solutions of Metal Complexes. An approach to the photochemical conversion and storage of solar energy. *Helv. Chim. Acta* **62**, 1345–1384 (1979).
31. Bard, A. J. Photoelectrochemistry and heterogeneous photo-catalysis at semiconductors. *J. Photochem.* **10**, 59–75 (1979).
32. Grätzel, M. Artificial Photosynthesis: Water Cleavage into Hydrogen and Oxygen by Visible Light. *Acc. Chem. Res.* **14**, 376–384 (1981).
33. Đokicá, M. & Soo, H. Sen. Artificial photosynthesis by light absorption, charge separation, and multielectron catalysis. *Chem. Commun.* **54**, 6554–6572 (2018).
34. Serpone, N. *et al.* Why do Hydrogen and Oxygen Yields from Semiconductor-Based Photocatalyzed Water Splitting Remain Disappointingly Low? Intrinsic and Extrinsic Factors Impacting Surface Redox Reactions. *ACS Energy Lett.* **1**, 931–948 (2016).
35. Madelung, O. II-VI compounds. in *Semiconductors: Data Handbook* 173–244 (2004).
36. Steigerwald, M., Bawendi, M. G., Steigerwald, M. L. & Brus, L. E. The Quantum Mechanics of Larger Semiconductor Clusters. *Annu. Rev. Phys. Chem.* **41**, 477–96 (2003).
37. Yang, W. *et al.* Electron Accumulation Induces Efficiency Bottleneck for Hydrogen Production in Carbon Nitride Photocatalysts. *J. Am. Chem. Soc.* **141**, 11219–11229 (2019).
38. Edvinsson, T. Optical quantum confinement and photocatalytic properties in two-, one-and zero-dimensional nanostructures. *R. Soc. Open Sci.* **5**, 180387–180403 (2018).
39. Li, X., Yu, J. & Jaroniec, M. Hierarchical photocatalysts. *Chem. Soc. Rev.* **45**, 2603–2636 (2016).
40. Kovalenko, M. V. *et al.* Prospects of Nanoscience with Nanocrystals. *ACS*

Nano **9**, 1012–1057 (2015).
41. Wu, K. & Lian, T. Quantum confined colloidal nanorod heterostructures for solar-to-fuel conversion. *Chem. Soc. Rev.* **45**, 3759–4034 (2016).
42. Alivisatos, A. P. Perspectives on the Physical Chemistry of Semiconductor Nanocrystals. *J. Phys. Chem.* **100**, 13226–13239 (1996).
43. Murray, C. B., Norris, D. J. & Bawendi, M. G. Synthesis and Characterization of Nearly Monodisperse CdE (E = S, Se, Te) Semiconductor Nanocrystallites. *J. Am. Chem. Soc* **115**, 8706–8715 (1993).
44. Weiss, E. A. Designing the surfaces of semiconductor quantum dots for colloidal photocatalysis. *ACS Energy Lett.* **2**, 1005–1013 (2017).
45. Amirav, L. & Alivisatos, A. P. Photocatalytic Hydrogen Production with Tunable Nanorod Heterostructures. *J. Phys. Chem. Lett* **1**, 1051–1054 (2010).
46. Peng, X. *et al.* Shape control of CdSe nanocrystals. *Nature* **404**, 3408–3413 (2000).
47. Mokari, T., Rothenberg, E., Popov, I., Costi, R. & Banin, U. Selective Growth of Metal Tips onto Semiconductor Quantum Rods and Tetrapods. *Science.* **304**, (2004).
48. Habas, S. E., Yang, P. & Mokari, T. Selective Growth of Metal and Binary Metal Tips on CdS Nanorods. *J. Am. Chem. Soc.* **130**, 3294–3295 (2008).
49. Talapin, D. V. *et al.* Seeded Growth of Highly Luminescent CdSe/CdS Nanoheterostructures with Rod and Tetrapod Morphologies. *Nano Lett.* **7**, 2951–2959 (2007).
50. Amirav, L. & Alivisatos, A. P. Luminescence Studies of Individual Quantum Dot Photocatalysts. *J. Am. Chem. Soc.* **135**, 13049–13053 (2013).
51. Kalisman, P., Nakibli, Y. & Amirav, L. Perfect photon-to-hydrogen conversion efficiency. *Nano Lett.* **16**, 1776–1781 (2016).
52. Amirav, L., Oba, F., Aloni, S. & Alivisatos, A. P. Modular Synthesis of a Dual Metal-Dual Semiconductor Nano-Heterostructure. *Angew. Chemie Int. Ed.* **54**, 7007–7011 (2015).
53. Serpone, N. *et al.* Standardization protocol of process efficiencies and activation parameters in heterogeneous photocatalysis: Relative photonic efficiencies ζr. *J. Photochem. Photobiol. A Chem.* **94**, 191–203 (1996).
54. Kisch, H. Semiconductor photocatalysis for chemoselective radical coupling reactions. *Acc. Chem. Res.* **50**, 1002–1010 (2017).
55. Ghosh, I. *et al.* Organic semiconductor photocatalyst can bifunctionalize arenes and heteroarenes. *Science.* **365**, 360–366 (2019).
56. Kisch, H. On the Problem of Comparing Rates or Apparent Quantum Yields in Heterogeneous Photocatalysis. *Angew. Chemie Int. Ed.* **49**, 9588–9589 (2010).
57. Qureshi, M. & Takanabe, K. Insights on Measuring and Reporting Heterogeneous Photocatalysis: Efficiency Definitions and Setup Examples. *Chem. Mater.* **29**, 158–167 (2017).
58. Kunz, L. Y. *et al.* Artificial inflation of apparent photocatalytic activity induced by catalyst-mass-normalization and a method to fairly compare heterojunction systems. *Energy Environ. Sci.* **12**, 1657–1667 (2019).
59. Osterloh, F. E. Photocatalysis versus Photosynthesis: A Sensitivity Analysis of Devices for Solar Energy Conversion and Chemical

Transformations. *ACS Energy Lett.* **2**, 445–453 (2017).
60. Coontz, R. *et al.* Toward a Hydrogen Economy. *Science.* **305**, 957–976 (2004).
61. Tang, J., Durrant, J. R. & Klug, D. R. Mechanism of photocatalytic water splitting in TiO_2. Reaction of water with photoholes, importance of charge carrier dynamics, and evidence for four-hole chemistry. *J. Am. Chem. Soc.* **130**, 13885–13891 (2008).
62. Wolff, C. *et al.* All-in-one visible-light-driven water splitting by combining nanoparticulate and molecular co-catalysts on CdS nanorods. *Nat. Energy* **3**, 862–869 (2018).
63. You, B., Han, G. & Sun, Y. Electrocatalytic and photocatalytic hydrogen evolution integrated with organic oxidation. *Chem. Commun.* **54**, 5943–5955 (2018).
64. Nakibli, Y. & Amirav, L. Selective Growth of Ni Tips on Nanorod Photocatalysts. *Chem. Mater.* **28**, 4524–4527 (2016).
65. Norris, D. J., Sacra, A., Murray, C. B. & Bawendi, M. G. Measurement of the size dependent hole spectrum in CdSe quantum dots. *Phys. Rev. Lett.* **72**, 2612–2615 (1994).
66. Ekimov, A. I. *et al.* Absorption and intensity-dependent photoluminescence measurements on CdSe quantum dots: assignment of the first electronic transitions. *J. Opt. Soc. Am. B* **10**, 100–107 (1993).
67. Hoang, T. B. *et al.* Temperature dependent photoluminescence of single CdS nanowires. *Appl. Phys. Lett.* **89**, 1231231–1231233 (2006).
68. Puthussery, J., Lan, A., Kosel, T. H. & Kuno, M. Band-Filling of Solution-Synthesized CdS Nanowires. *ACS Nano* **2**, 357–367 (2008).
69. Shabaev, A. & Efros, A. L. 1D Exciton Spectroscopy of Semiconductor Nanorods. *Nano Lett.* **4**, 1821–1825 (2004).
70. Sitt, A., Sala, F. Della, Menagen, G. & Banin, U. Multiexciton Engineering in Seeded Core/Shell Nanorods: Transfer from Type-I to Quasi-type-II Regimes. *Nano Lett.* **9**, 3470–3476 (2009).
71. Rainò, G. *et al.* Probing the Wave Function Delocalization in CdSe/CdS Dot-in-Rod Nanocrystals by Time- and Temperature-Resolved Spectroscopy. *ACS Nano* **5**, 4031–4036 (2011).
72. Smith, E. R., Luther, J. M. & Johnson, J. C. Ultrafast Electronic Delocalization in CdSe/CdS Quantum Rod Heterostructures. *Nano Lett.* **11**, 4923–4931 (2011).
73. Wu, K. *et al.* Universal Length Dependence of Rod-to-Seed Exciton Localization Efficiency in Type I and Quasi-Type II CdSe@CdS Nanorods. *ACS Nano* **9**, 4591–4599 (2015).
74. Christodoulou, S. *et al.* Band structure engineering via piezoelectric fields in strained anisotropic CdSe/CdS nanocrystals. *Nat. Commun.* **6**, 7905–7912 (2015).
75. Lakowicz, J. R. *Principles of Fluorescence Spectroscopy*. (2006).
76. Tarafder, K., Surendranath, Y., Olshansky, J. H., Alivisatos, A. P. & Wang, L.-W. Hole Transfer Dynamics from a CdSe/CdS Quantum Rod to a Tethered Ferrocene Derivative. *J. Am. Chem. Soc.* **136**, 5121–5131 (2014).
77. Mokari, T., Sztrum, C. G., Salant, A., Rabani, E. & Banin, U. Formation of asymmetric one-sided metal-tipped semiconductor nanocrystal dots and

rods. *Nat. Mater.* **4**, 855–863 (2005).
78. Wu, K. *et al.* Hole Removal Rate Limits Photodriven H $_2$ Generation Efficiency in CdS-Pt and CdSe/CdS-Pt Semiconductor Nanorod–Metal Tip Heterostructures. *J. Am. Chem. Soc.* **136**, 7708–7716 (2014).
79. Lupo, M. G. *et al.* Ultrafast Electron−Hole Dynamics in Core/Shell CdSe/CdS Dot/Rod Nanocrystals. *Nano Lett.* **8**, 4582–4587 (2008).
80. Utterback, J. K. *et al.* Observation of trapped-hole diffusion on the surfaces of CdS nanorods. *Nat. Chem.* **8**, 1061–1066 (2016).
81. Grennell, A. N., Utterback, J. K., Pearce, O. M., Wilker, M. B. & Dukovic, G. Relationships between Exciton Dissociation and Slow Recombination within ZnSe/CdS and CdSe/CdS Dot-in-Rod Heterostructures. *Nano Lett.* **17**, 3764–3774 (2017).
82. Utterback, J. K., Hamby, H., Pearce, O. M., Eaves, J. D. & Dukovic, G. Trapped-Hole Diffusion in Photoexcited CdSe Nanorods. *J. Phys. Chem. C* **122**, 16974–16982 (2018).
83. Pearce, O. M., Duncan, J. S., Damrauer, N. H. & Dukovic, G. Ultrafast Hole Transfer from CdS Quantum Dots to a Water Oxidation Catalyst. *J. Phys. Chem. C* **122**, 17559–17565 (2018).
84. Tran, K. & Ulissi, Z. W. Active learning across intermetallics to guide discovery of electrocatalysts for CO_2 reduction and H_2 evolution. *Nat. Catal.* **1**, 696–703 (2018).
85. Hopkinson, M. N., Gómez-Suárez, A., Teders, M., Sahoo, B. & Glorius, F. Accelerated discovery in photocatalysis using a mechanism-based screening method. *Angew. Chemie Int. Ed.* **128**, 4434–4439 (2016).
86. Würth, C., Grabolle, M., Pauli, J., Spieles, M. & Resch-Genger, U. Relative and absolute determination of fluorescence quantum yields of transparent samples. *Nat. Protoc.* **8**, 1535–1550 (2013).
87. Morris-Cohen, A. J., Vasilenko, V., Amin, V. A., Reuter, M. G. & Weiss, E. A. Model for Adsorption of Ligands to Colloidal Quantum Dots with Concentration-Dependent Surface Structure. *ACS Nano* **6**, 557–565 (2012).
88. Uematsu, T., Shimomura, E., Torimoto, T. & Kuwabata, S. Evaluation of Surface Ligands on Semiconductor Nanoparticle Surfaces Using Electron Transfer to Redox Species. *J. Phys. Chem. C* **120**, 16012–12023 (2016).
89. Tachiya, M. Application of a generating function to reaction kinetics in micelles. Kinetics of quenching of luminescent probes in micelles. *Chem. Phys. Lett.* **33**, 289–292 (1975).
90. Ross, R. T. & Calvin, M. Thermodynamics of Light Emission and Free-Energy Storage in Photosynthesis. *Biophys. J.* **7**, 595–614 (1967).
91. Wang, Z. J., Garth, K., Ghasimi, S., Landfester, K. & Zhang, K. A. I. Conjugated Microporous Poly(Benzochalcogenadiazole)s for Photocatalytic Oxidative Coupling of Amines under Visible Light. *ChemSusChem* **8**, 3459–3464 (2015).
92. Xiao, X., Jiang, J. & Zhang, L. Selective oxidation of benzyl alcohol into benzaldehyde over semiconductors under visible light: The case of $Bi_{12}O_{17}Cl_2$ nanobelts. *Appl. Catal. B Environ.* **142**–**143**, 487–493 (2013).
93. Su, Y., Straathof, N. J. W., Hessel, V. & Noël, T. Photochemical Transformations Accelerated in Continuous-Flow Reactors: Basic Concepts and Applications. *Chem. - A Eur. J.* **20**, 10562–10589 (2014).

94. Chang, C.-C., Chen, L.-C. C. & Liu, S.-J. L. Investigation of electro-oxidation of methanol and benzyl alcohol at boron-doped diamond electrode: evidence for the mechanism for fouling film formation. *J. Phys. Chem. B* **110**, 19426–19432 (2006).
95. Serpone, N. & Emeline, A. V. Suggested terms and definitions in photocatalysis and radiocatalysis. *Int. J. Photoenergy* **4**, 91–131 (2007).
96. Kamat, P. V., Christians, J. A. & Radich, J. G. Quantum dot solar cells: hole transfer as a limiting factor in boosting the photoconversion efficiency. *Langmuir* **30**, 5716–5725 (2014).
97. DiMeglio, J. L. & Bartlett, B. M. Interplay of corrosion and photocatalysis during nonaqueous benzylamine oxidation on cadmium sulfide. *Chem. Mater.* **29**, 7579–7586 (2017).
98. Kisch, H. & Bahnemann, D. Best Practice in Photocatalysis: Comparing Rates or Apparent Quantum Yields? *J. Phys. Chem. Lett.* **6**, 1907–1910 (2015).
99. Gomollón-Bel, F. Ten Chemical Innovations That Will Change Our World. *Chem. Int.* **41**, 1–17 (2019).
100. Baker, C. O., Huang, X., Nelson, W. & Kaner, R. B. Polyaniline nanofibers: broadening applications for conducting polymers. *Chem. Soc. Rev.* **46**, 1510–1525 (2017).
101. Jäckle, S. *et al.* Potential of PEDOT:PSS as a hole selective front contact for silicon heterojunction solar cells. *Sci. Rep.* **7**, 2170–2177 (2017).
102. Chen, K., Deng, X., Dodekatos, G. & Tüysüz, H. Photocatalytic Polymerization of 3,4-Ethylenedioxythiophene over Cesium Lead Iodide Perovskite Quantum Dots. *J. Am. Chem. Soc.* (2017).
103. Kirkwood, N. *et al.* Finding and Fixing Traps in II–VI and III–V Colloidal Quantum Dots: The Importance of Z-Type Ligand Passivation. *J. Am. Chem. Soc.* **140**, 15712–15723 (2018).
104. Trent, J. S., Scheinbeim, J. I. & Couchman, P. R. Ruthenium tetraoxide staining of polymers for electron microscopy. *Macromolecules* **16**, 589–598 (1983).
105. Kirchmeyer, S. & Reuter, K. Scientific importance, properties and growing applications of poly(3,4-ethylenedioxythiophene). *J. Mater. Chem.* **15**, 2077–2088 (2005).
106. Kuehnel, M. F. & Reisner, E. Solar Hydrogen Generation from Lignocellulose. *Angew. Chemie Int. Ed.* **57**, 3290–3296 (2018).
107. Wakerley, D. W. *et al.* Solar-driven reforming of lignocellulose to H_2 with a CdS/CdOx photocatalyst. *Nat. Energy* **2**, 17021–17030 (2017).
108. Kasap, H., Achilleos, D. S., Huang, A. & Reisner, E. Photoreforming of lignocellulose into H_2 using nano-engineered carbon nitride under benign conditions. *J. Am. Chem. Soc.* 28 (2018).
109. Uekert, T., Kuehnel, M. F., Wakerley, D. W. & Reisner, E. Plastic waste as a feedstock for solar-driven H_2 generation. *Energy Environ. Sci.* **11**, 2853–2857 (2018).
110. Uekert, T., Kasap, H. & Reisner, E. Photoreforming of Nonrecyclable Plastic Waste over a Carbon Nitride/Nickel Phosphide Catalyst. *J. Am. Chem. Soc.* **141**, 15201−15210 (2019).
111. Simon, T. *et al.* Redox shuttle mechanism enhances photocatalytic H_2

generation on Ni-decorated CdS nanorods. *Nat. Mater.* **13**, 1013–1018 (2014).
112. Ishibashi, K., Fujishima, A., Watanabe, T. & Hashimoto, K. Detection of active oxidative species in TiO_2 photocatalysis using the fluorescence technique. *Electrochem. commun.* **2**, 207–210 (2000).
113. Han, X. *et al.* Structural insight into catalytic mechanism of PET hydrolase. *Nat. Commun.* **8**, 2106–2011 (2017).
114. Habisreutinger, S. N., Schmidt-Mende, L. & Stolarczyk, J. K. Photocatalytic Reduction of CO_2 on TiO_2 and Other Semiconductors. *Angew. Chemie Int. Ed.* **52**, 7372–7408 (2013).
115. Stolarczyk, J. K., Bhattacharyya, S., Polavarapu, L. & Feldmann, J. Challenges and Prospects in Solar Water Splitting and CO_2 Reduction with Inorganic and Hybrid Nanostructures. *ACS Catal.* (2018).
116. Tollefson, J. Can the World Slow Global Warming? *Nature* **572**, 325–326 (2019).
117. Manzi, A. *et al.* Light-Induced Cation Exchange for Copper Sulfide Based CO_2 Reduction. *J. Am. Chem. Soc.* **137**, 14007–14010 (2015).
118. Wang, D. *et al.* How and Why Nanoparticle's Curvature Regulates the Apparent pK_a of the Coating Ligands. *J. Am. Chem. Soc.* **133**, 2192–2197 (2011).
119. Woehrle, G. H., Brown, L. O. & Hutchison, J. E. Thiol-Functionalized, 1.5-nm Gold Nanoparticles through Ligand Exchange Reactions: Scope and Mechanism of Ligand Exchange. *J. Am. Chem. Soc.* **127**, 2172–2183 (2005).
120. Fogg, P. G. T. *Carbon Dioxide in Non-Aqueous Solvents at Pressure less than 200 kPa*. (1992).
121. Rosen, B. A. *et al.* Ionic Liquid-Mediated Selective Conversion of CO_2 to CO at Low Overpotentials. *Science.* **334**, 643–644 (2011).
122. Dong, C. *et al.* Size-dependent activity and selectivity of carbon dioxide photocatalytic reduction over platinum nanoparticles. *Nat. Commun.* **9**, 1252–1262 (2018).
123. Ran, J., Jaroniec, M. & Qiao, S.-Z. Cocatalysts in Semiconductor-based Photocatalytic CO_2 Reduction: Achievements, Challenges, and Opportunities. *Adv. Mater.* **30**, 1704649–1704679 (2018).
124. McQuillin, F. J. *Homogeneous Hydrogenation in Organic Chemistry*. (1976).
125. Prier, C. K., Rankic, D. A. & MacMillan, D. W. C. Visible Light Photoredox Catalysis with Transition Metal Complexes: Applications in Organic Synthesis. *Chem. Rev.* **113**, 5322–5363 (2013).
126. Romero, N. A. & Nicewicz, D. A. Organic Photoredox Catalysis. *Chem. Rev.* **116**, 10075–10166 (2016).
127. Balzani, V., Bergamini, G. & Ceroni, P. Photochemistry and photocatalysis. *Rend. Lincei* (2017).
128. Magagnano, G. *et al.* Photocatalytic ATRA reaction promoted by iodo-Bodipy and sodium ascorbate. *Chem. Commun.* **53**, 1591–1594 (2017).
129. Pal, A., Ghosh, I., Sapra, S. & König, B. Quantum Dots in Visible-Light Photoredox Catalysis: Reductive Dehalogenations and C−H Arylation Reactions Using Aryl Bromides. *Chem. Mater.* **29**, 5225–5231 (2017).

130. Zhang, Z., Edme, K., Lian, S. & Weiss, E. A. Enhancing the Rate of Quantum-Dot-Photocatalyzed Carbon−Carbon Coupling by Tuning the Composition of the Dot's Ligand Shell. *J. Am. Chem. Soc.* **139**, 4246–4249 (2017).
131. Caputo, J. A. *et al.* General and Efficient C−C Bond Forming Photoredox Catalysis with Semiconductor Quantum Dots. *J. Am. Chem. Soc.* **139**, 4250–4253 (2017).
132. Nicewicz, D. A. & MacMillan, D. W. C. Merging photoredox catalysis with organocatalysis: the direct asymmetric alkylation of aldehydes. *Science.* **322**, 77–80 (2008).
133. Lewis, N. S. Developing a scalable artificial photosynthesis technology through nanomaterials by design. *Nat. Nanotechnol.* **11**, (2016).
134. Pinaud, B. A. *et al.* Technical and economic feasibility of centralized facilities for solar hydrogen production via photocatalysis and photoelectrochemistry. *Energy Environ. Sci.* 1983–2002 (2013). doi:10.1039/c3ee40831k
135. O'Regan, B. & Grätzel, M. A low-cost, high-efficiency solar cell based on dye-sensitized colloidal TiO_2 films. *Nature* **353**, 737–740 (1991).
136. Mazzaro, R. *et al.* Uniform Functionalization of High-Quality Graphene with Platinum Nanoparticles for Electrocatalytic Water Reduction. *ChemistryOpen* **4**, 268–273 (2015).
137. Grzelczak, M., Vermant, J., Furst, E. M. & Liz-Marzá, L. M. Directed Self-Assembly of Nanoparticles. *ACS Nano* **4**, 3591–3605 (2010).
138. Cambié, D. & Noël, T. Solar Photochemistry in Flow. *Top. Curr. Chem.* **376**, 45 (2018).
139. Pieber, B., Shalom, M., Antonietti, M., Seeberger, P. H. & Gilmore, K. Heterogeneous Photocatalysis in Serial Micro-Batch Reactors. *Angew. Chemie Int. Ed.* **57**, 9976–9979 (2018).
140. Italia, V. *et al.* Laser-Inscribed Glass Microfluidic Device for Non-Mixing Flow of Miscible Solvents. *Micromachines* **10**, 23–32 (2018).
141. Ashton, P. R. *et al.* A Three-Pole Supramolecular Switch. *J. Am. Chem. Soc.* **121**, 3951–3957 (1999).
142. Niu, W.-J. *et al.* Dumbbell-shaped carbon quantum dots/AuNCs nanohybrid as an efficient ratiometric fluorescent probe for sensing cadmium (II) ions and l-ascorbic acid. *Carbon N. Y.* **96**, 1034–1042 (2016).
143. Ju, E. *et al.* Heterogeneous Assembled Nanocomplexes for Ratiometric Detection of Highly Reactive Oxygen Species in Vitro and in Vivo. *ACS Nano* **6**, 6014–6023 (2019).
144. Kodaimati, M. S. *et al.* Viewpoint: Challenges in Colloidal Photocatalysis and Some Strategies for Addressing Them. *Inorg. Chem.* **57**, 3659–3670 (2018).
145. Carbone, L. *et al.* Synthesis and Micrometer-Scale Assembly of Colloidal CdSe/CdS Nanorods Prepared by a Seeded Growth Approach. *Nano Lett.* **7**, 2942–2950 (2007).

Chapter 5 Conclusion and Outlook

5.1 Key Findings

This thesis has explored the photochemical properties of core-shell CdSe@CdS seeded nanorods (SR), followed by their applications in a variety of light-triggered chemical transformations. Drawing from established synthetic protocols, the exceptional optoelectronic properties of this class of materials afforded rigorous spectroscopic material-function descriptions, yielding improved solar energy conversion performances.

In the first part of this thesis, H_2 generation was coupled to alternative oxidative organic transformations in the framework of solar chemicals production. World-record efficiencies for PC device systems were obtained through the simultaneous synthesis of hydrogen and benzaldehyde, through direct oxidation of benzylamine or benzylalcohol. Having realised a sacrificial-free endergonic reaction, we elevated the solar-to-chemical energy conversion efficiency index, or *STC*, to a crucial figure-of-merit assessing closed-cycle photosynthetic redox processes. In particular, Pt-SR promoted H_2/BnCHO production, which extracts $335.4\ kJ\ mol^{-1}$ from solar radiation, at maximum STC values of 1.2% at 1 sun and 4.2% at 0.1 sun. In parallel to the research efforts aiming at boosting STH performance, we demonstrated the ability of Pt-SR to be efficient in both H_2 production and value-added chemicals synthesis. Remarkably, the reactions have been predicted through fluorescence quenching screening and performed in mild experimental conditions, namely at room temperature and using water and acetonitrile as reaction solvents. Further organic oxidative schemes touched the possibility to process polymer moieties via photochemical mechanisms, either through the creation of aniline- or EDOT-based conductive composites, or the photo-reforming of waste plastic feedstock.

This investigation led us to consider other redox chemistries to be performed with seeded nanorods. Specifically, when targeting CO_2 reduction, we were

surprised by the outcompeting selectivity towards the undesired H_2 generation. Nevertheless, this proved invaluable in the possibility to conduct photo-hydrogenations in organic solvents, leveraging on in-situ production of reducing equivalents. Later, de-halogenations and C-C couplings were explored in sight of a full utilisation of the concerted electron-transfer mechanism of Pt-SR for organic synthetic purposes. Finally, we proceded with the proof-of-concept demonstration of fully functional photochemical device with the integration of SR in microfluidic flow photoreactors. Initial insights on the physical and chemical functionalisation of the device channels walls may pave the way for future optimisation of proof-of-concept solar synthesis in continuous flow.

5.2 Outlook

The comprehensive investigation of oxidative photochemical processes promoted by CdSe@CdS nanorods revealed a new pathway in efficient solar-to-chemical energy conversion. Water is unarguably the ultimate feedstock to be exploited for solar fuels production, yet oxygen production poses severe kinetics and technological limitations. Solar chemicals synthesis will, on the other hand, exalt human mastery achieved across the chemistry, physics, materials science and engineering disciplines.

It is our responsibility to make, in the imminent future, better use of radiant energy to surpass fossil solar energy utilisation. To this extent, opening solar-to-hydrogen approaches to a wide gallery of oxidative organic transformations can result in practical technological solutions. In addition to that, achieving both chemical selectivity and material's photostability will endeavour nanoscience research with unprecedented scientific challenges. In semiconductor photocatalysis precise control of reaction sites at the semiconductor-surfactant-solvent interface is a basic requirement for improving the conversion of light into chemical energy. The specific geometry of semiconductor nanorods opens the possibility of fine tuning both synthetic and post-processing techniques. This solicits in turns the

development of more sensitive operando characterisation tools, but also the establishment of a large data pool of materials-function properties. With respect to this, we demonstrated how readily available tools such as fluorescence quenching screening yields rigorous assessment of the inceptive photochemical event, i.e. electron transfer. In spite of that, additional understanding of the Stern-Volmer and Langmuir-based descriptions for collisional phenomena between colloidal nanostructures and solute quenchers are yet to be fully understood. We believe that techniques like transient absorption will greatly contribute in completing the description of the overall photophysical picture.

Lastly, successful integration of Pt-SR and similar materials into microfluidic flow photoreactors will bridge the gap between lab-to-fab device deployment. The obvious advantages of continuous reagent replenishment and photocatalyst recyclability will unavoidably make batch processing obsolete. It this regard, however, we believe of primary importance the development of proper reaction optimisation procedures. The thorough investigations conducted for light-intensity and substrate concentration performance dependence should be perceived in an effort to avoid trail-and-error design of experiments. Overall, a holistic approach to synthesis, characterisation, operando assessment and data analysis and reporting is proved, once more, of vital importance for semiconductor-based photochemical systems.

In this regard, Ciamician envisioned in 1912 the photochemistry of the future with these avant-gardist words:

"*On the arid lands there will spring up industrial colonies without smoke and without smokestacks; forests of glass tubes will extend over the plains and glass buildings will rise everywhere; inside of these will take place the photochemical processes that hitherto have been the guarded secret of plants, but that will have been mastered by human industry which will know how to make them bear even more abundant fruit than nature, for nature is not in a hurry and mankind is.*"

Chapter 6 Methods

6.1 Colloidal Nano Heterostructure Synthesis

The synthesis of colloidal core-shell CdSe@CdS seeded rods and the corresponding metal-tipped hybrid heterostructure was adapted following the contributions described in Chapter 2.2.2. All the data presented in this thesis was collected with materials synthesised by the author at the collaborating Prof. Amirav research group at Technion Israel Institute of Technology (Haifa-Israel), except for experiments performed with Ni- and Au-tipped SR, that were provided by Dr. Yifat Nakibli (Technion) and Dr. Dong Kaituo (Technion), respectively.

In general, synthesis of metal-tipped SR follows consequential colloidal synthesis of:

- CdSe QD
- CdSe@CdS Seeded NR
- Pt, Ni and Au QD anchoring to CdSe@CdS-SR

Synthesis of Cadmium Selenide Quantum Dots (CdSe QD)

Firstly, CdSe Seeds were synthesized following Carbone, Manna L. and co-authors procedure[145]. 60mg of Cadmium Oxide (CdO) (Sigma Aldrich) 0.280g of Octadecylphosphonic acid (ODPA, Sigma Aldrich) and 3.0g of Trioctylphosphine oxide (TOPO, Sigma Aldrich) are heated to 150°C in a 25mL three-neck flask flushed under argon, followed by a 1 hour long vacuum stage. Then, again under argon, the solution is heated to 300°C. At this point, 1.5 g of Trioctylphosphine (TOP, Sigma Aldrich) is injected into the flask. The temperature is raised to 370°C and the flask is removed from the heating mantle. Upon cooling, at 350-330°C, TOP:Se solution (0.058g Se + 0.360g TOP) is rapidly injected. The reaction time is modified in order to synthesize CdSe dots of different sizes. In this work we used

2.3 nm CdSe seeds with green fluorescence, obtained by removal of the heating mantle immediately after the injection. After the synthesis, the nanocrystals are precipitated with methanol, and are washed by repeated redissolution in toluene and precipitation by the addition of methanol.

Synthesis of Cadmium Sulphide Seeded Rods (CdSe@CdS)

The procedure for the seeded rods synthesis was adopted from Talapin, Alivisatos et al.[49]. 0.230 g of CdO, 1.08 g of ODPA, 0.075g of Propylphosphonic acid (Sigma Aldrich), and 3.35 g of TOPO were loaded into a 25 mL three-neck flask and heated to 120°C for 30 min under vacuum. The mixture was heated to 320 °C under flowing argon to produce an optically clear solution. After the CdO completely dissolved, the solution was cooled to 120°C and put under vacuum for 2 h for removal of water, after which it was heated to 340°C under flowing Ar. At this time, 1.5 g of TOP were injected and the flask was allowed to return to 340°C. TOP:S was prepared by reacting equimolar amounts of TOP and elemental sulphur under inert atmosphere. 0.65 g of TOP:S was injected into the flask at 340 °C, followed after 20 s by the injection of the CdSe seeds dissolved in 0.50 g of TOP. The CdSe solution was prepared by evaporating 0.3 g of $5 \cdot 10^{-3}$ M solution of CdSe nanocrystals in toluene and redispersing in TOP (gentle sonication might be necessary). The reaction temperature was adjusted to 320 °C, and the reaction was stopped after 15 min by the removal of the heating mantle and the injection of 4 mL of anhydrous toluene. The nanorods were isolated and cleaned by a few repeatable steps of precipitation and redissolution using toluene/hexane/chloroform as solvent and isopropanol/methanol as nonsolvent (10:7 solvent to nonsolvent ratio), with the alternating addition octylamine and nonanoic acid (about 1-2 ml). Precipitation was achieved by centrifugation for 20-30 min under 4000 rpm. Modifications to this synthetic procedure allow for control of nanorod length and diameter. The length of the rods could be controlled by the injection of different amounts of CdSe dots with more dots producing shorter rods. Also, the reaction time could be changed to

control rod length; longer growth times produce longer rods. Finally, the diameter and length of the rods could be controlled by the amount of TOP:S injected into the reaction; more TOP:S produces longer and skinnier rods.

Colloidal Growth of Metal tips on CdSe@CdS-SR

The procedure for colloidal Pt tipping was adopted from Mokari T. and coauthors[47]. Oleic acid (0.2 mL), oleylamine (0.2 mL), 43.0 mg of 1,2-hexadecanediol and 10 ml of diphenyl ether were loaded into a 25 mL three-neck flask and heated to 80 °C under vacuum for 30 min to remove traces of water. Pt (acetylacetonate)$_3$ (13 mg) was added to a suspension of CdSe@CdS rods (about half of the synthesis product (~ 16.4 mg) in dichlorobenzene (DCB, ~1 ml) and the solution was sonicated for a few seconds to promote dissolution of the Pt precursor. Under argon, the mixture of surfactants and diphenyl ether was heated to 200 °C. At this point the Pt precursor and seeded rods in dichlorobenzene were injected into the flask. Upon temperature readjustment to 200 °C the solution turned black. After several minutes (about 4 min; the time depends on the amount of seeded rods and the quality of their cleaning procedure) the reaction was removed from the heating mantle and quenched in a water bath. The Pt tipped nanorods were isolated and cleaned by a few repeatable steps of precipitation/redissolution. Homogenous nucleation of Pt dots in the reaction flask contributed to the strong black color of the crude product. The clean solution of Pt tipped seeded rods in toluene is brown. The key factor determining the amount of tips that will grow on each rod is the Pt-NR molar ratio.

Synthesis of Ni and Au QD followed instead the procedure from Nakibli, Amirav et al. Mokari, Alivisatos et al. ad, respectively[47,64].

Ligand Exchange

Finally, all the experiments carried out in aqueous solvent mixture required a ligand exchange procedure. In particular, the TOP ligands on the tipped seeded rods with 11-mercaptoundecanoic acid (MUA, Sigma Aldrich), a polar ligand that will allow

the particles to be well dispersed and suspended in water. The platinum tipped seeded rods are precipitated from solution (via the addition of non-solvent and the use of centrifuge). Next, 250 mg of 11- mercaptoundecanoic acid are dissolved in 20g of methanol. Tetramethylammonium hydroxidepentahydrate salt is added until solution pH of 11 is obtained. The MUA solution in methanol is added to the particles residue and. This should result in a clean brown solution. Next, the particles are precipitated from the methanol using toluene as non solvent and centrifuging at 6000 rpm. The particles are then redispersed in water.

6.2 Optical Characterisation

Optical Characterisations were carried out by the author both at Prof. Bergamini (University of Bologna) and Prof. Amirav (Technion) research laboratories.

Electronic Absorption and Fluorescence Spectra

UV/Vis absorption spectra were recorded with a PerkinElmer l40 spectrophotometer, using quartz cells with path length of 1.0 cm. Fluorescence spectra were obtained with a PerkinElmer LS-50 spectrofluorimeter, equipped with a Hamamatsu R928 phototube. Spectra were used frequently to determine seed size, seed concentration, rod concentration, and the absorbance of solutions used for hydrogen production. Fluorescence quantum yields were measured following the method of Resch-Genger et al.[86]. The estimated experimental errors are: 2 nm on the band maximum, 5% on the molar absorption co- efficient and log K values, 10% on the fluorescence quantum yield.

Excited State Lifetime Measurements

Fluorescence lifetime measurements were performed by an Edinburgh FLS920 spectrofluorimeter equipped with a TCC900 card for data acquisition in time-correlated single-photon counting experiments (0.5 ns time resolution) with a D2 lamp and a LDH-P-C-405 pulsed diode laser.

6.3 Materials Characterisation

Transmission Electron Microscopy measurements were carried out by the author at the MIKA Electron Microscopy Centre (Technion). Scanning Electron Microscopy images were taken by Dr. Mazzaro Raffaello at CNR Institute (Bologna).

Transmission Electron Microscopy Measurements

Transmission Electron Microscopy was carried out on a FEI Tecnai G^2 T20 S-Twin TEM, running at 200keV with a LaB_6 electron source and an FEI Supertwin Objective Lens or on a FEI Titan 80-300 KeV S/TEM at 300keV with a field emission gun electron source. Samples for TEM were prepared by either dropping the solution directly or by aerosolized spray onto 300 mesh ultrathin carbon on lacey carbon grids purchased from Ted Pella Inc.

Scanning Electron Microscopy Measurements

The SEM images displayed in Chapter 4 were recorded by a Zeiss Leo Gemini 1530 equipped a Schottky emitter and a high efficiency in-lens electron detector. The

instrument is operated at an accelerating voltage of 5 kV in order to maximize the morphological contrast of thin nanomaterials. The samples are supported on a conventional SEM stub and sticked with carbon tape to ensure a good electrical contact.

6.4 Photoreaction Characterisation

Photochemical experiments were performed by the author both at Prof. Amirav (Technion) research laboratories and at the collaborating Prof. Natali research group (University of Ferrara).

Hydrogen Production Measurements (Technion)

Rods solutions were moved to ultrapure water by MUA ligand exchange as close as possible to starting a new measurement, usually less than one hour before the cell was first purged. Samples were diluted using ultrapure water, after which desired amounts of $BnNH_2$ or BnOH were added to make 10 mL solutions. The gas tight reaction cells (Figure A1) were closed and connected to a 10 mL/min argon line (filtered 99.999% purity) and an Agilent 7890A Series gas chromatograph with a thermal conductivity detector (GC-TCD). The cell on the right has an inlet port that enables further injections of $BnNH_2$, or to withdraw sample time aliquots. Gas was continually flowed through the cell in the dark while the solution was stirred and gas samples were automatically taken every 5-10 minutes for measurement to monitor the purging process.

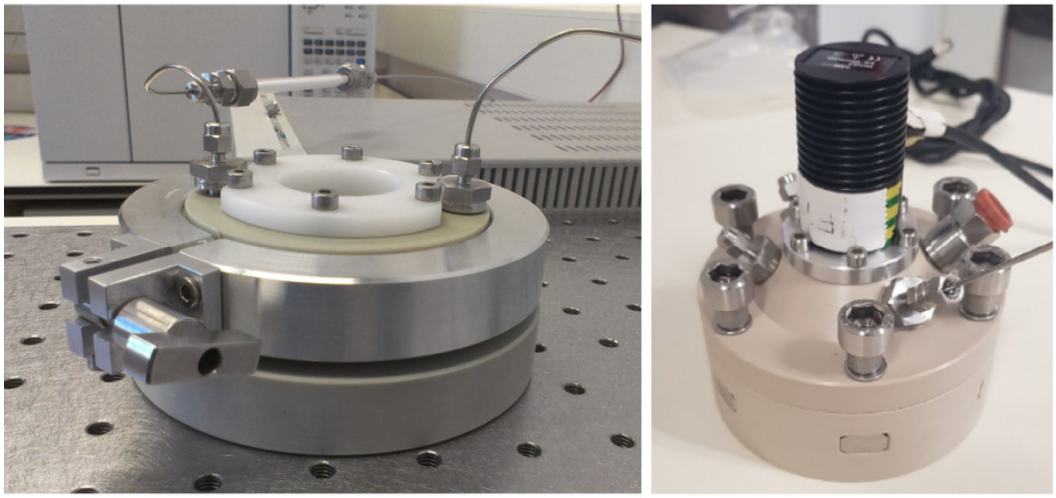

Figure A1. ***Photoreactor cells used at Technion.***

In a typical monochromatic excitation experiment a Thorlabs Royal Blue (455 nm) high-power LED was switched on to illuminated the sample once the cell was fully purged. The photon flux was calculated by measuring the LED power (which was adjusted to a desired value and measured using a Thorlabs Digital Optical Meter – PM206) assuming all photons had the same wavelength of 455 nm. In this adjustment of the power we accounted for the irradiated area over the sample, as well as for the absorption of the reaction cell window and other minor losses in the setup. The LED power used during this work was 50 mW.

The hydrogen production rate generated by each sample was determined based on the area of the hydrogen gas peak, adjusted from μV/min (as reported by the TCD) directly to the number of hydrogen molecules produced per min or in units of μL_{H2} /min, via calibration. Calibration was preformed using an electrolysis unit, built into a calibration cell that is identical to the sample cell, except that it has two nickel electrodes which can be connected to an external power supply. This method of calibration offers three distinct advantages over traditional calibration methodologies with a standard gas sample: (1) a calibration curve can be easily made with numerous points; (2) accurate calibration can be made even for extremely low amounts of hydrogen; and (3) the calibration precisely mimics the experimental conditions and thus is as accurate as can be.

Experiments under simulated AM1.5 100 mW/cm2 sunlight were performed by a class AAB ABET Technologies Sun 2000 simulator with a Keithley 2400

sourcemeter. The lamp intensity was calibrated with an NRELcertified KG5 filtered silicon reference diode with a mismatch factor of 1.01.

Hydrogen Production Measurements (Ferrara)

The photoreactor cells used at the University of Ferrara features a closed headspace from which automatic withdrawal by the GC pump takes place for gas detection and quantification. All connections involving electrodes are gas-tight (*Ace Glass Inc., USA*). The gas atmosphere of the reaction cell is analysed on an Agilent Technologies 490 micro-GC equipped with a 5 Å molecular sieve column (10 m) and a thermal conductivity detector (TCD). Argon was used as the carrier gas. 5 mL from the headspace are sampled by the internal GC pump and 200 nL are injected in the column maintained at 60 °C for separation and detection of gases. The unused gas sample is then reintroduced in the reactor in order to minimize its consumption along the whole experiment. The amount of hydrogen produced during the photo-electrolysis was quantified from a calibration procedure based on a galvanostatic electrolysis (−0.5 mA, 1 h) of a 0.1 M H_2SO_4 solution with a Pt electrode using the same setup and experimental conditions. A 100% faradaic efficiency was assumed leading to a linear correlation between the amount of hydrogen evolved at the Pt cathode and the electrolysis time. A LOT-Oriel solar simulator, equipped with an AM 1.5 G filter, was used as the illumination source, and set to 0.1 Wcm^{-2} incident irradiance power by means of a Power Meter (Newport 1918-C).

Gas-Chromatography Mass-Spectroscopy (GC-MS) Measurements

GC-MS data was collected with a Hewlett- Packard 5971 spectrometer with GC injection and EI ionisation at 70 eV coupled with an Agilent Technologies MSD1100 single-quadrupole mass spectrometer, reported as: m/z (rel. intensity).

High-Performance Liquid Chromatography (HP-LC) Measurements

Analysis were performed with an Agilent Infinity 1260 liquid chromatograph (HPLC-DAD) equipped with an Aminex HPX 87-H 300 mm 7.8 mm column using a 0.005 M H2SO4 solution as the mobile phase. For HMF (Sigma Aldrich) photo-oxidation experiments, an external calibration method was used for the identification, quantification of reactants and products using reference commercial samples. Particular care was devoted to the determination of the C balance, which was found to always fall between 95 and 105% (calculated as the comparison between converted HMF and the sum of the product yields).

Nuclear Magnetic Resonance Measurements

1H-NMR and 13C-NMR spectra were recorded on Varian INOVA 400 (400 MHz) spectrometers. Chemical shifts are reported in ppm using tetramethylsilane as the internal reference standard. Data are reported as follows: chemical shift, multiplicity (s = singlet, d = doublet, t = triplet, q = quartet, br = broad, m = multiplet), coupling constants (Hz). LC-electrospray ionization mass spectra were obtained with an Agilent Technologies MSD1100 single-quadrupole mass spectrometer.

References

1. Pearson, P. N. & Palmer, M. R. Atmospheric carbon dioxide concentrations over the past 60 million years. *Nature* **406**, 695–699 (2000).
2. Sapart, C. J. *et al.* Natural and anthropogenic variations in methane sources during the past two millennia. *Nature* **490**, 85–88 (2012).
3. Cook, J. *et al.* Consensus on consensus: a synthesis of consensus estimates on human-caused global warming. *Environ. Res. Lett.* **11**, 1–7 (2016).
4. *World Energy Outlook 2018*. *International Energy Agency Publications* (2018).
5. Lewis, N. S. & Nocera, D. G. Powering the planet: Chemical challenges in solar energy utilization. *Proc. Natl. Acad. Sci.* **103**, 15729–15735 (2006).
6. Tachibana, Y., Vayssieres, L. & Durrant, J. R. Artificial photosynthesis for solar water-splitting. *Nat. Photonics* **6**, 511–518 (2012).
7. Kornienko, N., Zhang, J. Z., Sakimoto, K. K., Yang, P. & Reisner, E. Interfacing nature's catalytic machinery with synthetic materials for semi-artificial photosynthesis. *Nat. Nanotechnol.* **13**, 890–899 (2018).
8. United States Department of Energy. *DOE Technical Targets for Hydrogen Production from Photoelectrochemical Water Splitting*. (2011).
9. Japanese Ministerial Council on Renewable Energy - Hydrogen and Related Issues. *Basic Hydrogen Strategy*. (2017).
10. Jang, J.-W. *et al.* Toward practical solar hydrogen production-an artificial photosynthetic leaf-to-farm challenge. *Chem. Soc. Rev.* **48**, 1908–1971 (2019).
11. Goto, Y. *et al.* A Particulate Photocatalyst Water-Splitting Panel for Large-Scale Solar Hydrogen Generation. *Joule* **2**, 509–520 (2018).
12. Hisatomi, T. & Domen, K. Reaction systems for solar hydrogen production via water splitting with particulate semiconductor photocatalysts. *Nat. Catal.* **2**, 387–399 (2019).
13. Fabian, D. M. *et al.* Particle suspension reactors and materials for solar-driven water splitting. *Energy Environ. Sci.* **8**, 2825–2850 (2015).
14. Ciamician, G. The photochemistry of the future. *Science.* **36**, 385–394 (1912).
15. Verhoeven, J. W. Glossary of Terms used in Photochemistry. *Pure Appled Chem.* **68**, 2223–2286 (1996).
16. Kisch, H. *Semiconductor Photocatalysis*. (2014).
17. Barber, J. Biological solar energy. *Philos. Trans. Math. Phys. Eng. Sci.* **365**, 1007–1023 (2007).
18. Böer, K. W. The solar spectrum at typical clear weather days. *Sol. Energy* **19**, 525–538 (1977).
19. Blankenship, R. E. *et al.* Comparing Photosynthetic and Photovoltaic Efficiencies and Recognizing the Potential for Improvement. *Science.* **332**, 805–809 (2011).
20. Bolton, J. R. & Hall, D. O. Conversion and Storage. *Annu. Rev. Energy* **4**, 353–401 (1979).
21. Ross, R. T. & Hsiao, T.-L. Limits on the yield of photochemical solar

energy conversion. *J. Appl. Phys.* **48**, 4783–4785 (1977).
22. Bolton, J. R. Solar Fuels : The production of energy-rich compounds by the photochemical conversion and storage of solar energy. *Science.* **202**, 705–711 (1978).
23. Bolton, J. R., Haught, A. F. & Ross, R. T. Photochemical Energy Storage: An Analysis of Limits. in *Photochemical Conversion and Storage of Solar Energy* 297–346 (1981).
24. Bolton, J. R., Strickler, S. J. & Connolly, J. S. Limiting and realizable efficiencies of solar photolysis of water. *Nature* **316**, 495–500 (1985).
25. Archer, M. D. & Bolton, J. R. Requirements for Ideal Performance of Photochemical and Photovoltaic Solar Energy Converters. *J. Phys. Chem.* **94**, 8028–8036 (1990).
26. Shockley, W. & Queisser, H. J. Detailed Balance Limit of Efficiency of p-n Junction Solar Cells. *J. Appl. Phys.* **32**, 510–519 (1961).
27. Baierlein, R. The elusive chemical potential. *Am. J. Phys.* **69**, 423–434 (2001).
28. McConnell, I., Li, G. & Brudvig, G. W. Energy Conversion in Natural and Artificial Photosynthesis. *Chem. Biol.* **17**, 434–447 (2010).
29. Fujishima, A. & Honda, K. Electrochemical Photolysis of Water at a Semiconductor Electrode. *Nature* **238**, 37–38 (1972).
30. Kirch, M., Lehn, J.-M. & Sauvage, J.-P. Hydrogen Generation by Visible Light Irradiation of Aqueous Solutions of Metal Complexes. An approach to the photochemical conversion and storage of solar energy. *Helv. Chim. Acta* **62**, 1345–1384 (1979).
31. Bard, A. J. Photoelectrochemistry and heterogeneous photo-catalysis at semiconductors. *J. Photochem.* **10**, 59–75 (1979).
32. Grätzel, M. Artificial Photosynthesis: Water Cleavage into Hydrogen and Oxygen by Visible Light. *Acc. Chem. Res.* **14**, 376–384 (1981).
33. Đokicá, M. & Soo, H. Sen. Artificial photosynthesis by light absorption, charge separation, and multielectron catalysis. *Chem. Commun.* **54**, 6554–6572 (2018).
34. Serpone, N. *et al.* Why do Hydrogen and Oxygen Yields from Semiconductor-Based Photocatalyzed Water Splitting Remain Disappointingly Low? Intrinsic and Extrinsic Factors Impacting Surface Redox Reactions. *ACS Energy Lett.* **1**, 931–948 (2016).
35. Madelung, O. II-VI compounds. in *Semiconductors: Data Handbook* 173–244 (2004).
36. Steigerwald, M., Bawendi, M. G., Steigerwald, M. L. & Brus, L. E. The Quantum Mechanics of Larger Semiconductor Clusters. *Annu. Rev. Phys. Chem.* **41**, 477–96 (2003).
37. Yang, W. *et al.* Electron Accumulation Induces Efficiency Bottleneck for Hydrogen Production in Carbon Nitride Photocatalysts. *J. Am. Chem. Soc.* **141**, 11219–11229 (2019).
38. Edvinsson, T. Optical quantum confinement and photocatalytic properties in two-, one-and zero-dimensional nanostructures. *R. Soc. Open Sci.* **5**, 180387–180403 (2018).
39. Li, X., Yu, J. & Jaroniec, M. Hierarchical photocatalysts. *Chem. Soc. Rev.* **45**, 2603–2636 (2016).

40. Kovalenko, M. V. *et al.* Prospects of Nanoscience with Nanocrystals. *ACS Nano* **9**, 1012–1057 (2015).
41. Wu, K. & Lian, T. Quantum confined colloidal nanorod heterostructures for solar-to-fuel conversion. *Chem. Soc. Rev.* **45**, 3759–4034 (2016).
42. Alivisatos, A. P. Perspectives on the Physical Chemistry of Semiconductor Nanocrystals. *J. Phys. Chem.* **100**, 13226–13239 (1996).
43. Murray, C. B., Norris, D. J. & Bawendi, M. G. Synthesis and Characterization of Nearly Monodisperse CdE (E = S, Se, Te) Semiconductor Nanocrystallites. *J. Am. Chem. Soc* **115**, 8706–8715 (1993).
44. Weiss, E. A. Designing the surfaces of semiconductor quantum dots for colloidal photocatalysis. *ACS Energy Lett.* **2**, 1005–1013 (2017).
45. Amirav, L. & Alivisatos, A. P. Photocatalytic Hydrogen Production with Tunable Nanorod Heterostructures. *J. Phys. Chem. Lett* **1**, 1051–1054 (2010).
46. Peng, X. *et al.* Shape control of CdSe nanocrystals. *Nature* **404**, 3408–3413 (2000).
47. Mokari, T., Rothenberg, E., Popov, I., Costi, R. & Banin, U. Selective Growth of Metal Tips onto Semiconductor Quantum Rods and Tetrapods. *Science.* **304**, (2004).
48. Habas, S. E., Yang, P. & Mokari, T. Selective Growth of Metal and Binary Metal Tips on CdS Nanorods. *J. Am. Chem. Soc.* **130**, 3294–3295 (2008).
49. Talapin, D. V. *et al.* Seeded Growth of Highly Luminescent CdSe/CdS Nanoheterostructures with Rod and Tetrapod Morphologies. *Nano Lett.* **7**, 2951–2959 (2007).
50. Amirav, L. & Alivisatos, A. P. Luminescence Studies of Individual Quantum Dot Photocatalysts. *J. Am. Chem. Soc.* **135**, 13049–13053 (2013).
51. Kalisman, P., Nakibli, Y. & Amirav, L. Perfect photon-to-hydrogen conversion efficiency. *Nano Lett.* **16**, 1776–1781 (2016).
52. Amirav, L., Oba, F., Aloni, S. & Alivisatos, A. P. Modular Synthesis of a Dual Metal-Dual Semiconductor Nano-Heterostructure. *Angew. Chemie Int. Ed.* **54**, 7007–7011 (2015).
53. Serpone, N. *et al.* Standardization protocol of process efficiencies and activation parameters in heterogeneous photocatalysis: Relative photonic efficiencies ζr. *J. Photochem. Photobiol. A Chem.* **94**, 191–203 (1996).
54. Kisch, H. Semiconductor photocatalysis for chemoselective radical coupling reactions. *Acc. Chem. Res.* **50**, 1002–1010 (2017).
55. Ghosh, I. *et al.* Organic semiconductor photocatalyst can bifunctionalize arenes and heteroarenes. *Science.* **365**, 360–366 (2019).
56. Kisch, H. On the Problem of Comparing Rates or Apparent Quantum Yields in Heterogeneous Photocatalysis. *Angew. Chemie Int. Ed.* **49**, 9588–9589 (2010).
57. Qureshi, M. & Takanabe, K. Insights on Measuring and Reporting Heterogeneous Photocatalysis: Efficiency Definitions and Setup Examples. *Chem. Mater.* **29**, 158–167 (2017).
58. Kunz, L. Y. *et al.* Artificial inflation of apparent photocatalytic activity induced by catalyst-mass-normalization and a method to fairly compare heterojunction systems. *Energy Environ. Sci.* **12**, 1657–1667 (2019).
59. Osterloh, F. E. Photocatalysis versus Photosynthesis: A Sensitivity

Analysis of Devices for Solar Energy Conversion and Chemical Transformations. *ACS Energy Lett.* **2**, 445–453 (2017).
60. Coontz, R. *et al.* Toward a Hydrogen Economy. *Science.* **305**, 957–976 (2004).
61. Tang, J., Durrant, J. R. & Klug, D. R. Mechanism of photocatalytic water splitting in TiO_2. Reaction of water with photoholes, importance of charge carrier dynamics, and evidence for four-hole chemistry. *J. Am. Chem. Soc.* **130**, 13885–13891 (2008).
62. Wolff, C. *et al.* All-in-one visible-light-driven water splitting by combining nanoparticulate and molecular co-catalysts on CdS nanorods. *Nat. Energy* **3**, 862–869 (2018).
63. You, B., Han, G. & Sun, Y. Electrocatalytic and photocatalytic hydrogen evolution integrated with organic oxidation. *Chem. Commun.* **54**, 5943–5955 (2018).
64. Nakibli, Y. & Amirav, L. Selective Growth of Ni Tips on Nanorod Photocatalysts. *Chem. Mater.* **28**, 4524–4527 (2016).
65. Norris, D. J., Sacra, A., Murray, C. B. & Bawendi, M. G. Measurement of the size dependent hole spectrum in CdSe quantum dots. *Phys. Rev. Lett.* **72**, 2612–2615 (1994).
66. Ekimov, A. I. *et al.* Absorption and intensity-dependent photoluminescence measurements on CdSe quantum dots: assignment of the first electronic transitions. *J. Opt. Soc. Am. B* **10**, 100–107 (1993).
67. Hoang, T. B. *et al.* Temperature dependent photoluminescence of single CdS nanowires. *Appl. Phys. Lett.* **89**, 1231231–1231233 (2006).
68. Puthussery, J., Lan, A., Kosel, T. H. & Kuno, M. Band-Filling of Solution-Synthesized CdS Nanowires. *ACS Nano* **2**, 357–367 (2008).
69. Shabaev, A. & Efros, A. L. 1D Exciton Spectroscopy of Semiconductor Nanorods. *Nano Lett.* **4**, 1821–1825 (2004).
70. Sitt, A., Sala, F. Della, Menagen, G. & Banin, U. Multiexciton Engineering in Seeded Core/Shell Nanorods: Transfer from Type-I to Quasi-type-II Regimes. *Nano Lett.* **9**, 3470–3476 (2009).
71. Rainò, G. *et al.* Probing the Wave Function Delocalization in CdSe/CdS Dot-in-Rod Nanocrystals by Time- and Temperature-Resolved Spectroscopy. *ACS Nano* **5**, 4031–4036 (2011).
72. Smith, E. R., Luther, J. M. & Johnson, J. C. Ultrafast Electronic Delocalization in CdSe/CdS Quantum Rod Heterostructures. *Nano Lett.* **11**, 4923–4931 (2011).
73. Wu, K. *et al.* Universal Length Dependence of Rod-to-Seed Exciton Localization Efficiency in Type I and Quasi-Type II CdSe@CdS Nanorods. *ACS Nano* **9**, 4591–4599 (2015).
74. Christodoulou, S. *et al.* Band structure engineering via piezoelectric fields in strained anisotropic CdSe/CdS nanocrystals. *Nat. Commun.* **6**, 7905–7912 (2015).
75. Lakowicz, J. R. *Principles of Fluorescence Spectroscopy*. (2006).
76. Tarafder, K., Surendranath, Y., Olshansky, J. H., Alivisatos, A. P. & Wang, L.-W. Hole Transfer Dynamics from a CdSe/CdS Quantum Rod to a Tethered Ferrocene Derivative. *J. Am. Chem. Soc.* **136**, 5121–5131 (2014).
77. Mokari, T., Sztrum, C. G., Salant, A., Rabani, E. & Banin, U. Formation of

asymmetric one-sided metal-tipped semiconductor nanocrystal dots and rods. *Nat. Mater.* **4**, 855–863 (2005).
78. Wu, K. *et al.* Hole Removal Rate Limits Photodriven H $_2$ Generation Efficiency in CdS-Pt and CdSe/CdS-Pt Semiconductor Nanorod–Metal Tip Heterostructures. *J. Am. Chem. Soc.* **136**, 7708–7716 (2014).
79. Lupo, M. G. *et al.* Ultrafast Electron−Hole Dynamics in Core/Shell CdSe/CdS Dot/Rod Nanocrystals. *Nano Lett.* **8**, 4582–4587 (2008).
80. Utterback, J. K. *et al.* Observation of trapped-hole diffusion on the surfaces of CdS nanorods. *Nat. Chem.* **8**, 1061–1066 (2016).
81. Grennell, A. N., Utterback, J. K., Pearce, O. M., Wilker, M. B. & Dukovic, G. Relationships between Exciton Dissociation and Slow Recombination within ZnSe/CdS and CdSe/CdS Dot-in-Rod Heterostructures. *Nano Lett.* **17**, 3764–3774 (2017).
82. Utterback, J. K., Hamby, H., Pearce, O. M., Eaves, J. D. & Dukovic, G. Trapped-Hole Diffusion in Photoexcited CdSe Nanorods. *J. Phys. Chem. C* **122**, 16974–16982 (2018).
83. Pearce, O. M., Duncan, J. S., Damrauer, N. H. & Dukovic, G. Ultrafast Hole Transfer from CdS Quantum Dots to a Water Oxidation Catalyst. *J. Phys. Chem. C* **122**, 17559–17565 (2018).
84. Tran, K. & Ulissi, Z. W. Active learning across intermetallics to guide discovery of electrocatalysts for CO_2 reduction and H_2 evolution. *Nat. Catal.* **1**, 696–703 (2018).
85. Hopkinson, M. N., Gómez-Suárez, A., Teders, M., Sahoo, B. & Glorius, F. Accelerated discovery in photocatalysis using a mechanism-based screening method. *Angew. Chemie Int. Ed.* **128**, 4434–4439 (2016).
86. Würth, C., Grabolle, M., Pauli, J., Spieles, M. & Resch-Genger, U. Relative and absolute determination of fluorescence quantum yields of transparent samples. *Nat. Protoc.* **8**, 1535–1550 (2013).
87. Morris-Cohen, A. J., Vasilenko, V., Amin, V. A., Reuter, M. G. & Weiss, E. A. Model for Adsorption of Ligands to Colloidal Quantum Dots with Concentration-Dependent Surface Structure. *ACS Nano* **6**, 557–565 (2012).
88. Uematsu, T., Shimomura, E., Torimoto, T. & Kuwabata, S. Evaluation of Surface Ligands on Semiconductor Nanoparticle Surfaces Using Electron Transfer to Redox Species. *J. Phys. Chem. C* **120**, 16012–12023 (2016).
89. Tachiya, M. Application of a generating function to reaction kinetics in micelles. Kinetics of quenching of luminescent probes in micelles. *Chem. Phys. Lett.* **33**, 289–292 (1975).
90. Ross, R. T. & Calvin, M. Thermodynamics of Light Emission and Free-Energy Storage in Photosynthesis. *Biophys. J.* **7**, 595–614 (1967).
91. Wang, Z. J., Garth, K., Ghasimi, S., Landfester, K. & Zhang, K. A. I. Conjugated Microporous Poly(Benzochalcogenadiazole)s for Photocatalytic Oxidative Coupling of Amines under Visible Light. *ChemSusChem* **8**, 3459–3464 (2015).
92. Xiao, X., Jiang, J. & Zhang, L. Selective oxidation of benzyl alcohol into benzaldehyde over semiconductors under visible light: The case of $Bi_{12}O_{17}Cl_2$ nanobelts. *Appl. Catal. B Environ.* **142**–**143**, 487–493 (2013).
93. Su, Y., Straathof, N. J. W., Hessel, V. & Noël, T. Photochemical Transformations Accelerated in Continuous-Flow Reactors: Basic Concepts

and Applications. *Chem. - A Eur. J.* **20**, 10562–10589 (2014).
94. Chang, C.-C., Chen, L.-C. C. & Liu, S.-J. L. Investigation of electro-oxidation of methanol and benzyl alcohol at boron-doped diamond electrode: evidence for the mechanism for fouling film formation. *J. Phys. Chem. B* **110**, 19426–19432 (2006).
95. Serpone, N. & Emeline, A. V. Suggested terms and definitions in photocatalysis and radiocatalysis. *Int. J. Photoenergy* **4**, 91–131 (2007).
96. Kamat, P. V., Christians, J. A. & Radich, J. G. Quantum dot solar cells: hole transfer as a limiting factor in boosting the photoconversion efficiency. *Langmuir* **30**, 5716–5725 (2014).
97. DiMeglio, J. L. & Bartlett, B. M. Interplay of corrosion and photocatalysis during nonaqueous benzylamine oxidation on cadmium sulfide. *Chem. Mater.* **29**, 7579–7586 (2017).
98. Kisch, H. & Bahnemann, D. Best Practice in Photocatalysis: Comparing Rates or Apparent Quantum Yields? *J. Phys. Chem. Lett.* **6**, 1907–1910 (2015).
99. Gomollón-Bel, F. Ten Chemical Innovations That Will Change Our World. *Chem. Int.* **41**, 1–17 (2019).
100. Baker, C. O., Huang, X., Nelson, W. & Kaner, R. B. Polyaniline nanofibers: broadening applications for conducting polymers. *Chem. Soc. Rev.* **46**, 1510–1525 (2017).
101. Jäckle, S. *et al.* Potential of PEDOT:PSS as a hole selective front contact for silicon heterojunction solar cells. *Sci. Rep.* **7**, 2170–2177 (2017).
102. Chen, K., Deng, X., Dodekatos, G. & Tüysüz, H. Photocatalytic Polymerization of 3,4-Ethylenedioxythiophene over Cesium Lead Iodide Perovskite Quantum Dots. *J. Am. Chem. Soc.* (2017).
103. Kirkwood, N. *et al.* Finding and Fixing Traps in II–VI and III–V Colloidal Quantum Dots: The Importance of Z-Type Ligand Passivation. *J. Am. Chem. Soc.* **140**, 15712–15723 (2018).
104. Trent, J. S., Scheinbeim, J. I. & Couchman, P. R. Ruthenium tetraoxide staining of polymers for electron microscopy. *Macromolecules* **16**, 589–598 (1983).
105. Kirchmeyer, S. & Reuter, K. Scientific importance, properties and growing applications of poly(3,4-ethylenedioxythiophene). *J. Mater. Chem.* **15**, 2077–2088 (2005).
106. Kuehnel, M. F. & Reisner, E. Solar Hydrogen Generation from Lignocellulose. *Angew. Chemie Int. Ed.* **57**, 3290–3296 (2018).
107. Wakerley, D. W. *et al.* Solar-driven reforming of lignocellulose to H_2 with a CdS/CdOx photocatalyst. *Nat. Energy* **2**, 17021–17030 (2017).
108. Kasap, H., Achilleos, D. S., Huang, A. & Reisner, E. Photoreforming of lignocellulose into H_2 using nano-engineered carbon nitride under benign conditions. *J. Am. Chem. Soc.* 28 (2018).
109. Uekert, T., Kuehnel, M. F., Wakerley, D. W. & Reisner, E. Plastic waste as a feedstock for solar-driven H_2 generation. *Energy Environ. Sci.* **11**, 2853–2857 (2018).
110. Uekert, T., Kasap, H. & Reisner, E. Photoreforming of Nonrecyclable Plastic Waste over a Carbon Nitride/Nickel Phosphide Catalyst. *J. Am. Chem. Soc.* **141**, 15201−15210 (2019).

111. Simon, T. *et al.* Redox shuttle mechanism enhances photocatalytic H_2 generation on Ni-decorated CdS nanorods. *Nat. Mater.* **13**, 1013–1018 (2014).
112. Ishibashi, K., Fujishima, A., Watanabe, T. & Hashimoto, K. Detection of active oxidative species in TiO_2 photocatalysis using the fluorescence technique. *Electrochem. commun.* **2**, 207–210 (2000).
113. Han, X. *et al.* Structural insight into catalytic mechanism of PET hydrolase. *Nat. Commun.* **8**, 2106–2011 (2017).
114. Habisreutinger, S. N., Schmidt-Mende, L. & Stolarczyk, J. K. Photocatalytic Reduction of CO_2 on TiO_2 and Other Semiconductors. *Angew. Chemie Int. Ed.* **52**, 7372–7408 (2013).
115. Stolarczyk, J. K., Bhattacharyya, S., Polavarapu, L. & Feldmann, J. Challenges and Prospects in Solar Water Splitting and CO_2 Reduction with Inorganic and Hybrid Nanostructures. *ACS Catal.* (2018).
116. Tollefson, J. Can the World Slow Global Warming? *Nature* **572**, 325–326 (2019).
117. Manzi, A. *et al.* Light-Induced Cation Exchange for Copper Sulfide Based CO_2 Reduction. *J. Am. Chem. Soc.* **137**, 14007–14010 (2015).
118. Wang, D. *et al.* How and Why Nanoparticle's Curvature Regulates the Apparent pK_a of the Coating Ligands. *J. Am. Chem. Soc.* **133**, 2192–2197 (2011).
119. Woehrle, G. H., Brown, L. O. & Hutchison, J. E. Thiol-Functionalized, 1.5-nm Gold Nanoparticles through Ligand Exchange Reactions: Scope and Mechanism of Ligand Exchange. *J. Am. Chem. Soc.* **127**, 2172–2183 (2005).
120. Fogg, P. G. T. *Carbon Dioxide in Non-Aqueous Solvents at Pressure less than 200 kPa*. (1992).
121. Rosen, B. A. *et al.* Ionic Liquid-Mediated Selective Conversion of CO_2 to CO at Low Overpotentials. *Science.* **334**, 643–644 (2011).
122. Dong, C. *et al.* Size-dependent activity and selectivity of carbon dioxide photocatalytic reduction over platinum nanoparticles. *Nat. Commun.* **9**, 1252–1262 (2018).
123. Ran, J., Jaroniec, M. & Qiao, S.-Z. Cocatalysts in Semiconductor-based Photocatalytic CO_2 Reduction: Achievements, Challenges, and Opportunities. *Adv. Mater.* **30**, 1704649–1704679 (2018).
124. McQuillin, F. J. *Homogeneous Hydrogenation in Organic Chemistry*. (1976).
125. Prier, C. K., Rankic, D. A. & MacMillan, D. W. C. Visible Light Photoredox Catalysis with Transition Metal Complexes: Applications in Organic Synthesis. *Chem. Rev.* **113**, 5322–5363 (2013).
126. Romero, N. A. & Nicewicz, D. A. Organic Photoredox Catalysis. *Chem. Rev.* **116**, 10075–10166 (2016).
127. Balzani, V., Bergamini, G. & Ceroni, P. Photochemistry and photocatalysis. *Rend. Lincei* (2017).
128. Magagnano, G. *et al.* Photocatalytic ATRA reaction promoted by iodo-Bodipy and sodium ascorbate. *Chem. Commun.* **53**, 1591–1594 (2017).
129. Pal, A., Ghosh, I., Sapra, S. & König, B. Quantum Dots in Visible-Light Photoredox Catalysis: Reductive Dehalogenations and C−H Arylation

Reactions Using Aryl Bromides. *Chem. Mater.* **29**, 5225–5231 (2017).
130. Zhang, Z., Edme, K., Lian, S. & Weiss, E. A. Enhancing the Rate of Quantum-Dot-Photocatalyzed Carbon−Carbon Coupling by Tuning the Composition of the Dot's Ligand Shell. *J. Am. Chem. Soc.* **139**, 4246–4249 (2017).
131. Caputo, J. A. *et al.* General and Efficient C−C Bond Forming Photoredox Catalysis with Semiconductor Quantum Dots. *J. Am. Chem. Soc.* **139**, 4250–4253 (2017).
132. Nicewicz, D. A. & MacMillan, D. W. C. Merging photoredox catalysis with organocatalysis: the direct asymmetric alkylation of aldehydes. *Science.* **322**, 77–80 (2008).
133. Lewis, N. S. Developing a scalable artificial photosynthesis technology through nanomaterials by design. *Nat. Nanotechnol.* **11**, (2016).
134. Pinaud, B. A. *et al.* Technical and economic feasibility of centralized facilities for solar hydrogen production via photocatalysis and photoelectrochemistry. *Energy Environ. Sci.* 1983–2002 (2013). doi:10.1039/c3ee40831k
135. O'Regan, B. & Grätzel, M. A low-cost, high-efficiency solar cell based on dye-sensitized colloidal TiO_2 films. *Nature* **353**, 737–740 (1991).
136. Mazzaro, R. *et al.* Uniform Functionalization of High-Quality Graphene with Platinum Nanoparticles for Electrocatalytic Water Reduction. *ChemistryOpen* **4**, 268–273 (2015).
137. Grzelczak, M., Vermant, J., Furst, E. M. & Liz-Marzá, L. M. Directed Self-Assembly of Nanoparticles. *ACS Nano* **4**, 3591–3605 (2010).
138. Cambié, D. & Noël, T. Solar Photochemistry in Flow. *Top. Curr. Chem.* **376**, 45 (2018).
139. Pieber, B., Shalom, M., Antonietti, M., Seeberger, P. H. & Gilmore, K. Heterogeneous Photocatalysis in Serial Micro-Batch Reactors. *Angew. Chemie Int. Ed.* **57**, 9976–9979 (2018).
140. Italia, V. *et al.* Laser-Inscribed Glass Microfluidic Device for Non-Mixing Flow of Miscible Solvents. *Micromachines* **10**, 23–32 (2018).
141. Ashton, P. R. *et al.* A Three-Pole Supramolecular Switch. *J. Am. Chem. Soc.* **121**, 3951–3957 (1999).
142. Niu, W.-J. *et al.* Dumbbell-shaped carbon quantum dots/AuNCs nanohybrid as an efficient ratiometric fluorescent probe for sensing cadmium (II) ions and l-ascorbic acid. *Carbon N. Y.* **96**, 1034–1042 (2016).
143. Ju, E. *et al.* Heterogeneous Assembled Nanocomplexes for Ratiometric Detection of Highly Reactive Oxygen Species in Vitro and in Vivo. *ACS Nano* **6**, 6014–6023 (2019).
144. Kodaimati, M. S. *et al.* Viewpoint: Challenges in Colloidal Photocatalysis and Some Strategies for Addressing Them. *Inorg. Chem.* **57**, 3659–3670 (2018).
145. Carbone, L. *et al.* Synthesis and Micrometer-Scale Assembly of Colloidal CdSe/CdS Nanorods Prepared by a Seeded Growth Approach. *Nano Lett.* **7**, 2942–2950 (2007).